

FEDERAL UNIVERSITY OF PARAÍBA
RENEWABLE AND ALTERNATIVE ENERGIES CENTER
ELECTRICAL ENGINEERING GRADUATE PROGRAM

ANTI-WINDUP AND LOAD SHEDDING FOR
SMOOTH TRANSITIONS IN MULTI-LOOP
POWER MANAGEMENT OF ISLANDED
SINGLE-UNIT-SOURCED MICROGRIDS

Pedro Aquino de Alcântara

João Pessoa
June - 2023

PEDRO AQUINO DE ALCÂNTARA

**ANTI-WINDUP AND LOAD SHEDDING FOR SMOOTH
TRANSITIONS IN MULTI-LOOP POWER
MANAGEMENT OF ISLANDED SINGLE
UNIT-SOURCED MICROGRIDS**

Final dissertation presented to Electrical Engineering
Graduate Program of Federal University of Paraíba -
UFPB, as a requirement to obtain Master degree in
Electrical Engineering.

Advisor: Prof. Dra. Camila Mara Vital Barros
Co-advisor: Prof. Dr. Luciano Sales Barros

João Pessoa - PB

2023

Catálogo na publicação
Seção de Catalogação e Classificação

A347a Alcântara, Pedro Aquino de.

Anti-windup and load shedding for smooth transitions
in multi-loop power management of islanded single
unit-sourced microgrids / Pedro Aquino de Alcântara. -
João Pessoa, 2023.

91 f. : il.

Orientação: Camila Mara Vital Barros.

Coorientação: Luciano Sales Barros.

Dissertação (Mestrado) - UFPB/CEAR.

1. Engenharia elétrica. 2. Microrrede ilhada. 3.
Unidade fotovoltaica com baterias. 4. Gerenciamento de
potência multi-loop. 5. Corte de carga. I. Barros,
Camila Mara Vital. II. Barros, Luciano Sales. III.
Título.

UFPB/BC

CDU 621.3(043)

FEDERAL UNIVERSITY OF PARAÍBA - UFPB
RENEWABLE AND ALTERNATIVES ENERGIES CENTER - CEAR
ELECTRICAL ENGINEERING GRADUATE PROGRAM - PPGEE

Thesis Defense Committee, as signed below, approves the Final Examination

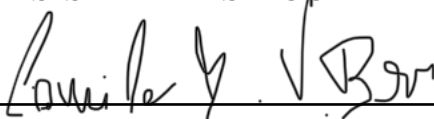
**ANTI-WINDUP AND LOAD SHEDDING FOR SMOOTH
TRANSITIONS IN MULTI-LOOP POWER
MANAGEMENT OF ISLANDED SINGLE
UNIT-SOURCED MICROGRIDS**

Made by

PEDRO AQUINO DE ALCÂNTARA

as a requirement to obtain the title of
Master in Electrical Engineering.

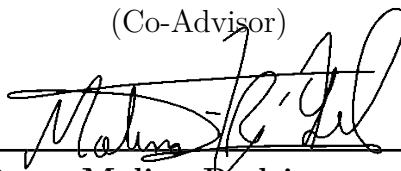
THESIS DEFENSE COMMITTEE



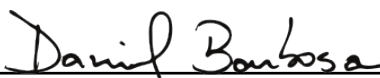
Prof. Dra. Camila Mara Vital Barros - UFPB/PPGEE
(Advisor - Committee President)



Prof. Dr. Luciano Sales Barros - UFPB/CI
(Co-Advisor)



Prof. Dr. Yuri Percy Molina Rodriguez - UFPB/PPGEE
(Internal Member)



Prof. Dr. Daniel Barbosa - UFBA
(External Member)

João Pessoa - PB, June 29, 2023

Dedication

This work is dedicated to my mother Isabel Rubenia who has made everything possible.

Acknowledgements

First, I thank God and the good spirits for never leaving me alone and always giving me the strength to keep going.

I thank my mother, my life's queen, for always standing by my side in all moments and making everything possible. Everything I am today I owe to her.

I thank my advisors Camila Mara and Luciano Sales for never giving up on helping me and always believing I could do it. In addition, I thank all Electrical Engineering Graduate Program faculty and staff for their support.

I thank my research mates for being there all the time believing in our potential and making all efforts worth.

I thank the Higher Education Personnel Improvement Coordination (CAPES, in Portuguese) for the financial support to make this work possible.

Finally, I thank my relatives and friends for always sending me good vibes.

"One moment of pain is worth a lifetime of glory". (Louis Zamperini)

Abstract

The huge development of distributed generation (DG) systems and their insertion in the main grid has made the concept of microgrids the target of much research. Renewable energy sources (RES) like photovoltaic (PV) and wind systems represent a vast part of DG units once they have been developed to replace non-clean energy sources. Still, it has been a challenge to make possible RES operations in islanded microgrid environments, especially those formed by PV systems. The intermittent behavior of RES and their lack of power reserve have provoked many problems like voltage and frequency deviations. For this reason, energy storage devices such as battery energy storage systems (BESS) represent an important solution for power support in islanded systems due to their fast response to outages. Several strategies have been studied to provide standalone microgrid environments with power management for maintaining the balance between generation power and load demand. However, critical situations where the microgrid is composed of only one generation system have been little addressed. In these cases, the physical limitation of BESS instigates crucial decisions for keeping the grid balance such as generation power curtailment, when BESS charging limits are reached, and load-shedding, when it reaches discharging limits. This work studies a multi-loop power management strategy for a three-phase islanded microgrid formed by one PV/BESS-based generation unit with grid-forming droop control for the Voltage Source Inverter (VSI), including a secondary frequency/voltage regulation and Proportional-Resonant control loops. To better understand the unit behavior, the operation is divided into states. The transition among the states is performed by the multi-loop strategy whenever the BESS has reached any limit. However, it is extremely necessary to ensure smooth state transitions in order to avoid harmful current and voltage variations. As the strategy is based on Proportional-Integral controllers, the physical limitation of the BESS may cause constant steady-state errors and consequently integration windup. This problem is extremely undesirable, because it may cause decision delays and/or undesired transients during the transition among operation states. This work proposes the use of integration anti-windup techniques in important PI controllers for improving state transitions. Two well-known anti-windup techniques are compared in order to assess smoother behavior. In addition, this work provides an improved load-shedding strategy based on the unit DC-link voltage to keep the power balance in cases of low generation power availability. The results showed that anti-windup methods are essential to avoid undesired transients, decision delays, and current/voltage harmful oscillations during operation state transitions. Two anti-windup methods were tested: clamping and back-calculation. Both showed satisfactory performances. However, the back-calculation technique showed a better performance in a situation when the BESS state-of-charge (SoC) has to be regulated. This technique presented a better response by

avoiding under and overshoots during the transitions. Finally, the work was developed through Matlab/Simulink simulations.

Keywords: Islanded Microgrid. Photovoltaic-Battery unit. Multi-loop Power Management. Grid-Forming Droop Control. Anti-windup. Load Shedding.

Resumo

O grande desenvolvimento dos sistemas de geração distribuída (GD) e sua inserção na rede principal tornou o conceito de microrredes alvo de muitas pesquisas. Fontes de energia renovável (FER) como sistemas fotovoltaicos (PV) e eólicos representam uma grande parte das unidades de GD uma vez que foram desenvolvidas para substituir fontes de energia não limpas. Ainda assim, tem sido um desafio viabilizar operações de FER em ambientes insulares de MG, principalmente naqueles formados por sistemas fotovoltaicos. O comportamento intermitente dos RES e sua falta de reserva de energia provocaram muitos problemas como desvios de tensão e frequência. Por esta razão, os dispositivos de armazenamento de energia, como os sistemas de armazenamento de energia por bateria (BESS), representam uma importante solução para suporte de energia em sistemas ilhados devido à sua rápida resposta a interrupções. Várias estratégias foram estudadas para fornecer ambientes de microrredes autônomos com gerenciamento de energia para manter o equilíbrio entre geração de energia e demanda de carga. No entanto, situações críticas em que a microrrede é composta por apenas um sistema de geração têm sido pouco abordadas. Nesses casos, a limitação física do BESS instiga decisões cruciais para manter o equilíbrio da rede, como o corte de potência de geração, quando os limites de carregamento do BESS são atingidos, e o corte de carga, quando BESS atinge os limites de descarga. Este trabalho estuda uma estratégia de gerenciamento de energia multi-loop para uma microrrede trifásica, ilhada e formada por uma unidade de geração fotovoltaica com BESS, incluindo controle formador de rede baseado em controle droop para o inversor fonte de tensão (VSI), incluindo uma regulação de frequência/tensão secundária, e malhas de controle Proporcional-Ressonante. Para entender melhor o comportamento da unidade, a operação é dividida em estados. A transição entre os estados é realizada pela estratégia multi-loop sempre que o BESS atingir algum limite. No entanto, é extremamente necessário garantir transições de estado suaves para evitar variações prejudiciais de corrente e tensão. Como a estratégia é baseada em controladores Proporcionais-Integrais, a limitação física do BESS pode ocasionar erros constantes de regime permanente e conseqüentemente windup da integração. Este problema é extremamente indesejável, pois pode causar atrasos de decisão e/ou transientes indesejados durante a transição de estados. Este trabalho propõe o uso de técnicas anti-windup de integração em controladores PI para melhorar as transições de estado. Duas técnicas anti-windup bem conhecidas são comparadas a fim de avaliar um comportamento mais suave. Além disso, este trabalho fornece uma estratégia aprimorada de corte de carga com base na tensão do barramento CC da unidade para manter o equilíbrio de potência em casos de baixa disponibilidade de geração. Os resultados mostraram que métodos anti-windup são essenciais para evitar transientes indesejados, atrasos de decisão e oscilações prejudiciais de corrente/tensão durante as transições de estado de operação. Dois métodos anti-windup foram testados: clamping e back-calculation.

Ambos apresentaram desempenhos satisfatórios. No entanto, a técnica back-calculation mostrou um melhor desempenho em situações em que o estado de carga (SoC) do BESS precisa ser regulado. Essa técnica apresentou uma melhor resposta evitando under e overshoots dos controladores durante as transições. Por fim, o trabalho foi desenvolvido por meio de simulações no Matlab/Simulink.

Palavras-chave: Microrrede Ilhada. Unidade Fotovoltaica com Baterias. Gerenciamento de Potência Multi-loop. Controle Formador de Rede baseado em Controle Droop. Anti-windup. Corte de Carga.

Figure List

Figure 1 – Brazilian DG cumulative installed power capacity until the middle of May 2023.	16
Figure 2 – Structure of the microgrid unit studied in this work.	29
Figure 3 – Equivalent circuit of single-diode PV cell model.	30
Figure 4 – PV module characteristic $I-V$ curve.	31
Figure 5 – $I-V$ curve remarkable points.	32
Figure 6 – Modified equivalent circuit for $N_{pp} \times N_{ss}$ modules PV array.	32
Figure 7 – Complete model of $LiFePO_4$ BESS.	34
Figure 8 – DC-DC boost converter characteristic circuit.	35
Figure 9 – Boost current and voltage waveforms for CCM.	36
Figure 10 – DC-DC bidirectional buck-boost converter characteristic circuit.	38
Figure 11 – Buck mode circuit detailed.	38
Figure 12 – Buck mode current and voltage waveforms for CCM.	39
Figure 13 – VSI configuration.	41
Figure 14 – SPWM waveforms.	42
Figure 15 – LCL filter topology.	43
Figure 16 – DC-DC Converters control.	45
Figure 17 – Microgrid control flowchart.	50
Figure 18 – States transitions criteria.	51
Figure 19 – PI controller with CAW scheme.	53
Figure 20 – PI controller with BCAW scheme.	54
Figure 21 – Proposed load shedding strategy flowchart.	56
Figure 22 – P&O algorithm flowchart.	59
Figure 23 – Boost converter control.	59
Figure 24 – BESS bidirectional converter control strategy.	61
Figure 25 – VSI Grid-forming control diagram.	63
Figure 26 – Droop control characteristic curves.	64
Figure 27 – Droop control diagram.	65
Figure 28 – PR control loops strategy blocks.	66
Figure 29 – PLL strategy block diagram.	67
Figure 30 – Scenario 1 results without AWD in PI_1	70
Figure 31 – Scenario 1 results with CAW in PI_1	71
Figure 32 – Comparison between AWD strategies in PV power, BESS power, SoC, and PI_1	72
Figure 33 – Scenario 2 results without AWD in PI_2	73
Figure 34 – Scenario 2 results with CAW in PI_2	74

Figure 35 – Comparison between AWD strategies in PI_2	75
Figure 36 – Scenario 3 results without AWD in PI_{B1} , and with CAW in PI_1	76
Figure 37 – Scenario 3 results with CAW in PI_{B1} and PI_1	77
Figure 38 – Comparison between AWD strategies in PV power, BESS power, SoC, and PI_{B1}	77
Figure 39 – Scenario 4 results with $UV_{dc}LS$ and secondary frequency droop turned on.	79
Figure 40 – Comparison between $UFLS$ and $UV_{dc}LS$ with frequency secondary control turned off.	80
Figure 41 – Scenario 5 results without AWD in PI_{B3}	81
Figure 42 – Scenario 5 results with CAW in PI_{B3}	82
Figure 43 – Comparison between AWD strategies in PV power, BESS power, SoC, and PI_{B3}	83

Table List

Table 1 – Characteristics of main references studied to motivate the present work.	23
Table 2 – Setup parameters.	44
Table 3 – Control Parameters.	67

Contents

1	INTRODUCTION	15
1.1	CONTEXTUALIZATION	15
1.2	OBJECTIVE	19
1.2.1	Specific Objectives	20
1.3	CONTRIBUTIONS	20
1.4	METHODOLOGY	20
1.5	DOCUMENT ORGANIZATION	22
2	BIBLIOGRAPHIC REVIEW	23
3	MICROGRID MODELING	29
3.1	PV ARRAY AND BESS MODELING	29
3.1.1	PV array	30
3.1.2	BESS	33
3.2	DC-DC CONVERTERS	34
3.2.1	Boost Converter	34
3.2.2	Bidirectional Buck-Boost Converter	37
3.3	VSI	41
3.3.1	Sinusoidal Pulse Width Modulation (SPWM)	41
3.4	LCL FILTER	43
3.5	LOAD MODEL	43
4	POWER MANAGEMENT STRATEGY	45
4.1	OPERATION STATES	47
4.1.1	State 1 - Normal Operation	47
4.1.2	State 2 - BESS Charging Limit	47
4.1.3	State 3 - BESS Maximum SoC	48
4.1.4	State 4 - BESS Discharging Limit	49
4.1.5	State 5 - BESS Minimum SoC	49
4.2	PROPOSED IMPROVEMENTS	51
4.2.1	Anti-Windup Strategies	53
4.2.1.1	Clamping Anti-Windup	53
4.2.1.2	Back-Calculation Anti-Windup	54
4.2.2	Proposed Load-Shedding Scheme	54
5	CONTROL SYSTEMS	58

5.1	PV BOOST CONTROL	58
5.1.1	Perturb and Observe MPPT	58
5.1.2	Control Design	59
5.2	BESS BIDIRECTIONAL BUCK-BOOST CONTROL	61
5.2.1	Control Design	62
5.3	VSI GRID-FORMING DROOP CONTROL	62
5.3.1	Power Calculation Theory	63
5.3.2	Droop Control	64
5.3.3	Secondary Droop Control	64
5.3.4	PR Control	65
5.3.5	Frequency Estimation: Phase Locked Loop	66
6	SIMULATION RESULTS	69
6.1	Simulation Results	69
6.1.1	Scenario 1: Transition from State 1 to State 3	69
6.1.2	Scenario 2: Transition from State 1 to State 2	73
6.1.3	Scenario 3: Transition from State 2 to State 3	75
6.1.4	Scenario 4: Transition from State 1 to State 4	78
6.1.4.1	$UV_{dc}LS \times UFLS$ Comparison	79
6.1.5	Scenario 5: Transition from State 1 to State 5	82
7	CONCLUSION	85
	BIBLIOGRAPHY	87

1 Introduction

1.1 CONTEXTUALIZATION

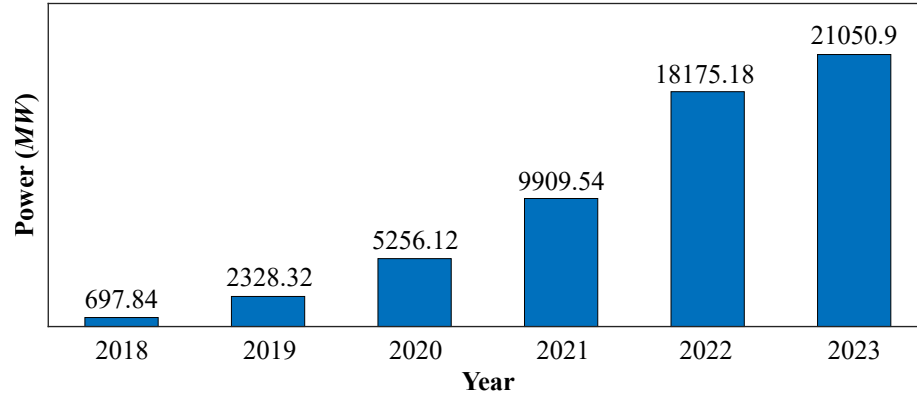
Technological advancements have been crucial for human life development over the years. However, the increase of technological devices and machines attached to energy misuse demand robust electrical energy generation systems. Unclean generation sources have been extensively used to meet this need. According to United Nations (UN), energy supply is the dominant contributor to climate change, accounting for around 60% of greenhouse gas emissions (NATIONS, 2022). Therefore, the seeking for clean and renewable energy is one of the UN's Sustainable Development Goals (SDGs), once SDG 7 looks to "ensure access to affordable, reliable, sustainable and modern energy for all" (LIAO *et al.*, 2021).

Clean and renewable energy sources (RES) have been widely discussed in recent years as one of the main alternatives to combat greenhouse gas emissions and climate change. Non-conventional renewable sources like solar, wind, and biofuel, have become the target of many studies and discussions. These kinds of generations have been increasingly connected to the main grid due to their increasing reliability and decreasing cost.

Therefore, these systems may be connected near load centers as distributed generation (DG) systems. The improvement of its reliability attached to easy installation has provided the creation of law regulations to allow penetration of DG units to the main grid. In Brazil, Electrical Energy National Agency (ANEEL), through its resolution number 482/2012, allows customers to produce energy using RES as DG units. It means the surplus/missing power is absorbed/provided by the main grid, respectively (MAESTRI; ANDRADE, 2022). Because of this, according to the Brazilian Association of Distributed Generation (ABGD) and ANEEL, by April 2023 DG units reached 19 GW of installed power, where 98.6% of these units are represented by solar photovoltaic (PV) generation systems (ABGD, 2023). This number surpasses 20 GW by the middle of May 2023, as depicted in Figure 1, where the evolution of Brazilian DG cumulative power capacity over the years until the middle of May 2023, according to ANEEL Brazilian DG Dashboard, is presented.

As aforementioned, the wide penetration of DG units to the main grid around the world counts for a huge amount of solar PV systems thanks to its predictability, silence, easy maintenance, and easy installation (GARG *et al.*, 2020). They have also become popular as DG due to their immediate and efficient utilization (WANG; ZHANG, 2009). For these reasons, the concept of microgrids has been the target of much research.

Figure 1 – Brazilian DG cumulative installed power capacity until the middle of May 2023.



Source: ANEEL.

Microgrids may be defined as local grids formed by primary generation (especially PV systems) represented by DG units, energy storage systems, and local loads (KARIMI; ORAEE; GUERRERO, 2017). In other words, it is a set of distributed energy resources and interconnected load (MENG *et al.*, 2015). However, once DG units composed of RES rely on natural resources, microgrids' proper operation has been a challenge.

Much research has been developed to offer many benefits to customers and power utilities, ranging from high power quality and reliability to diversified energy options (SUN *et al.*, 2015). Microgrids may be structured in many configurations, depending on load and generation requirements. It may be presented in DC or AC structures, where AC configuration may be composed of single-phase or three-phase units (KARIMI; ORAEE; GUERRERO, 2017). DC microgrids have received special attention in recent years because of PV systems' success, battery storage systems proliferation, and DC loads growth (like LED lighting and data centers). However, since most loads are represented by AC equipment and devices, and due to the possibility to work in cooperation with the main grid, AC microgrids hold the biggest amount of studies (CHE *et al.*, 2015).

Hence, AC microgrids have been addressed by many works in two main operation modes: grid-connected and islanded modes. At first, the microgrid work in cooperation with the main grid, exchanging power and alternating with each other to improve the reliability of the power supply (ZHENG; CHANG; WANG, 2013). Once some disturbance occurs, the microgrid is disconnected from the main grid and starts to operate standalone in islanded mode (KARIMI *et al.*, 2017). Therefore, both modes have instigated the development of control strategies to provide microgrids' with proper operation.

Due to the intermittency of RES and their lack of power reserve, ensuring microgrids' security, reliability, and power quality has been a challenge, especially in islanded environments composed of PV units. For this reason, integrating Battery Energy Storage Systems (BESS) into islanded systems has been the main alternative for providing frequency and voltage support (SHATAKSHI; SINGH; MISHRA, 2018)(KARIMI *et al.*,

2017). The BESS' fast power response makes it the ideal solution for PV generation fluctuations. Power management control strategies attached to BESS provide many solutions to frequency control issues (SERBAN; MARINESCU, 2014) in microgrid environments. Thus, PV/BESS-based architectures call for efficient control techniques to make its operation smooth in different operation states (SHATAKSHI; SINGH; MISHRA, 2018).

Several works have been developed for the power management of islanded microgrids with PV generation and BESS. The researchers address these kinds of microgrids under different situations, with different architectures. Islanded environments with multiple DG units instigate the evolution of many strategies for frequency control and load sharing. Mostly, they regard hierarchical techniques to respect the units' power capacity and battery limits. However, it is important to consider extreme situations where load-sharing and hierarchical systems may not be employed. Microgrids composed of a single DG unit are little addressed in the literature. These kinds of systems require extreme decisions to keep the power balance. Extremely low-load situations demand generation curtailment to match the load, considering that the storage systems' limitations make the surplus power absorption unfeasible. On the other hand, a very high load or low generation availability would require the system to shed load as the last resource to keep the power balance. From this viewpoint, the contributions of this work rely on ensuring smooth transitions of single-sourced PV/BESS-based microgrids during generation power adjustment and load-shedding situations. The next paragraphs discuss how the contributions take place.

During critical conditions of low voltage and frequency, load-shedding has been one of the most efficient methods to maintain the system stability (SHEIKHZADEHBABOLI *et al.*, 2022). The traditional methods are the most used due to their easy implementation, and the use of simple relays (BAKAR *et al.*, 2017). When the frequency or voltage drops below a specific threshold, the algorithm sheds a specific amount of load. The main disadvantage of traditional schemes is the susceptibility to under/over-shedding problems since they are unable to measure the power imbalance. Further, these methods generally rely on frequency estimation to make a shedding decision. It may be a problem considering it needs to wait until low-frequency limits are reached to act. Long delays may expose important devices to harmful voltage and current oscillations. Furthermore, semi-adaptive and adaptive techniques have been developed to improve selectivity and accuracy in determining the amount of load to be shed. Semi-adaptive techniques are based on the rate of change of frequency or voltage to improve the selectivity when compared to the traditional method. Adaptive techniques improve the traditional method by enhancing the accurate amount of load to be shed through the frequency derivative, depending on the system frequency response (BAKAR *et al.*, 2017). However, semi-adaptive schemes do not provide any improvement during high faults, while adaptive methods do not perform well during frequency behavior oscillation. On top of that, traditional load-shedding schemes are still the best and easier options, but the previously mentioned drawbacks of these

methods may be taken into account. Therefore, one of the aims of the present work is to propose an improvement of a load-shedding technique for single-sourced microgrids in which the DC-link voltage is used as a trigger to shed loads.

Furthermore, in those critical situations where the single-sourced microgrid control system is required to cut power or shed load to keep the grid stable, a reliable power management strategy is necessary. Most microgrid control strategies rely on PID controllers due to their well-established implementation and tuning. These controllers have been widely employed as one of the most common solutions for many practical problems (ÅSTRÖM; HÄGGLUND, 2006). However, it is crucial to consider their limitations and drawbacks in order to avoid undesired behaviors. Devices such as batteries and PV units have natural limitations which may provoke non-linear performance in PID controllers. In several practical processes, this limitation may cause the output signal of the controller to be different from the real signal applied to the process (HANUS, 1980a). For example, when a battery reaches its maximum operating current, the controller input error will not be null. The action of the integrator attempts to mitigate the steady-state error by increasing or decreasing the controller output signal, but the saturated battery can deliver no larger current. The integration of the non-null error pushes the controller output away from the desired operation region. This effect is popularly called integration "windup" (ÅSTRÖM; HÄGGLUND, 2006). As expected, this effect is very undesired when it takes to the power management of single-sourced islanded microgrids, especially when it relies on multi-PID loops. For this reason, the employment of anti-windup techniques is crucial for ensuring smooth transitions among operation states when power curtailment or load shedding is needed.

Hence, this work studies a multi-loop power management control of a single-sourced PV/BESS-based islanded microgrid with grid-forming droop control. The PV unit and the BESS share the same capacitive DC-link through DC-DC converters: a boost converter and a bidirectional buck-boost converter, respectively. First, the use of a bidirectional converter allows the BESS to controllably charge or discharge depending on the grid's need, does not limit the DC-link voltage to the BESS nominal voltage, and protects the BESS from harmful voltage and current oscillations (MAHMOOD; MICHAELSON; JIANG, 2012). Secondly, the multi-loop strategy changes the PV unit power operation point through the boost controller to adjust the PV power according to the load conditions. Finally, grid-forming droop control is used for a Voltage Source Inverter (VSI). Droop control has been extensively used as a method to support islanded PV/BESS-based microgrids power supply. The absence of synchronous generators in the power system makes those architectures lose frequency and voltage references. Thus, droop control acts by imitating the behavior of synchronous generation machines, increasing or decreasing frequency and voltage magnitude according to grid active and reactive power variation, respectively (LI *et al.*, 2021). However, it is necessary to consider droop control drawbacks. Small load

oscillations may cause considerable voltage and frequency variations out of safe range (NUTKANI *et al.*, 2015). Therefore, a secondary droop control was implemented to regulate frequency and voltage. Attached to the droop control strategy, a Proportional-Resonant (PR) closed-loop strategy is implemented to track droop reference voltage waveform (VASQUEZ *et al.*, 2013)(KARIMI; ORAEE; GUERRERO, 2017).

Through the aforementioned set of control systems, the microgrid unit operates according to five operation states. The first one is considered the normal operation state where the BESS absorbs or injects power to keep the power balance. The second one regards a situation where the BESS reaches the maximum charging power due to a low load or large PV power availability, so the PV unit must reduce the injecting power. In the third one, the BESS has reached the maximum state-of-charge (SoC) level, so its power leads to zero for protection. Then the PV unit must again perform power curtailment. Similarly, the fourth operating state is when the BESS has reached the discharging power limit but the load demand is higher than the PV unit plus the BESS power. In these cases, there is no other option for the system but to shed load to keep the stability. Finally, when the BESS reaches the minimum SoC limit, the power leads to zero, and the microgrid must again perform load shedding to maintain the balance.

On top of that, the present work aims to present an improvement in the power management strategy to ensure a smooth transition among the operation states. Depending on the state the microgrid operates, the input reference error of the PI controllers may change, especially when the BESS reaches the limits. Then, during state transitions, integration windup causes undesired transients, exposing the microgrid devices to large voltage and current variations. This work proposes the use of anti-windup techniques in important PI controllers to avoid these harmful behaviors. Two well-known anti-windup methods are tested to attest to the best solution. Additionally, an improvement for a load-shedding strategy in which the DC-link voltage level triggers the shedding decision is proposed. This strategy attached to a robust frequency control shows to be easier to implement once it does not rely on frequency estimation, but only on voltage measurement, ensuring grid frequency and voltage regulation.

1.2 OBJECTIVE

Model and simulate multi-loop power management for a single-sourced PV/BESS-based islanded microgrid architecture with grid-forming droop control, propose the use of anti-windup methods for ensuring smooth transitions among operation states, and propose an improvement for a load-shedding strategy used in these microgrid architectures.

1.2.1 Specific Objectives

The specific objectives of this work are:

- Modeling of the microgrid unit elements (PV unit, BESS, and converters);
- Implement the multi-loop power management strategy through the DC-DC converters control systems;
- Implement a grid-forming control based on droop control for islanded operation with secondary frequency and voltage regulation;
- Analyse the performance of two well-known anti-windup techniques in the power management strategy;
- Test an improvement for a load-shedding strategy based on the DC-link voltage level.

1.3 CONTRIBUTIONS

This work's main contribution consists of promoting smooth transitions in the power management of a single-sourced PV/BESS-based islanded microgrid through the use of anti-windup techniques in the PI controllers and proposing improvements for load shedding strategies. The proposed improvements look for providing the following features:

- Maintain the grid voltage and frequency levels for any load demand and/or generation availability;
- Avoid undesired transients during state transitions to prevent harmful voltage and current oscillations;
- Improve a load-shedding method based on the DC-link voltage to promote better decisions by preventing over-shedding;
- Keep the BESS operation at safe power and SoC values.

1.4 METHODOLOGY

First, literature was consulted to understand islanded microgrids' issues. The power management of islanded microgrids has been widely addressed in the literature, but single-sourced PV/BESS-based environments have been little studied regarding all power management possibilities. Thus, this analysis fomented the idea of modeling an islanded microgrid unit and implementing the control strategies in each converter. Two

main works were used as the main references for the studied microgrid structure and power management control.

The first step was modeling microgrid elements using Matlab/Simulink. The PV modules were modeled according to the methodology presented by (VILLALVA; GAZOLI; FILHO, 2009). The BESS used the equivalent circuit presented by (JUNIOR; BARROS; BARROS, 2021) and the ion-Lithium battery experimental data from (BARONTI *et al.*, 2013; BARONTI *et al.*, 2014a; BARONTI *et al.*, 2014b). After modeling the power elements, the DC-DC converters were projected and implemented: the boost converter for the PV unit and the bidirectional buck-boost converter for the BESS unit. Finally, the VSI and an LCL filter were modeled. Each element was modeled separately to be put together later.

The next step was designing the controllers. First was implemented the maximum power point tracking (MPPT) strategy for the PV unit followed by a closed loop strategy to track the MPPT voltage reference through the boost converter. Then, the bidirectional converter control system was designed to control the DC-link voltage by charging or discharging the BESS. Finally, the VSI control strategy was implemented. However, the integration of all converters was made step by step. First, the microgrid was modeled grid-connected through a grid-following strategy presented by (BARROS; BARROS, 2017). Note that this step was necessary only for the initialization of the simulation, but the focus of the work is the islanded operation. In this first step, the BESS system is disconnected from the system, the PV unit is represented by a constant power source. After that, the PV unit system with the boost converter and the closed-loop MPPT control was integrated into the system. The next step was to disconnect the system from the main grid and implement the grid-forming droop control in the VSI for islanded operation. Once it works properly, the BESS system including converters was connected. After some adjustments in the controllers, the unit works properly considering BESS limits within a safe range, so the operation state 1 is finished

After normal islanded operation worked as expected, the next step was to work on the BESS limits by implementing states 2 and 3. These are states that regard PV power curtailment when the BESS reaches charging limits. The chosen strategy for these situations was proposed by (MAHMOOD; MICHAELSON; JIANG, 2012). This strategy comprehends a multi-loop control to adjust PV power in order to regulate the BESS SoC and power.

Further, those states in which the discharging BESS limits were implemented (states 4 and 5). In these critical states, load-shedding is necessary to keep the power balance once the BESS discharging limits were reached. Then, a load-shedding strategy based on the DC-link voltage was developed and implemented by the research team, and presented by (SOARES, 2022). Additionally, a new control loop was proposed by the team

to regulate the SoC at the minimum level in order to circumvent deep discharge. However, some adjustments were necessary to avoid over-shedding and avoid undesired transients during SoC regulation. These improvements are presented in the present work.

In spite of all the operation states being implemented, large undesired transients were noticed during operation state transitions. When the microgrid was required to transit mainly from state 1 to states 2, 3, and 5, large voltage and current oscillations were noticed. Further, the reason for those undesired behaviors was found to be integration windup in important PI controllers. Then, the last step was to implement anti-windup techniques to avoid them. Two well-known anti-windup schemes were implemented to analyze and compare their performance.

1.5 DOCUMENT ORGANIZATION

This introductory chapter is followed by Chapter 2 where is presented all bibliographic reviews previously studied to make this work possible. This chapter lists the most relevant works in literature, addressing different microgrid architectures and control systems.

Chapter 3 describes the studied microgrid and the modeling of all elements. It presents all theoretical and mathematical basis used to model each element. These elements are PV units, BESS, DC-DC converters, VSI, LCL filter, and load model.

Chapter 4 details multi-loop power management. It includes the microgrid unit behavior in all operating states.

Chapter 5 addresses the theoretical basis for the implementation of control systems in all operating states. It details the power management method and the control systems designs.

Chapter 6 presents this work simulation results, and gives the microgrid setup parameters and the gains of the controllers.

Finally, Chapter 7 concludes the work.

2 Bibliographic Review

This chapter discusses the literature review that supports the present work. Several works about microgrids were consulted during the references' research tenure. It was observed the quantity of DG units in each studied architecture, their structure, and control systems. First, it was important to highlight whether the studied microgrid comprises a single-generation unit or multiple units. Also, noting the microgrid operation mode (islanded or grid-connected) to understand the control systems the study was carried out was necessary. Further, depending on the operation mode and on the control systems that each work employs to provide the microgrid with power management, it was observed whether the control systems employ any kind of anti-windup technique for those controllers that rely on integration activity to avoid harmful behaviors. Finally, it was observed if the adopted power management strategies include any kind of load-shedding method as a resource for maintaining the microgrid balance. The aforementioned features of each reference are condensed in Table 1. The following paragraphs detail each reference and the conclusions obtained from them.

Reference	Units	Mode	Anti-Windup	Load-Shedding
Mahmood, Michaelson and Jiang (2012)	Single	Islanded	Yes	No
Karimi, Oraee and Guerrero (2017)	Multiple	Islanded	-	No
Mahmood, Michaelson and Jiang (2015)	Multiple	Islanded	No	No
Chtita <i>et al.</i> (2021)	Single	Islanded	Yes	Yes
Rezkallah <i>et al.</i> (2019)	Multiple	Islanded	Yes	No
Mahmood and Blaabjerg (2022)	Multiple	Islanded	Yes	No
Behera and Saikia (2022)	Single	Grid-Connected	Yes	No
Mahmood and Jiang (2019)	Multiple	Islanded	No	No
Michaelson, Mahmood and Jiang (2017)	Multiple	Islanded	-	Yes
Sadoudi, Boudour and Kouba (2021)	Multiple	Islanded	-	Yes

Table 1 – Characteristics of main references studied to motivate the present work.

The first and main reference is found in the work of Mahmood, Michaelson and

Jiang (2012). The authors propose a power management control for an islanded unit composed of a PV unit and a battery sharing the same capacitive DC-link through DC-DC converters: boost for the PV unit, and bidirectional buck-boost for the battery. The power management control allows the unit to autonomously adapt the PV unit power in order to regulate the DC-link voltage and the battery SoC in situations where the PV power is larger than the load demand, and the battery has reached the charging limits (MAHMOOD; MICHAELSON; JIANG, 2012). To achieve this, the authors propose a multi-loop method formed by several PI controllers to push the reference voltage of the boost controller away from the maximum power point. Consequently, the PV unit reduces the power until the balance between generation and load is established. This strategy is the base for 3 operation states of the microgrid system studied in the present work, even though the authors do not divide the autonomous operation this way. The idea of state division is based on the reference presented in the next paragraph. However, some drawbacks were found during the states' transition. The reference input errors of some PI controllers are rarely null since they only act in extreme situations when the PV is required to cut power. Therefore, integration windup might easily affect the system behavior. The authors cite the use of a clamped anti-windup technique in one PI controller used to regulate the battery SoC in the maximum value. But, it was noticed that two important PI controllers also suffer from this problem bringing undesired transients for the operation. Furthermore, the authors do not address situations in which the load power is larger than the PV unit, and the BESS reaches the discharging limits. It is fundamental to address these situations in order to keep the power balance. The employment of load-shedding strategies is an excellent solution to meet this problem. Additionally, a control loop is important to protect the battery from deep discharge.

The second main important reference is the work of Karimi, Oraee and Guerrero (2017). It brings a hybrid microgrid architecture formed by two single-phase (SPU) and one three-phase (TPU) unit. Each SPU is formed by a PV unit and a BESS sharing the same DC-link, while TPU is only formed by a PV unit. The work proposes a decentralized method for load sharing among phases in islanded mode, taking into account PV power availability and BESS conditions. The frequency level is used to switch the units into five (SPU) or seven (TPU) operation states, according to a modified active-power/frequency droop control strategy experimentally validated (KARIMI; ORAEE; GUERRERO, 2017). The units' operation states inspired the states' division of the single-sourced microgrid studied here. It also inspired the employment of grid-forming droop control with a PR closed-loop strategy. Still, the microgrid structure studied in that work allows the system to share the load among the generation units to keep the balance. Therefore, extreme cases where load-shedding may be necessary are not addressed. Also, the authors do not detail the DC-DC controllers, so it is not possible to conclude that any anti-windup method was employed.

In Mahmood, Michaelson and Jiang (2015), the authors present power management for integrating a droop-controlled microgrid formed by one PV/battery-based hybrid unit with "n" droop-controlled units. The strategy provides the hybrid unit decentralized power management based on a multi-segment adaptive power/frequency characteristic curve. It makes the islanded microgrid autonomously match the load and keep power balance, considering hybrid unit BESS SoC limits and providing PV unit MPPT (MAHMOOD; MICHAELSON; JIANG, 2015). It is important to note this reference controls the PV unit as a voltage source, contrasting from most works. It was experimentally validated using a 3.5kVA microgrid. The strategy also uses a multi-loop strategy for the battery charging controller to limit PV generation and regulate the battery SoC and power. No anti-windup technique was used to avoid harmful situations when the battery limits are reached. Again, the strategy focuses on the battery charging limits and does not address discharging situations. Consequently, shedding loads is not a resource mentioned by the authors.

The control of an off-grid PV system with a battery is presented in Chtita *et al.* (2021). The power management method is developed for a DC off-grid system with PV generation aiming to control the power flow through 4 operation modes. Similarly to Mahmood, Michaelson and Jiang (2015), the operation modes comprehend situations when the PV unit has to reduce power to match the load and the battery limits. In addition, two extra operation modes are presented: night mode and off mode. The first one addresses situations where the PV unit is off and the battery can supply the load demand, while the second one comprehends situations where the load power is larger than the PV unit power and the battery discharging power, so some loads must be shed. The work validates the method through Matlab/Simulink simulations. In addition, the authors propose the use of a digital anti-windup technique in the PI controllers of the PV unit converter to ensure smooth transitions among operating modes. However, some limitations of this work may be pointed out. First, the studied system only regards DC load, so no inverter was employed. This limits the range of situations the method may reach, once most equipments are AC loads. Secondly, no converter was employed to connect the battery to the system. This limits the operating voltage of the system to the battery's nominal voltage and makes the power flow be controlled only by the PV unit converter. Finally, even though the authors consider the load disconnection in night mode, no load-shedding method is detailed.

An islanded microgrid unit composed of three generation sources is presented in Rezkallah *et al.* (2019). The unit is formed by a hybrid unit composed of a PV unit, a Wind turbine, and a BESS sharing the same DC-link, and a Diesel generator connected to the AC side of the grid. The grid works according to five operating modes depending on the load power, the PV + Wind power availability, and BESS conditions. Basically, if the generation power (PV+Wind) is larger than the load demand, the BESS absorbs the surplus power. Otherwise, if the load power is lower than the generation, the BESS injects power. When

the BESS can not absorb power because it is completely charged, a dump load is activated to leak the surplus power. On the other hand, if the load demand is larger than the generation and the BESS can not inject any power because it is completely discharged, the Diesel generator is activated to compensate for the lack. The dump load control algorithm employs a control scheme based on a PI anti-windup strategy. The limitations that may be pointed out about this work are similar to those presented previously. The authors do not use converters to connect the BESS. It again limits the DC-link voltage to the BESS nominal voltage. Further, reducing the generation power to match the low load demand shows to be more robust and realistic than using a dump load to absorb the surplus power the BESS can not absorb. Finally, grid-following strategies attached to an load-shedding method may be a good alternative to maintain the system stability than the use of Diesel generators in order to avoid non-clean generation sources.

In Mahmood and Blaabjerg (2022), the authors propose a power management strategy for coordinating multiple distributed energy storage systems (ESS) units with a PV and several droop-controlled units. The method achieves selectivity of the ESS units by prioritizing the charging of those with lower SoC conditions, while the others compensate for the load demand. This technique protects the ESS systems from overcharging and/or deep discharge by changing P - f droop reference according to the SoC conditions (MAHMOOD; BLAABJERG, 2022). Additionally, a power limiter PI control loop is proposed to limit the units' power to a maximum value. In this loop, the authors propose an anti-windup technique to avoid integration windup while the maximum power is not reached. Depending on the microgrid project, the use of several ESS units to compensate for the intermittent nature of PV systems might be unfeasible. The short lifetime of battery banks may require constant replacement, and consequently, it may increase the project cost. Also, the project price might be even higher due to the employment of several inverters for each ESS system.

In Behera and Saikia (2022), the authors propose power management for a grid-connected microgrid unit composed of a PV array and a hydrogen/bromine battery. The PV array and the battery feed the same DC-link through a boost converter and a bidirectional buck-boost converter, respectively. The DC-DC converters are controlled by tilt integral derivative (TID) controllers to track their references. The battery is responsible for compensating the microgrid needed power whenever the PV power is different from the load power by charging or discharging (BEHERA; SAIKIA, 2022). The PV unit control always extracts the maximum power through a close-loop TID strategy attached to an MPPT algorithm. Finally, the VSI control scheme employs an orthogonal signal generator-anti-windup filtered second-order generalized integrator (OSG-AWFSOGI) technique to extract from the grid the fundamental component regardless if the grid is under critical conditions like under-voltage, over-voltage, or severe harmonic distortions. Some comments may be extracted from this work. First, the authors employ a grid-following strategy for the inverter. It means that the controller follows the mains grid reference for controlling

the VSI. If some critical disturbance occurs making the protection system disconnect the system from the main grid, the microgrid is unable to operate in stand-alone mode. Further, the main grid fulfills critical situations of extreme unbalance between generation and load power, so no power curtailment or load-shedding is implemented. Additionally, the power management system does not consider the battery SoC regulation when the limits are reached. Further, the battery switching from charging to discharging mode is instantaneously performed according to the relation of the PV unit and load powers. It may cause undesired transients in situations of abrupt load change or abrupt change in PV power availability.

The work of Mahmood and Jiang (2019) proposes a power management coordination of islanded microgrids composed of three kinds of generation units: PV units, BESS units, and droop-controlled units. The strategy aims to keep the power balance respecting each unit's BESS limits and PV power capacity. It is based on multi-loop PI controllers to autonomously adapt the unit's power in order to match the load demand. This coordination is achieved through multi-segments power and frequency curves designed by the authors for the PV and BESS units without the need for any communication layer employment bib8. No need for communication links is an important advancement for islanded microgrid environments' reliability since they do not depend on link availability to perform accurately. However, the multi-loop approach proposed by the authors includes PI controllers with the objective of changing the operation set-points of the PV and BESS units to adapt the operation power whenever it is necessary to keep the power balance. Those controllers only act whenever the input variable crosses a pre-defined value. Then, while the unit operates in a "normal" operation state, the input errors of their controllers will never be null, causing integration windup. The authors do not mention the employment of any kind of anti-windup method in any of these controllers, but it seems to be strongly necessary.

An energy management system is studied in Michaelson, Mahmood and Jiang (2017) for an islanded microgrid structure formed by a PV unit and a BESS unit. The focus of this work is to propose a predictive load-shedding method to avoid or minimize the effects of outages through pre-emptive load-shedding actions, respecting the BESS' SoC limits. The method considers the PV unit's generation production forecast and the predicted load power demand to schedule load-shedding actions (MICHAELSON; MAHMOOD; JIANG, 2017). The management is performed through an Ethernet link with TCP/IP communication protocol to send signal information to PV and BESS controllers. As the focus of this work is to present an load-shedding technique for an islanded microgrid environment, the converters controllers are not detailed. Then, it is not possible to conclude if any anti-windup technique was employed. Further, it is possible to make some conclusions about the paper. Even though the proposed method is simply implemented, the simple dependence on communication links reduces the system's reliability when compared to autonomous multi-loop power management, and traditional load-shedding techniques.

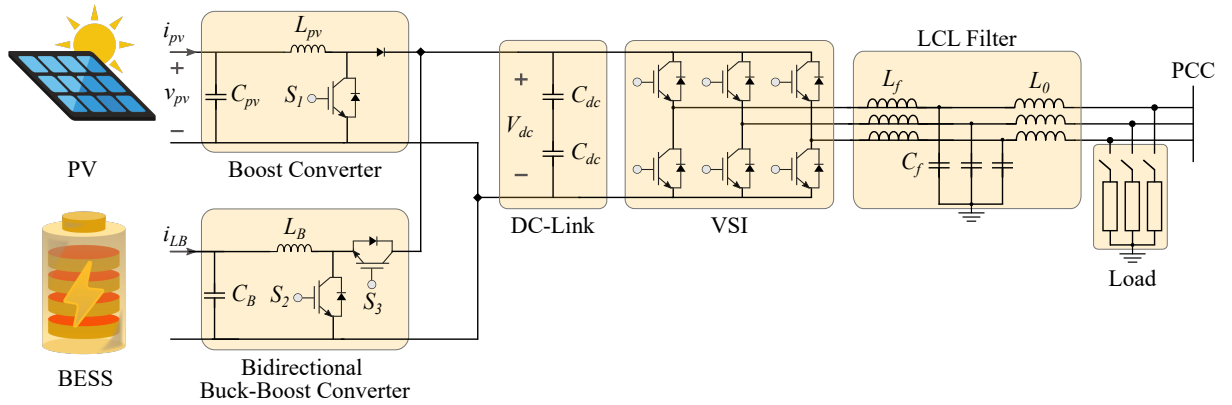
Finally, in Sadoudi, Boudour and Kouba (2021), the authors propose a multi-stage power management control for a multi-microgrid environment composed of multiple DG units. The units comprehend RES such as PV, Wind systems, and Diesel generators. Hybrid energy storage systems were integrated to contribute to frequency regulation during dynamic intermittent situations provoked by the RES systems. They comprehend electrical vehicles, fuel cells, redox flow batteries, and superconducting magnetic energy storage (SADOUDI; BOUDOUR; KOUBA, 2021). The strategy also includes an load-shedding scheme to deal with overload conditions or generator islanding. Therefore, the management of the power flow in the grid is performed with the integration of 3 coordinated stages: frequency and tie-line control stage as the first resource; energy storage system stage as the second alternative; and finally a smart load-shedding algorithm for extreme cases. Further, the authors propose the use of artificial intelligence (AI) based on Elephant Herding Optimization to improve the Fuzzy PID controllers of the second stage and to propose an improved load-shedding method at the third stage. On top of that, some comments may be concluded from this work. First of all, the management strategy is designed for multi-microgrid environments. It means that the multiple units need to communicate with a control center to operate. Once again, the communication link requirement reduces the system's reliability. Further, embedding robust AI algorithms may not be an easy task since it may require powerful computational effort. To conclude, the authors do not detail the units' systems controllers, so it is not possible to conclude the use of anti-windup strategies.

3 Microgrid Modeling

This chapter is dedicated to the modeling of the microgrid unit, including generation-side and grid-side elements. It starts with the PV unit and BESS, where mathematical models and equivalent electrical circuits are addressed. Then, it discusses DC-DC converters considering structural elements sizing and equivalent circuit presentation. The following subsections address grid-side elements such as VSI, LCL filters, and load models. All microgrid modeling was performed in Matlab/Simulink environment.

The microgrid unit studied in this work is depicted in Figure 2. The hybrid configuration comprehends the BESS and the PV array sharing the same capacitive DC-link through a boost converter and a bidirectional buck-boost converter, respectively. The use of a bidirectional converter provides more flexibility once it does not limit the DC-link voltage to BESS nominal voltage, prevents the BESS from harmful currents, and allows controllable charging/discharging. Further, the DC-link feeds a three-phase VSI, and then it is connected to the Point of Common Coupling (PCC) through an LCL filter to feed three-phase loads.

Figure 2 – Structure of the microgrid unit studied in this work.



Source: Adapted from Karimi, Oraee and Guerrero (2017).

The next subsections detail the modeling of each element.

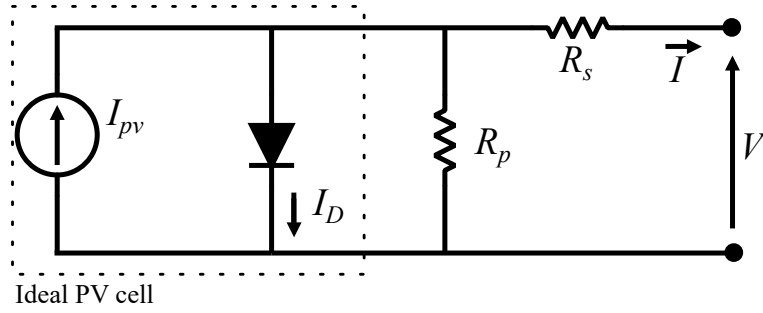
3.1 PV ARRAY AND BESS MODELING

This subsection describes PV arrays and BESS modeling, performed to obtain a good real-life equipment approach. The theoretical basis was consulted and studied to provide the simulation best possible reliability.

3.1.1 PV array

According to the theory, there are several forms of modeling PV cells (MOREIRA *et al.*, 2019). A PV cell is the basic device of a PV system. A group of PV cells forms together PV modules (VILLALVA; GAZOLI; FILHO, 2009). According to the theory of semiconductors, the I - V behavior of an ideal PV cell may be represented by a current source connected in parallel with a diode forming the single-diode model shown in Figure 3 (RAUSCHENBACH, 1980). This model provides an excellent real-life approach when it regards parallel (R_p) and series (R_s) resistances to simulate the current lack and voltage drop of a practical device, respectively (VILLALVA J.R. GAZOLI, 2009).

Figure 3 – Equivalent circuit of single-diode PV cell model.



Source: Adapted from Villalva J.R. Gazoli (2009)

From Figure 3 is possible to obtain the mathematical Equation (3.1) to represent the output current of a practical PV cell (I):

$$I = I_{pv} - I_D - \frac{V + R_s I}{R_p} \quad (3.1)$$

where I_{pv} is the electrical current generated by solar irradiance, I_D is the diode current, and V is the device output voltage.

Thus, I_{pv} is strongly influenced by environmental temperature and is linearly dependent on solar irradiance. The generated current is affected depending on light incidence on the device surface (VILLALVA; GAZOLI; FILHO, 2009). It is described by the Equation (3.2):

$$I_{pv} = [I_{pv,n} + K_I(T - T_n)] \frac{G}{G_n} \quad (3.2)$$

where $I_{pv,n}$ is the generated current under normal conditions (25°C and 1000 W/m², generally); K_I is the current coefficient parameter; T and G are actual temperature and solar irradiation on the device surface, respectively; T_n and G_n are the nominal temperature and solar irradiation, respectively.

As well known, the diode characteristic curve is defined by an exponential function. Therefore, according to the theory of semiconductors, I_D is defined by Equation (3.3):

$$I_D = I_0 \left[\exp \left(\frac{V + R_s I}{V_t a} \right) - 1 \right] \quad (3.3)$$

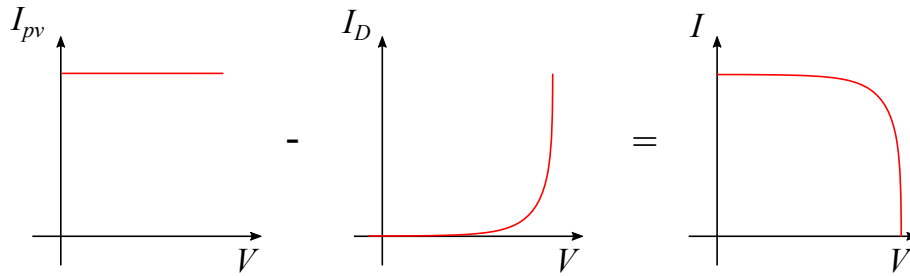
where I_0 , V_t are the saturation current, and thermal voltage, respectively, and a is the diode ideality constant. V_t may be computed using Equation (3.4), considering a PV module composed of N_s series-connected cells, the Boltzmann constant k ($1.3806503 \cdot 10^{-23}$ J/K) and electron charge q ($1.60217646 \cdot 10^{-19}$ C).

$$V_t = N_s \frac{kT}{q} \quad (3.4)$$

If the PV module is formed by N_p parallel-connected cells, generated and diode saturation currents must be expressed as multiples: $I_{pv} = N_p I_{pv,cell}$, $I_0 = N_p I_{0,cell}$. Therefore, series-connected cells increases array output voltage, while parallel-connected cells increases array output current (VILLALVA J.R. GAZOLI, 2009).

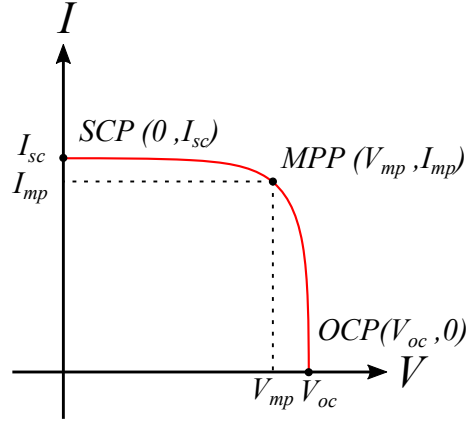
Once the equations are known, it is possible to obtain a PV module characteristic I - V curve, as depicted in Figure 4. From the resultant characteristic curve, three main points are highlighted: short circuit point (SCP), maximum power point (MPP), and open-circuit point (OCP). They are called by Villalva J.R. Gazoli (2009) *remarkable points*. The first one represents the point where maximum PV module current is obtained (short circuit current I_{sc}), and $V = 0$. The second represents the point where the maximum power is composed of maximum power voltage (V_{mp}) and maximum power current (I_{mp}). Finally, the last point represents the PV module maximum voltage (open circuit voltage V_{oc}), with $I = 0$. These three points are presented graphically in Figure 5.

Figure 4 – PV module characteristic I - V curve.



Source: Adapted from Villalva J.R. Gazoli (2009)

Once it is not easy to determine generated current without the influence of R_p and R_s , and the practical device's datasheet only informs short circuit current value at nominal conditions ($I_{sc,n}$), it is very common to assume it equals to PV short circuit current ($I_{pv} \approx I_{sc}$). Furthermore, it is still necessary to obtain diode saturation current I_0 . It is calculated through Equation (3.5), considering bandgap energy of the semiconductor E_g (in this case 1.12 eV for polycrystalline Si at 25°C) (CRISPIM; CARREIRA; CASTRO, 2007)(VILLALVA J.R. GAZOLI, 2009)(IMPROVEMENT... , 2006).

Figure 5 – I - V curve remarkable points.

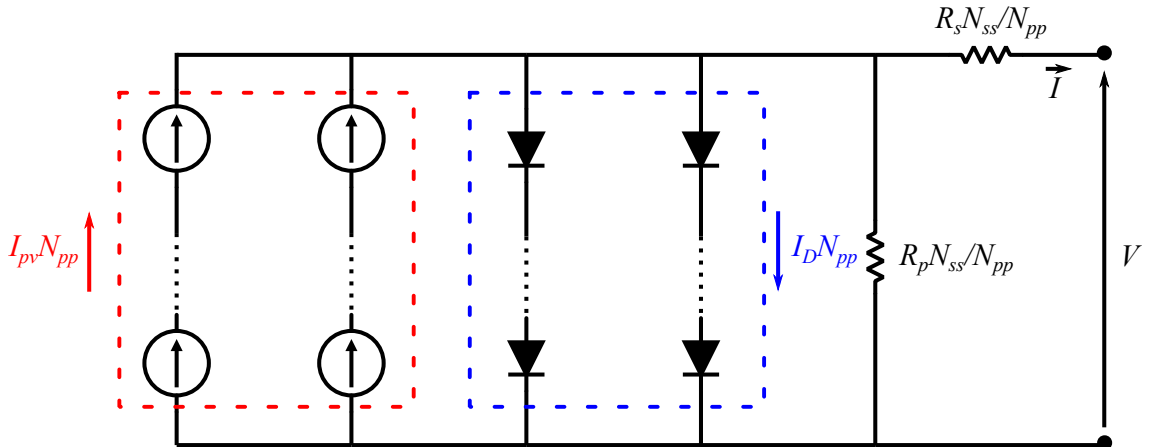
Source: Adapted from Villalva J.R. Gazoli (2009)

$$I_0 = I_{0,n} \left(\frac{T_n}{T} \right)^3 \exp \left[\frac{qE_g}{ak} \left(\frac{1}{T_n} - \frac{1}{T} \right) \right] \quad (3.5)$$

where $I_{0,n}$ represents saturation current at nominal conditions. It is calculated using Equation (3.6), considering I_{sc} , V_{oc} and V_t in the same conditions.

$$I_{0,n} = \frac{I_{sc,n}}{\exp \left(\frac{V_{oc,n}}{aV_{t,n}} \right) - 1} \quad (3.6)$$

As aforementioned, a PV module is formed by series or parallel-connected cells. Still, the group of PV modules forms a PV array, and they also may be series or parallel connected. Therefore, a set of N_{ss} series-connected and N_{pp} parallel-connected modules may be modeled according to the modified equivalent circuit presented in Figure 6.

Figure 6 – Modified equivalent circuit for $N_{pp} \times N_{ss}$ modules PV array.

Source: Adapted from Villalva J.R. Gazoli (2009)

3.1.2 BESS

Several studies have been performed to improve energy storage systems in many applications. Due to the best trade-off offered by Lithium-ion batteries, this technology has been widely used by many works (BARONTI *et al.*, 2014b). Lithium-iron-phosphate ($LiFePO_4$) batteries have been pointed out as one of the most promising technologies for energy storage systems once they are safer and cheaper than other lithium-based technologies.

There are several ways to model a $LiFePO_4$ battery. However, it is necessary to perform techniques to estimate its parameters. Battery SoC is a very important parameter to indicate charge level, once it is obtained from the relation between the current stored energy and the maximum energy the battery can store. It shows the percentage of stored energy in the battery, where 0% represents completely discharged and 100% is fully charged. So, one of the main characteristics of $LiFePO_4$ batteries consists of cell low operating voltage and almost flat open circuit voltage since SoC is between 20% and 90% (BARONTI *et al.*, 2013).

Baronti *et al.* (2013) performed several experiments to obtain analytical data and relate the SoC of a 20 Ah $LiFePO_4$ new battery to its open-circuit voltage V_{oc} . An intermediate curve obtained from these experiments was used in the present work to simulate the non-linear voltage behavior while charging or discharging (JUNIOR; BARROS; BARROS, 2021).

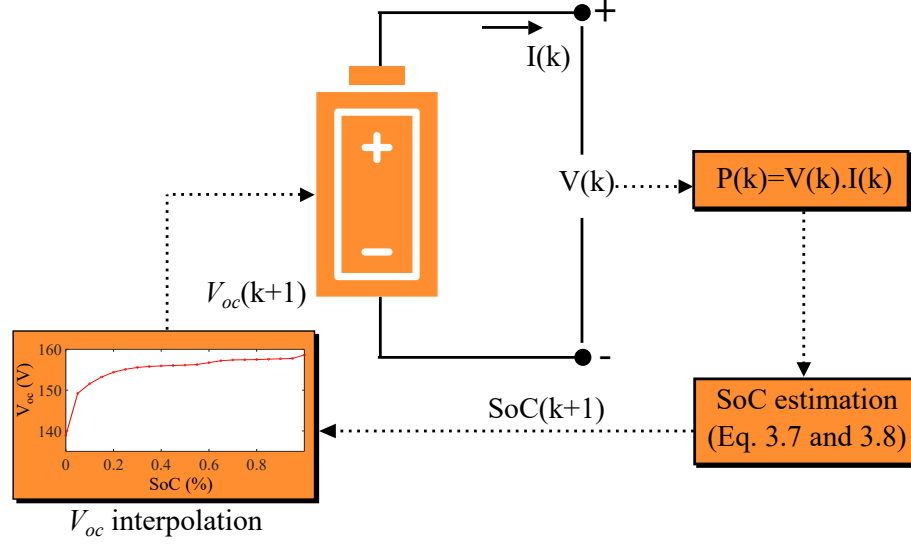
Therefore, Equations (3.7) and (3.8) were used to estimate SoC values depending on the power required to the battery:

$$SoC(k+1) = SoC(k) - \frac{\Delta k P(k)}{\eta_d E_b} \quad (3.7)$$

$$SoC(k+1) = SoC(k) - \frac{\Delta k P(k) \eta_c}{E_b} \quad (3.8)$$

where Δk is the sample time step; E_b is the energy capacity; η_c and η_d are charging and discharging efficiencies, respectively; $P(k)$ is the power requested from or to the battery. Case $P(k) > 0$, the battery is required to discharge, so Equation (3.7) is used. Otherwise, if $P(k) < 0$, Equation (3.8) is used to estimate SoC value.

The complete model used to simulate is presented in Figure 7, where the BESS is represented by an equivalent circuit model composed of an ideal controlled voltage source (JUNIOR; BARROS; BARROS, 2021). This voltage source follows reference V_{oc} obtained from the aforementioned interpolation curve, according to $P(k)$ calculation.

Figure 7 – Complete model of LiFePO_4 BESS.

Source: Adapted from Junior, Barros and Barros (2021).

3.2 DC-DC CONVERTERS

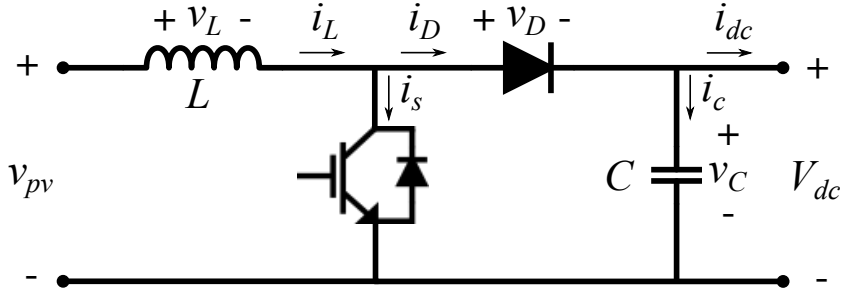
As aforementioned, the PV array and the BESS units are connected to a capacitive DC-link through DC-DC converters. The first uses a boost converter to provide a connection interface between PV arrays' low voltage and DC-link voltage (V_{dc}). The last ones are interfaced through a buck-boost bidirectional converter to allow power flow in two directions: charging and discharging. This subsection is dedicated to detail forenamed converters and their elements sizing.

3.2.1 Boost Converter

As noted by its name, a DC-DC boost converter "boosts" an input voltage to a higher level. Therefore its output voltage is always higher than the input, considering a steady-state operation (KAZIMIERCZUK, 2008). Figure 8 depicts boost converter characteristic circuit. It is composed of an inductor L , a filter capacitor C , a diode, and a power switch in this work represented by an Insulated Gate Bipolar Transistor (IGBT). Note that here the input voltage is represented by PV array voltage v_{pv} , and the output voltage is represented by V_{dc} .

The operation principle of DC-DC converters may be analyzed considering Continuous Conduction Mode (CCM) or Discontinuous Conduction Mode (DCM). For boost converter, CCM considers a not-null initial inductor current i_{L0} , since L is considered big enough not to let inductor current i_L reach zero within a switching period T . On the other hand, i_{L0} is zero in DCM, and i_L reaches zero before the switching period is finished. Note for both CCM and DCM, IGBT and diode are never turned ON at the same time, so, in steady-state, when one of them is ON the other is OFF. However, for DCM, when $i_L = 0$

Figure 8 – DC-DC boost converter characteristic circuit.



Source: Adapted from Rashid (2014).

and IGBT is off, diode current i_D reaches zero, turning the diode off (KAZIMIERCZUK, 2008).

Once the PV array is modeled through a controlled current source, as shown in subsection 3.1.1, i_L is considered here not to reach zero within a T period. Therefore, CCM is used to size boost components L and C . For this, it is important to understand boost current and voltage waveforms in CCM.

Initially, let's consider a T operation period, where IGBT is turned on for t_{on} seconds, and turned off for t_{off} seconds ($T = t_{on} + t_{off}$). So, boost duty-cycle D_{boost} may be given by $D_{boost} = t_{on}/T = 1 - t_{off}/T$. When IGBT is *ON*, diode is blocked, so its voltage $v_d = -V_{dc}$, the inductor voltage $v_L = v_{pv}$, and IGBT current $i_s = i_L$. Consequently, i_L rises in a v_{pv}/L slope until achieve its maximum value i_{Lmax} . Once IGBT is *OFF*, L operates as a current source turning the diode on. In this case, v_D is zero, and $v_L = v_{pv} - V_{dc}$, so i_L decreases in a $(v_{pv} - V_{dc})/L$ slope until reach its initial value. Figure 9 presents the described current and voltage waveforms (RASHID, 2014).

Considering i_L increasing from i_{L0} to i_{Lmax} during t_{on} , and decreasing from i_{Lmax} to i_{L0} during t_{off} , as shown in Figure 9, it is possible to conclude that:

$$v_{pv} = L \frac{\Delta i_L}{t_{on}} \quad (3.9)$$

$$V_{dc} - v_{pv} = -L \frac{\Delta i_L}{t_{off}} \quad (3.10)$$

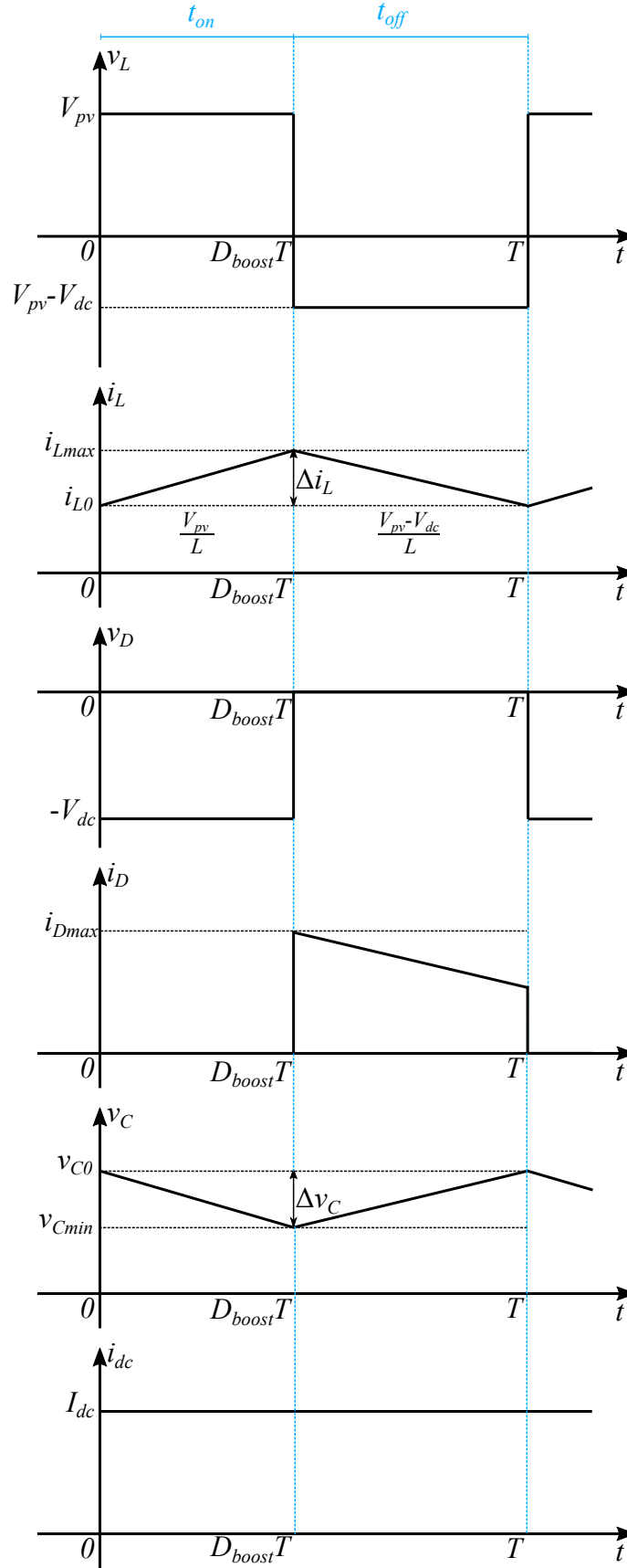
where Δi_L is the inductor current variation.

Isolating Δi_L in Equations (3.9) and (3.10) and making them equals is possible to reach Equation (3.11):

$$\frac{v_{pv} t_{on}}{L} = \frac{(v_{pv} - V_{dc}) t_{off}}{L} \quad (3.11)$$

Knowing that $t_{on} = D_{boost}T$ and $t_{off} = (1 - D_{boost})T$ and replacing it in Equation (3.11) we obtain Equation (3.12):

Figure 9 – Boost current and voltage waveforms for CCM.



Source: Adapted from Rashid (2014).

$$D_{boost} = \frac{V_{dc} - v_{pv}}{V_{dc}} \quad (3.12)$$

From Equations (3.9) and (3.10) is possible to obtain Equations (3.13) and (3.14):

$$t_{on} = L \frac{\Delta i_L}{v_{pv}} \quad (3.13)$$

$$t_{off} = L \frac{\Delta i_L}{V_{dc} - v_{pv}} \quad (3.14)$$

As aforementioned, switching period is given by $T = t_{on} + t_{off}$. Using Equations (3.12), (3.13) and (3.14) is possible to obtain boost inductance value L :

$$L = \frac{v_{pv} D_{boost} T}{\Delta i_L} \quad (3.15)$$

Furthermore, considering C is initially charged, during t_{on} , capacitor voltage v_C decreases from an initial v_{C0} to a minimum v_{Cmin} values. When IGBT is *ON*, capacitor current i_c is equal to load current i_{dc} . Considering its medium values I_c and I_{dc} , respectively, voltage variation in C may be given by:

$$\Delta v_C = \frac{1}{C} \int_0^{D_{boost}T} I_c dt = \frac{1}{C} \int_0^{D_{boost}T} I_{dc} dt = \frac{I_{dc} D_{boost} T}{C} \quad (3.16)$$

Isolating C , its value may be calculated using Equation (3.17):

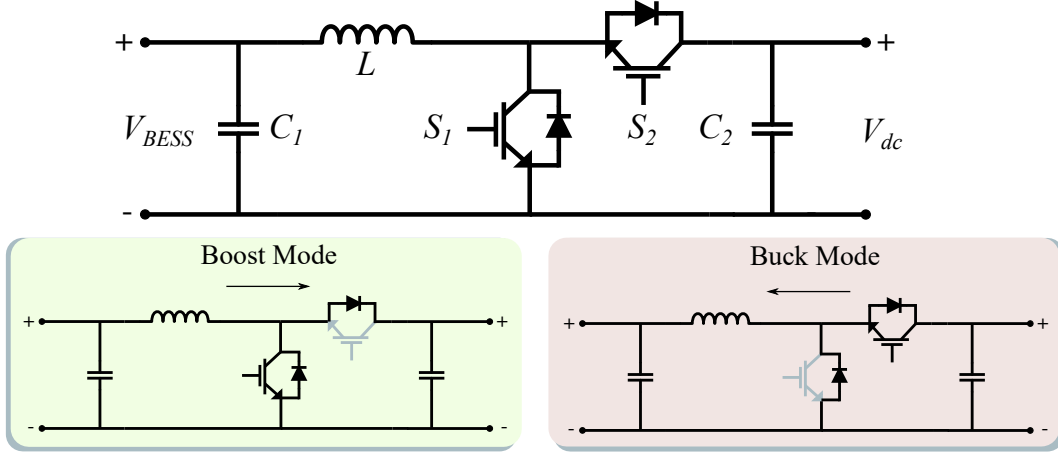
$$C = \frac{I_{dc} D_{boost} T}{\Delta V} \quad (3.17)$$

3.2.2 Bidirectional Buck-Boost Converter

A bidirectional DC-DC converter allows power transfer in two directions, from the high-voltage side (HVS) to the low-voltage side (LVS) and vice versa (SAHIN; TING, 2019). This configuration is very important once BESS needs to charge or discharge depending on microgrid's necessity. Thus, HVS is represented here by V_{dc} , while BESS voltage V_{BESS} stands for LVS. Figure 10 depicts a bidirectional buck-boost converter characteristic circuit. Note that this converter is a composition of two well-known DC-DC converters, boost, and buck. Therefore, the bidirectional converter operates in Boost Mode when BESS needs to discharge, and in Buck mode otherwise. Note that in the first mode, S_1 is switched while S_2 remains open, although in the last one, S_1 remains open while S_2 is switched.

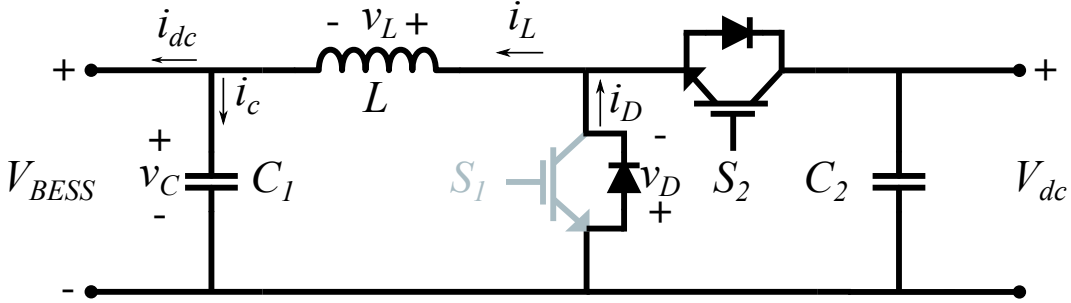
Boost operation mode was already described in previous subsection 3.2.1. Thus, bidirectional inductance L may be calculated through Equation (3.15) using BESS voltage V_{BESS} instead of v_{pv} , and capacitance C_2 is computed using Equation (3.17). Buck mode is going to be described considering Figure 11.

Figure 10 – DC-DC bidirectional buck-boost converter characteristic circuit.



Source: Adapted from Rashid (2014).

Figure 11 – Buck mode circuit detailed.



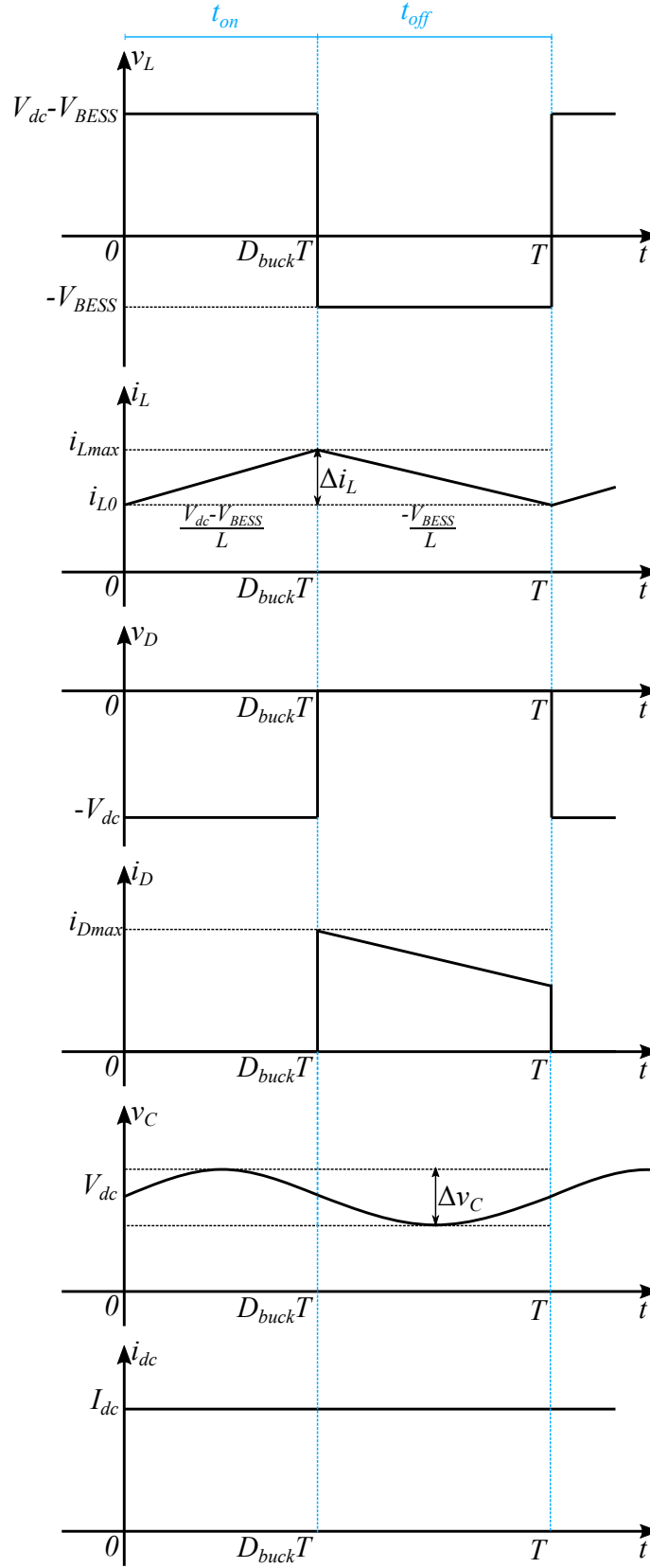
Source: Adapted from Rashid (2014).

In a buck converter, the output voltage is always lower than the input voltage. Here, for buck mode, both sides are represented by HVS and LVS, respectively. Hence, a buck converter "bucks" input voltage to a lower level (KAZIMIERCZUK, 2008). In the same way boost converter works, buck converter may be analyzed considering CCM and DCM.

Again, let's consider an operation period T composed of t_{on} and t_{off} when IGBT S_2 is turned *ON* and *OFF*, respectively ($T = t_{on} + t_{off}$). Buck duty-cycle is given by $D_{buck} = t_{on}/T$. Initially, during t_{on} , diode is blocked once its voltage is $v_d = -V_{dc}$. Once $v_L = V_{dc} - V_{BEES}$, i_L increases with a slope of $(V_{dc} - V_{BEES})/L$ until i_{Lmax} . When S_2 is turned off, i_L is not null, so current flow remains the same once L operates as a current source. In this case the diode is turned on, making $v_D = 0$ and $v_L = -V_{BEES}$. Therefore, i_L decreases with a slope of $-V_{BEES}/L$. While S_2 is *OFF*, L and C_1 work as an energy storage keeping current and voltage (KAZIMIERCZUK, 2008). The waveforms of aforementioned voltage and currents are presented in Figure 12 (RASHID, 2014).

Again, considering i_L increasing from i_{L0} to i_{Lmax} during t_{on} , and decreasing during t_{off} , it gives Equations (3.18) and (3.19):

Figure 12 – Buck mode current and voltage waveforms for CCM.



Source: Adapted from Rashid (2014).

$$V_{dc} - V_{BESS} = L \frac{\Delta i_L}{t_{on}} \quad (3.18)$$

$$-V_{BESS} = -L \frac{\Delta i_L}{t_{off}} \quad (3.19)$$

Isolating Δi_L in Equations (3.18) and (3.19) and making them equals gives Equation (3.20):

$$\frac{t_{on}(V_{dc} - V_{BESS})}{L} = \frac{t_{off}V_{BESS}}{L} \quad (3.20)$$

Knowing that $t_{on} = D_{buck}T$ and $t_{off} = (1 - D_{buck})T$ and replacing it in Equation (3.20), Equation (3.21) is obtained:

$$D_{buck} = \frac{V_{BESS}}{V_{dc}} \quad (3.21)$$

From Equations (3.18) and (3.19), t_{on} and t_{off} are computed through Equations (3.22) and (3.23), respectively:

$$t_{on} = L \frac{\Delta i_L}{V_{dc} - V_{BESS}} \quad (3.22)$$

$$t_{off} = L \frac{\Delta i_L}{V_{BESS}} \quad (3.23)$$

Replacing (3.22) and (3.23) in $T = t_{on} + t_{off}$ and using Equation (3.21) is possible to obtain L through Equation (3.24):

$$L = \frac{V_{dc}D(1 - D)T}{\Delta i_L} \quad (3.24)$$

Note bidirectional inductance may be obtained using Equations (3.15) or (3.24).

Using Kirchhoff's Current Law (KCL) is possible to note that $i_L = i_c + i_{dc}$. Disregarding i_{dc} variation ($\Delta i_L = \Delta i_c$), and considering C_1 medium current I_{c1} , current flowing in the circuit during $T/2 = t_{on}/2 + t_{off}/2$ may be expressed by Equation (3.25):

$$I_{c1} = \frac{\Delta i_L}{4} \quad (3.25)$$

Variation voltage in C_1 during $T/2$ is given by Equation (3.26):

$$\Delta v_c = \frac{1}{C_1} \int i_c dt = \frac{1}{C_1} \int_0^{T/2} I_{c1} dt = \frac{1}{C_1} \int_0^{T/2} \frac{\Delta i_L}{4} dt = \frac{\Delta i_L T}{8C_1} \quad (3.26)$$

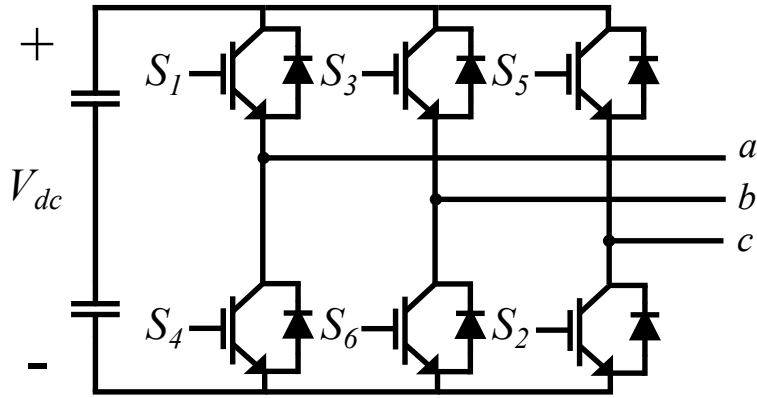
Isolating Δi_L in Equation (3.24), replacing it in Equation (3.26), then C_1 is given by Equation (3.27):

$$\Delta v_c = \frac{V_{dc}D(1-D)T^2}{8LC_1} \rightarrow C_1 = \frac{V_{dc}D(1-D)T^2}{8L\Delta v_c} \quad (3.27)$$

3.3 VSI

This work adopts a three-phase bridge VSI. An inverter converts voltage waveform from a DC source or an AC rectifier into a three-phase frequency-variable voltage output. The converter configuration presented in Figure 13 is composed of six power switches (here represented by IGBTs) working with freewheeling diodes. According to desired output waveform, the switches open and close in a proper sequence (AHMED, 1999).

Figure 13 – VSI configuration.



Adapted from Rashid (2014).

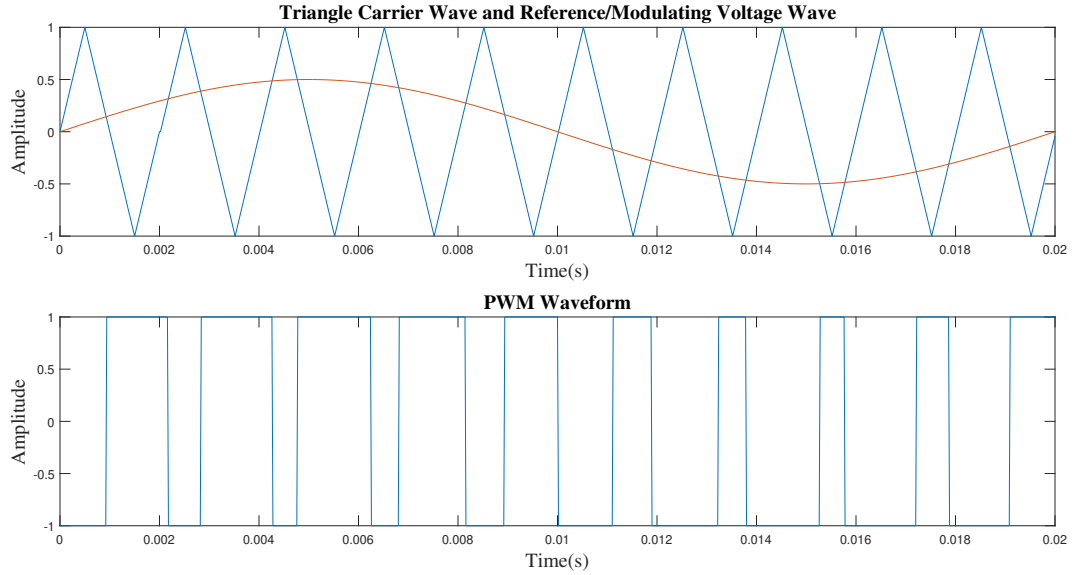
The IGBTs are divided into positive and negative groups. Switches S_1 , S_3 and S_5 form together the positive group, while S_4 , S_6 and S_2 compose the negative one. The connection of a positive with a negative switch in the way depicted in Figure 13 ($S_1 - S_4$, $S_3 - S_6$, $S_5 - S_2$) form inverter's "arms". Each arm provides an output phase current, so it is possible to obtain output phase and line voltages (AHMED, 1999). Note that switches of the same arm must not conduct at the same time to avoid V_{dc} shorting out. Therefore, the conduction signals of the negative group are complement of the positive.

3.3.1 Sinusoidal Pulse Width Modulation (SPWM)

In this work, the states of each IGBT are determined by an SPWM technique. In this strategy, VSI output voltage is determined by varying conduction times of each IGBT within a period. The PWM waveform is determined through the comparison between the reference (modulating) sinusoidal voltage (V^*) signal and a high-frequency triangle carrier waveform (Figure 14) (AHMED, 1999). When V^* is greater than the carrier wave, the IGBT connected to the positive group is turned on, otherwise, the negative group IGBT is activated. This principle is applied to each VSI phase since V^* considers a sine waveform with a 120° delay among phases. The frequency of the carrier determines the switching

frequency, while the modulation index is determined by the modulating signal amplitude. To illustrate, Figure 14 shows the comparison between a triangle carrier wave and the reference sinusoidal waveform, and the generated PWM waveform for switching the IGBTs in one phase.

Figure 14 – SPWM waveforms.



Adapted from Rashid (2014).

The modulation index (M) is determined to change the RMS output voltage since M is defined by the reference sinusoidal voltage amplitude (A_r) over the carrier triangle wave amplitude (A_c), as shown in Equation (3.28) (RASHID, 2014):

$$M = \frac{A_r}{A_c} \quad (3.28)$$

Then the output phase voltage is determined by equation (3.29):

$$V_g = M \frac{V_{dc}}{2}, \quad M \leq 1 \quad (3.29)$$

When $M \leq 1$, the controller operates in a linear region. It means that the maximum value of the phase output voltage V_g is $\frac{V_{dc}}{2}$ when $M = 1$. However, to increase the output voltage, the VSI may operate in a non-linear region. In these regions $M > 1$, then the inverter operates overmodulated. In overmodulation regions, V_g varies according to Equation 3.30 (RASHID, 2014):

$$\frac{V_{dc}}{2} < V_g < \frac{4}{\pi} \frac{V_g}{2} \quad (3.30)$$

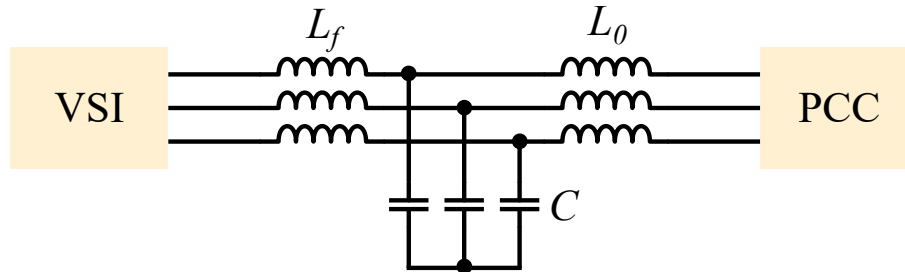
3.4 LCL FILTER

The VSI output signal generated by the PWM technique contains harmonics in fundamental frequency and its multiples (DURSUN; DÖŞOĞLU, 2018). Therefore, passive filters are necessary to mitigate harmonic currents and meet energy quality standards.

Literature addresses many passive filter topologies to solve this problem. First, and one of the most basic, L filter was proposed to attenuate harmonic currents. Although it works properly, this topology requires high inductance values, which cause a high voltage drop and affects the control time response. To meet this, a capacitance was incorporated forming a second-order LC filter, providing high-frequency attenuation. However, these filters present resonance frequency, and capacitor inrush currents (GOMES; CUPERTINO; PEREIRA, 2018).

Furthermore, third-order filters using an extra inductance form LCL filters as a more robust topology, providing higher filter volume, reducing inductor voltage drop, and higher harmonics suppression (KHAN *et al.*, 2022). The extra inductance also reduces capacitors' inrush currents. Thereby, this work uses a LCL topology between VSI and load as depicted in Figure 15, formed by source-side inductors L_s and load-side inductors L_g .

Figure 15 – LCL filter topology.



Source: Adapted from Khan *et al.* (2022).

It is important to highlight this topology also ensures microgrid unit output impedance is mainly inductive. This way, the traditional $P - f$ droop control strategy may be used in islanded microgrid operation mode described in Chapter 5.

3.5 LOAD MODEL

Many load models are considered in the literature, including static and dynamic models. The first one comprehends models that active and reactive power are modeled using instantaneous voltage magnitude and frequency, while the last models consider the instantaneous and previous voltage magnitude and frequency (VISCONTI, 2010).

This work consider a static constant impedance model, where active and reactive

Table 2 – Setup parameters.

Parameter	Symbol	Value	Unit
Nominal Voltage	E^*	127	V_{rms}
Nominal Frequency	f_0	60	Hz
Nominal DC-Link Voltage	V_{dc}	300	V
DC-Link Capacitances	C_{dc}	500	μF
Filter Capacitance	C_f	18	μF
Filter Inductances	L_f, L_0	3.6, 3.6	mH
Boost Capacitance	C_{pv}	53	μF
Boost Inductance	L_{pv}	11.8	mH
Bidirectional Capacitance	C_B	100	μF
Bidirectional Inductance	L_B	10	mH
PV array Power	P_{pv}	1725	W
PV array Nominal Maximum Power Point Voltage	V_{mpp}	189.75	V
PV array Nominal Maximum Power Point Current	I_{mpp}	9.1	A
PV array Open Circuit Voltage	V_{oc}	231.5	V
PV array Short Circuit Current	I_{sc}	9.6	A
BESS Power Limits	$P_{BESS,min}, P_{BESS,max}$	-500, 500	W
BESS Capacity	E_{bat}	20	Ah
BESS Voltage	V_{bat}	201.3	V
SoC Limits	SoC_{min}, SoC_{max}	20, 90	%

power are given as function of discrete time variable k by Equations (3.31) and (3.32), respectively:

$$P(k) = P_0 \left(\frac{V(k)}{V_0} \right)^2 \quad (3.31)$$

$$Q(k) = Q_0 \left(\frac{V(k)}{V_0} \right)^2 \quad (3.32)$$

where $P(k)$, $Q(k)$ and $V(k)$ are instantaneous load active power, reactive power and voltage, respectively; P_0 , Q_0 are steady-state active and reactive power, respectively.

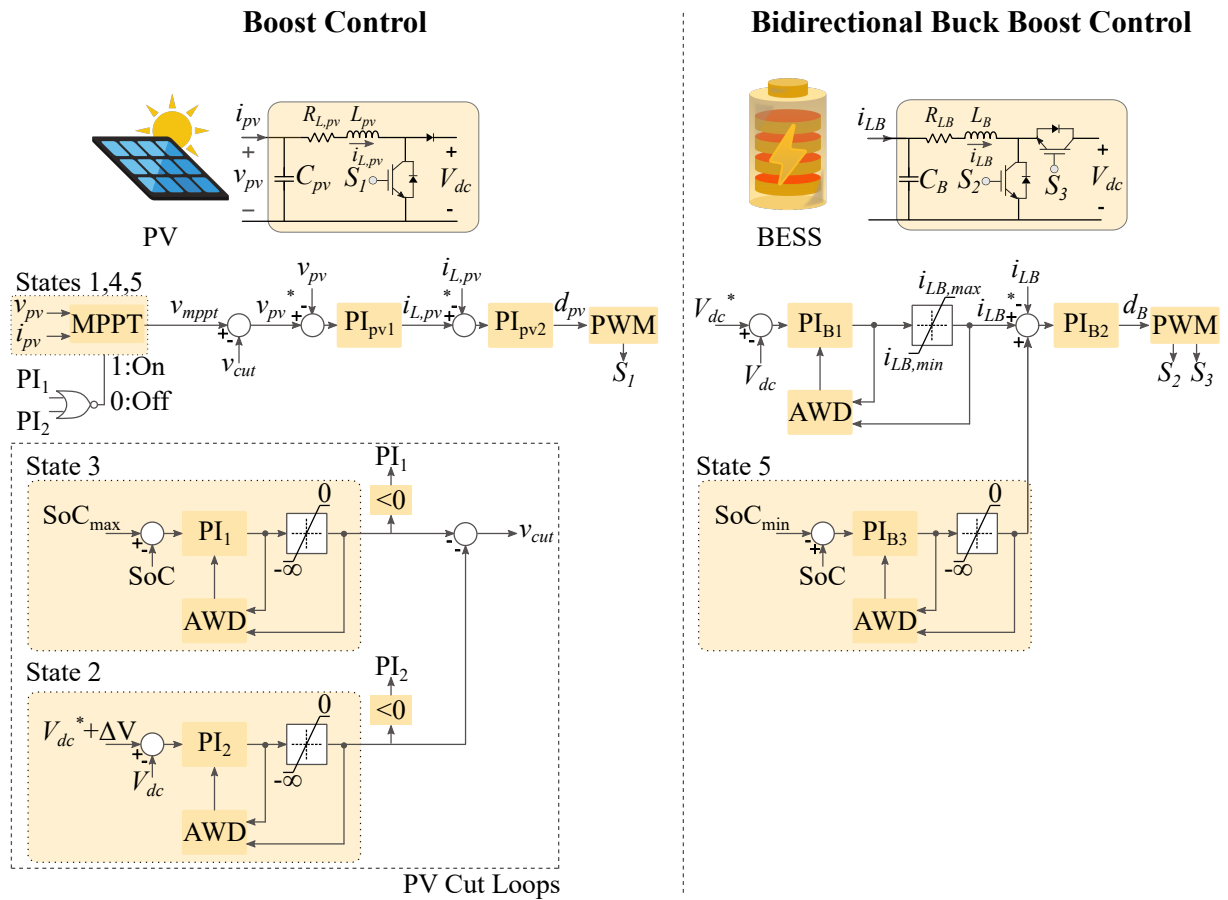
It is also important to highlight that the analysis of the results was performed considering resistive loads. The results comprise only active power analysis, and reactive loads are out of the scope of this work.

After the elements are modeled, Table 2 lists the microgrid parameters setup. The PV unit is composed of five series-connected solar modules of 345W, resulting in a 1725Wp nominal power at normal operating conditions. It means a constant 1000W/m² irradiance, and a constant temperature of 25°C. The data for modeling the array using experimental data obtained from the datasheet of a commercial module referenced as RSM72-6-345P by the manufacturer. The BESS was modeled with 61 series-connected lithium-ion cells of 3.3V. As mentioned in Chapter 3, the experimental data for the charging/discharging intermediate curve was obtained from Baronti *et al.* (2013), Baronti *et al.* (2014a).

4 Power Management Strategy

This chapter is dedicated to detailing the microgrid unit power management. The microgrid architecture studied in this work regards a critical situation where there is only one PV generation unit available attached to a BESS for power support. The BESS charges or discharges to compensate for the unbalance between generation and load. However, the strategy must respect the BESS limitations by preventing deep discharge or overcharging. For this reason, critical decisions must be taken to keep the power balance. When the BESS reaches charging limits by reaching the maximum SoC value or the maximum charging power, the PV unit has to reduce the injecting power to protect the BESS from overcharging. On the other hand, when the BESS reaches the minimum SoC value or the maximum discharging power, there is no other option for the microgrid system but to shed some load to keep the grid stable.

Figure 16 – DC-DC Converters control.



Source: Adapted Mahmood, Michaelson and Jiang (2012).

The balance between load and generation may be achieved through the multi-loop control strategy presented in Figure 16 attached to a load-shedding scheme. The multi-loop method is based on the works of Mahmood, Michaelson and Jiang (2012), and Soares

(2022). First, the DC-DC controllers are basically composed of a cascade closed-loop strategy with an outer voltage loop to track the reference voltage, and an inner current control loop to track the reference current generated by the voltage loop. Further, each controller includes parallel loops to change the operating setpoints. In this chapter, the microgrid behavior is described based on the actions of the multi-loop strategy controllers. Their designs and more details are presented in Chapter 5, and are not detailed here. Then, this chapter describes how the microgrid unit manages to keep the power balance through the aforementioned method.

First, the PV boost control depicted in the left side of Figure 16 tracks the Maximum Power Point (MPP) through a traditional Perturb and Observe method (discussed in Chapter 5), and generates the MPPT reference voltage (v_{mppt}). Whenever necessary, the PV cut loops composed of PI_1 and PI_2 change v_{mppt} through the power curtailment voltage (v_{cut}) to generate the PV unit reference voltage (v_{pv}^*). Then, the following outer and inner loops track v_{pv}^* to adjust the PV power. Secondly, the BESS buck-boost controller is tuned to regulate the DC-link voltage (V_{dc}) to a pre-defined reference value (V_{dc}^*). Likewise, whenever necessary, the BESS changes the operating point through the action of PI_{B3} . The details are presented in the next subsections.

It is very important to mention that the use of different loops to dynamically change the controllers' setpoints avoids the use of communication links. It means that the microgrid autonomously adapts to meet the load and maintain the power balance while keeping the BESS within a safe range of power and SoC. Further, to facilitate the understanding, the operation of the microgrid unit is divided into five states:

- State 1: normal operation;
- State 2: BESS charging limit;
- State 3: BESS maximum SoC limit;
- State 4: BESS discharging limit;
- State 5: BESS minimum SoC limit.

Note that the operation is completely autonomous and the state division represents an easy way to understand the method. The next sections explain how the unit operates in each operation state, propose improvements for multi-loop strategy, and present an improved load-shedding method.

4.1 OPERATION STATES

The following subsections explain how the unit behaves in each operation state, and how the controllers act to make the unit transit among them.

4.1.1 State 1 - Normal Operation

This state represents the normal operation where the unit is expected to work. It is considered the default operation state because the BESS operates within safe ranges of SoC and power. Therefore, in this state, the BESS bidirectional converter regulates V_{dc} to V_{dc}^* . Basically, when the PV unit power is greater than the load demand, V_{dc} tends to rise. The bidirectional controller then adjusts to make the BESS absorb the surplus power until V_{dc} is back to V_{dc}^* . On the other hand, when the load power is larger than the PV unit power, V_{dc} tends to decrease. Then, the bidirectional controller adapts to discharge the BESS until V_{dc} is regulated to the reference.

As the BESS works in safe regions, the PV unit is always regulated to deliver maximum power. First, as the SoC is considered here to be less than the maximum value SoC_{\max} , the input error of PI_1 is positive. The positive output signal is limited by the saturation block to zero, so the action of this controller remains idle. The same occurs to PI_2 . As the BESS regulates V_{dc} to V_{dc}^* , the input error will be always positive, so the positive output signal is saturated to zero. Thus, the control loops of the PV power controller remain idle in this operation state. It means that $v_{\text{cut}} = 0$. As there is no interference in the MPPT block, the PV unit is regulated in MPPT mode since $v_{pv}^* = v_{\text{mppt}}$.

To sum up, in the normal operation state the BESS regulates V_{dc} , and the PV unit injects the maximum power. The criteria for the unit exit this state are:

1. The BESS may not absorb more power for reaching the maximum charging power ($P_{\text{BESS},\min}$) by cause of a load decrease, or an increase PV power (due to an increase in irradiance or temperature decrease). Then, the unit changes to state 2;
2. BESS crosses maximum SoC threshold. Then the unit changes to state 3;
3. BESS delivers the maximum power ($P_{\text{BESS},\max}$) caused by a load increase or a decrease in PV power (due to a decrease in irradiance or temperature increase). In this case, the unit switches to state 4;
4. BESS crosses minimum SoC threshold. Then, the unit switches to state 5.

4.1.2 State 2 - BESS Charging Limit

The unit operates in this state when the BESS may not absorb any larger power. In order to protect the BESS from harmful high-charging currents, the bidirectional controller

limits the reference current generated by the voltage loop to a minimum value (i_{LB-min}). When the BESS is required to absorb a current lower than the limit, the BESS operates in a current control mode to regulate the BESS current (i_{LB}) to i_{LB-min} . The high availability of power delivered by the PV unit causes an increase in V_{dc} . When V_{dc} is larger than $V_{dc} + \Delta V$ the input error of PI_2 turns negative and consequently, the output signal is also negative ($v_{cut} \neq 0$). At this moment, a signal is sent to stop the MPPT block and hold the last calculated v_{mppt} value. The last value is subtracted from v_{cut} to drag the PV unit away from MPP. The value attributed to v_{cut} is properly tuned to make the PV unit cut enough power to regulate V_{dc} at $V_{dc} + \Delta V$ and keep the power balance. Here, ΔV is considered to be less than 5% of V_{dc}^* . The unit then works in state 2.

Finally, in state 2 the PV unit boost regulates V_{dc} whereas the bidirectional converter of the BESS controls the current to i_{LB-min} . The criteria for exiting this state are:

1. When a decrease in V_{dc} pushes the BESS power (P_{BESS}) away from $P_{BESS,min}$, or when $V_{dc} < V_{dc}^* + \Delta V$. It may happen due to an increase in load power or a greater decrease in PV power caused by natural resources (radiance or temperature). Then, the unit returns to state 1.
2. BESS reaches maximum SoC value. In this case, the input error of PI_1 is negative, causing a negative output that will drag even more v_{pv}^* away from the MPP. Then, the unit switches to state 3.

4.1.3 State 3 - BESS Maximum SoC

This state regards a situation where the BESS has reached the maximum SoC value. To prevent overcharging, the BESS must not absorb any further power. However, it is desired to dynamically drag the BESS current to zero rather than suddenly turn it off to avoid harmful transients when it is required to be connected again. In this case, the PV unit reduces the generation power until the BESS power is settled at zero.

When the SoC crosses the maximum value (SoC_{max}), the input error of PI_1 turns negative. The negative output signal of PI_1 turns the MPPT block off and drags v_{pv}^* away from the MPP. Then, v_{cut} dynamically changes v_{mppt} to reduce the PV power until the BESS power is settled in zero, and consequently, the SoC is regulated at SoC_{max} .

In this state, the BESS regulates the current at zero while the PV unit reduces power to regulate the SoC at SoC_{max} and V_{dc} at V_{dc}^* . The unit exit this state when:

1. A load increase or PV power decrease causes the load power to be higher than PV power. The BESS controller adjusts i_{LB} to a positive value, making the BESS

discharge. As soon as SoC is lower than SoC_{\max} , the PV returns to MPPT. The microgrid unit then returns to state 1.

4.1.4 State 4 - BESS Discharging Limit

In this state, the BESS has reached the discharging power limit. It may happen due to a really high increase in the load power. But in a real system, it is more likely to happen due to a decrease in the PV power caused by natural reasons like irradiance decrease or temperature increase. Still, the control system must limit the operating power to prevent BESS damage caused by high currents. First, the BESS' bidirectional converter limits the discharging current to a maximum safe value $\beta_{LB-\max}$. However, this is still not sustainable since the high unbalance between load and generation may provoke voltage and frequency deviations. It is also detected that V_{dc} decreases when the load power is greater than the PV power plus the BESS discharging power. In these cases, there is no other option for the system but to shed non-critical load attempting to keep the power balance.

In this work, an improved method for shedding loads is proposed and it is explained later in this chapter where V_{dc} level is used as a trigger to shed loads. When V_{dc} drops below $V_{dc} - \Delta V$, the proposed strategy detects the unbalance and starts shedding loads until V_{dc} is regulated at a safe value.

The criteria for exiting this state are described below.

1. As soon as enough load is shed to keep the power balance and the V_{dc} is regulated again the unit returns to state 1.
2. When not enough loads were shed and the SoC reaches the minimum value (SoC_{\min}), the unit then changes to state 5.

4.1.5 State 5 - BESS Minimum SoC

State 5 represents a situation where the BESS' SoC has reached the upper threshold. The control system must protect the BESS from harmful deep discharging. Again, it is not desirable to instantaneously turn the battery off, but to dynamically drag the BESS power to zero. The work of Mahmood, Michaelson and Jiang (2012) does not comprehend such a situation once it regards SoC_{\min} regulation as part of the BESS protection system. Then, a new control loop is proposed by the LASID research team (SOARES, 2022). It is here represented by PI_{B3} . This control loop acts directly in the bidirectional converter control to change the reference current of the inner loop. While the SoC is greater than SoC_{\min} , the positive input error generates a positive output signal which is saturated to zero. It means that when the SoC is at a safe range, this loop does not affect the controller.

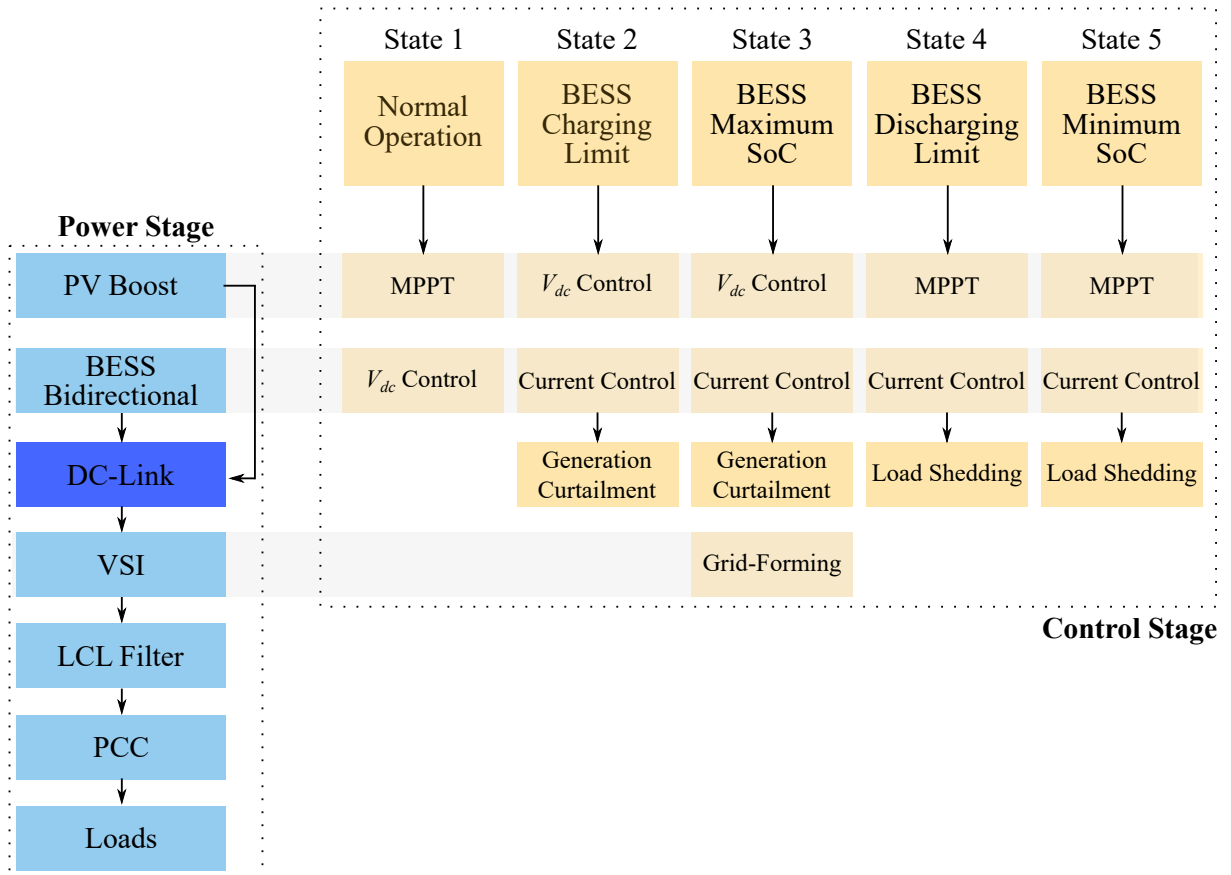
However, when the SoC crosses SoC_{\min} , the action of PI_{B3} dynamically drags i_{LB}^* to zero until the SoC is regulated at SoC_{\min} .

Furthermore, it is important to mention that leading the BESS from the grid increases the unbalance between PV power and load. Therefore, this strategy must be attached to the strategy to shed loads to keep the balance. When the BESS power leads to zero, V_{dc} tends to decrease. Like in state 4, this decrease is detected by the proposed method for shedding loads to disconnect non-critical load until the balance is reestablished.

Then, the criteria for exiting this state are:

1. The shedding of loads or a natural decrease in critical loads was enough to regulate V_{dc} until SoC is greater than SoC_{\min} . Then, the unit returns to state 1.

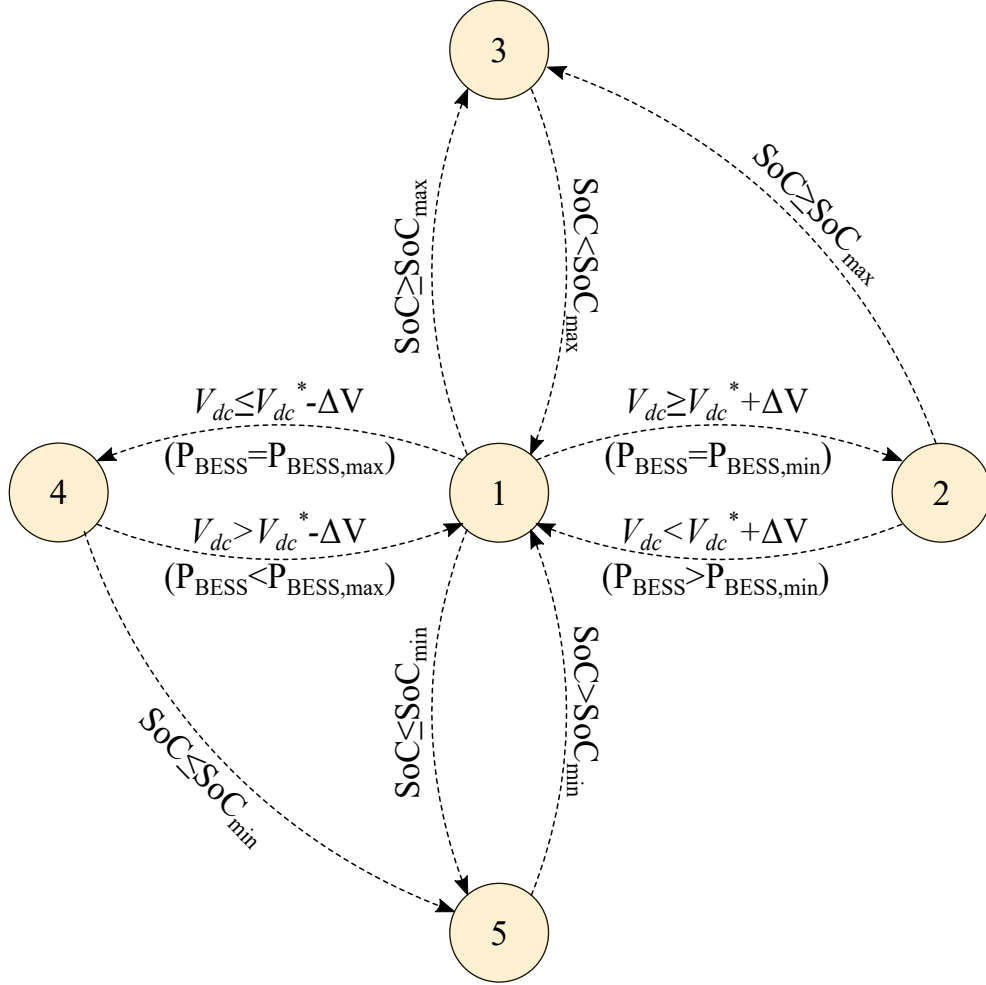
Figure 17 – Microgrid control flowchart.



Source: Made by the author.

To facilitate the understanding, Figure 17 gathers the control modes each converter assumes when the unit operates in each state. Note that the VSI assumes a grid-forming strategy regardless of the operation state. This strategy is detailed in Chapter 5. Furthermore, Figure 18 depicts a scheme with the states transitions criteria.

Figure 18 – States transitions criteria.



Source: Adapted from Karimi, Oraee and Guerrero (2017).

4.2 PROPOSED IMPROVEMENTS

As previously mentioned, the division into operation states is a didactic way of understanding how the microgrid unit adapts to keep the power balance. All transitions occur autonomously and without the need for communication layer employment. However, during the transitions from one operating state to another, undesired transients may appear, exposing the generation devices to harmful current and voltage oscillations. For this reason, it is crucial to ensure smooth transitions when the control system adapts to meet the load demand.

It is natural to note that the multi-loop strategy presented in Figure 16 uses several PI controllers. PID controllers have been widely used in many processes due to their well-established implementation and tuning methods (ÅSTRÖM; HÄGGLUND, 2006). Nevertheless, it is crucial to consider the drawbacks those controllers may present. Whenever the actuators reach physical limitations, the system is incapable of correcting steady-state errors. However, the integration action of PID controllers will continue integrating non-null input errors indefinitely, driving the controller output signal far away from the correct

operating point. As mentioned in section 1, this phenomenon is called integration windup.

During tests of the aforementioned power management strategy, several undesired transients were witnessed during the states' transitions. Observing the PI controllers' output signals, it was detected that most of them suffered from integration windup. It causes not just large delays in the controllers' actions, but high voltage and current oscillations that may be extremely harmful to the microgrid system. The authors that proposed the multi-loop management for states 1, 2, and 3 mention the use of an anti-windup (AWD) strategy only in PI_1 . But, integration windup situations were also detected in PI_2 and PI_{B1} . Further, the control loop for SoC regulation in state 5 proposed by the LASID research team also needs an AWD strategy to avoid misbehavior. The reasons why AWD strategies are crucial in each of those controllers are explained in the following paragraphs.

First, whenever the BESS works within a safe SoC range, the input errors of PI_1 and PI_{B3} are not null until the BESS is charged or discharged. As previously mentioned, these controllers are limited by a saturation block to limit their action to specific moments. However, the integrator action continues to integrate a non-null error. If the unit operates in state 1 for a long period, the output signals of PI_1 and PI_{B3} increase until SoC reaches SoC_{max} or SoC_{min} , respectively. It drives the controller's signal far away from the operating point. When the BESS crosses one of the thresholds, the controller must return to the operating point to send the correct signal. Depending on how long the integrator has integrated a non-null error, it may take a long time. The delay caused by the integration windup may expose the BESS to harmful overcharging (PI_1) or a deep discharge (PI_{B3}). For these reasons, the employment of AWD methods in both PI_1 and PI_{B3} is extremely necessary to ensure a smooth and fast transition from state 1 to state 3, and from state 1 to state 5, respectively. The authors who proposed the power management for states 1, 2, and 3 mention the use of clamping AWD technique in PI_1 , but do not discuss the consequences of not using it. Further, no AWD technique in PI_{B3} was mentioned in (SOARES, 2022).

A similar situation occurs in PI_2 during the transition from state 1 to state 2. During normal operations, the BESS bidirectional control regulates V_{dc} to V_{dc}^* . It is easy to note that the input error of PI_2 when the unit operates in state 1 is not zero, since the reference value is $V_{dc}^* + \Delta V$. The saturation block keeps this controller idle during normal operation, but the non-null error continues to be integrated. Again, PI_2 controller suffers from windup when the unit does not work in state 2. It causes a delay during the transition from state 1 to state 2, and an undesired increase in V_{dc} .

Finally, the undesired windup is also witnessed during the transition from state 2 to state 3. As mentioned before, PI_1 suffers from windup most of the time while the SoC is in a safe value. However, even if an AWD technique is employed in PI_1 , when SoC reaches SoC_{max} and the unit works in state 2, undesired transients may happen. It occurs

because in state 2 V_{dc} is regulated to $V_{dc}^* + \Delta V$, but the input reference of PI_{B1} is V_{dc}^* . For this reason, the input error of PI_{B1} is not null, causing integration windup in this controller. Likewise, the harmful transients caused by the windup include current and voltage oscillations that may damage the system.

4.2.1 Anti-Windup Strategies

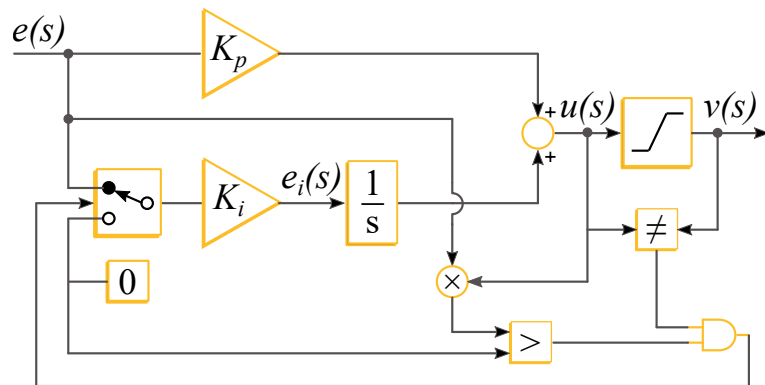
Therefore, this work proposes the use of an AWD scheme in PI_1, PI_2, PI_{B1} and PI_{B3} to ensure smooth transitions. Further, two well-known AWD techniques were tested in each of those controllers, and their performance was analyzed. The next paragraphs present how each AWD techniques work.

4.2.1.1 Clamping Anti-Windup

The Clamping Anti-Windup (CAW) strategy instantaneously turns the integrator off when it is no longer necessary. Because of that, this technique may also be called Conditional Integration Anti-Windup (JALIL *et al.*, 2021). Figure 19 depicts the diagram blocks of a PI controller with CAW. Then, the integrator input is equal to the input error times the integral gain (K_i) only when the actuator has not reached the limit. The integration is switched off when:

1. The PI controller output signals before ($u(s)$) and after ($v(s)$) the saturation block are different. It proves that the control has reached the clamping saturation limit.
2. The input error ($e(s)$) and $u(s)$ have equal signals. It means that $e(s)$ is not zero and the controller is trying to push it even more away from the reference.

Figure 19 – PI controller with CAW scheme.



Source: Adapted from Jalil *et al.* (2021).

When the two criteria are satisfied, the input of the integral gain block is switched to zero. The control integrator law of integrator input signal ($e_i(s)$) is defined by equations (4.1) and (4.2) (HANUS, 1980b):

$$e_i(s) = K_i e(s), \text{ if } u(s) = v(s) \text{ and } e(s)u(s) < 0 \quad (4.1)$$

$$e_i(s) = 0, \text{ if } u(s) \neq v(s) \text{ and } e(s)u(s) > 0 \quad (4.2)$$

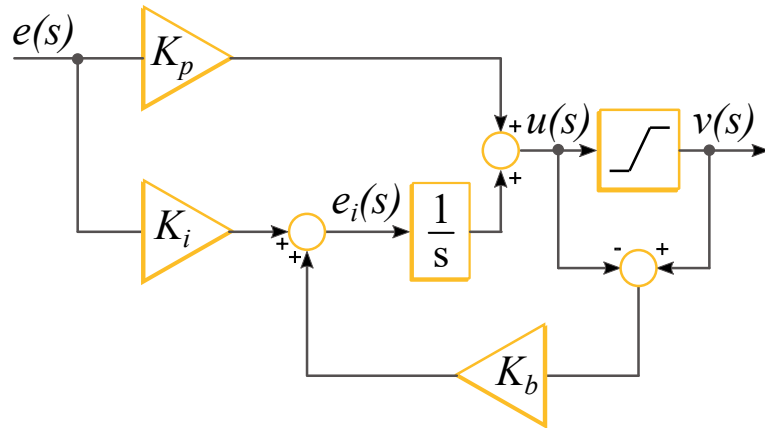
4.2.1.2 Back-Calculation Anti-Windup

Figure 20 depicts the diagram block of the Back-Calculation Anti-Windup (BCAW) strategy. In the BCAW method, the integrator input is dynamically reset when the actuator reaches the saturation limit. It consists of a feedback path to reduce the integrator input whenever is needed. The difference between $v(s)$ and $u(s)$ is computed, and feeds the integrator input through a feedback gain K_b (ÅSTRÖM; HÄGGLUND, 2006). Then, the integrator input is:

$$e_i(s) = K_i e(s) + K_b [v(s) - u(s)] \quad (4.3)$$

When the saturation limit is not reached, then $u(s) = v(s)$ and $e_i(s) = e(s)K_i$. On the other hand, when $u(s) \neq v(s)$, the integrator input is dynamically reset at the rate imposed by K_b (ÅSTRÖM; HÄGGLUND, 2006; ÅSTRÖM; RUNDQWIST, 1989). According to Astrom and Rundqwist (1989), K_b taken equal to K_i or $K_b = 0.8K_i$ gives a good response from impulse disturbance. The present work takes $K_b = K_i$ with a satisfactory outcome.

Figure 20 – PI controller with BCAW scheme.



Source: Adapted from Astrom and Rundqwist (1989).

4.2.2 Proposed Load-Shedding Scheme

In states 4 and 5, the microgrid unit must shed loads in order to maintain the grid stable. Here, the proposed load-shedding scheme is described. It improves a scheme that uses the V_{dc} level as a trigger for shedding loads presented by Soares (2022). First, the method must be sure that there is a high unbalance between generation and load. When

the load demand is higher than the PV power and the BESS may not inject power, the V_{dc} level drops. However, instantaneously shedding some loads whenever the V_{dc} drops below a pre-defined threshold is not desired since it may be susceptible to over-shedding. Then, two methods are employed to ensure unbalance detection:

1. A simple moving average (SMA) calculation is employed in V_{dc} measurement to avoid high variations;
2. The V_{dc} SMA value must drop below the limit for at least 100ms. If the V_{dc} SMA level is below the limit for 100ms, then the unbalance is confirmed.

Secondly, the methodology divides the microgrid loads into two categories: critical and non-critical. Critical loads represent those that may not be shed at any cost, while non-critical loads are those that may be shed in critical situations, such as a deep decrease in the PV power availability caused by low irradiance or high temperatures. Further, non-critical loads are hierarchically divided using a prioritization approach. Once a critical unbalance is detected, the less important loads are shed first. The less priority non-critical load L_{NC1} is firstly shed, followed by the next less priority L_{NC2} , and so on. The flowchart of the proposed algorithm is presented in Fig. 21, and explained in the next paragraphs.

Before explaining the algorithm, it is important to explain some terms:

- Timer_0 is the timer used to count how much time V_{dc} is below the range;
- Timer_1 is the timer used to count how much time has passed since L_{NC1} was shed;
- Timer_2 is the timer used to count how much time has passed since L_{NC2} was shed;
- Timer_N is the timer used to count how much time has passed since L_{NCN} was shed;

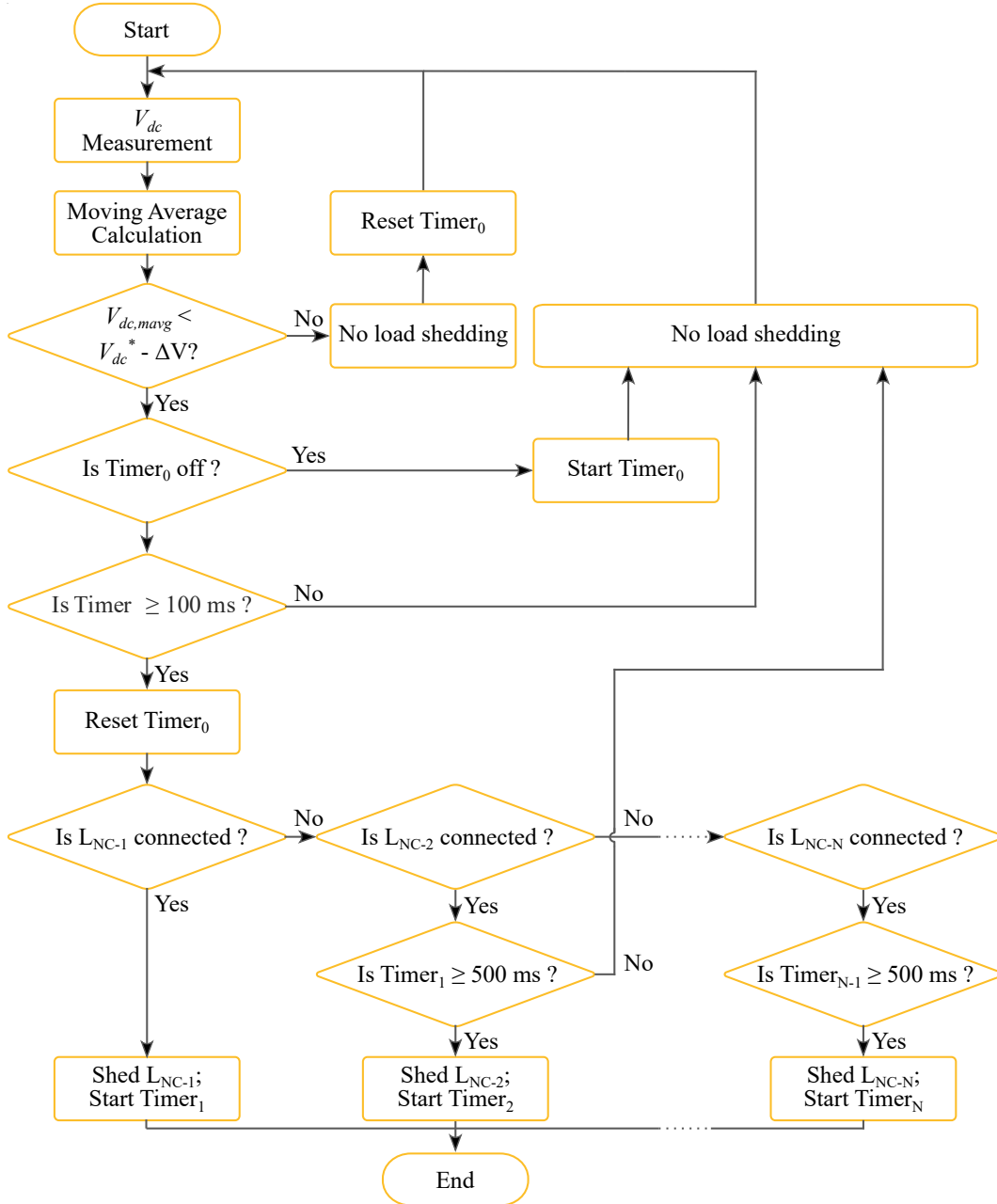
To start, the method measures V_{dc} level and computes an SMA according to equation (4.4) (4.4):

$$V_{dc,avg-k} = \frac{1}{k} \cdot \sum_{i=n-k+1}^n V_{dc-i} \quad (4.4)$$

where $V_{dc,avg}$ is V_{dc} SMA, k is the window size and n is the total observed values. The window size adopted in this work corresponds to the last 100 ms of V_{dc} measurements.

Then, if $V_{dc,avg}$ is not below $V_{dc}^* - \Delta V$ limit, no load is shed. As aforementioned, the strategy must be sure that the detected low $V_{dc,avg}$ represents a power unbalance. It only makes a load-shedding decision if $V_{dc,avg}$ is out of range for at least 100 ms. The maximum V_{dc} variation limit ΔV is the same adopted in state 3, being less than 5% of V_{dc}^* . If $V_{dc,avg} < V_{dc}^* - \Delta V$, and the timer has not started yet, it means that $V_{dc,avg}$

Figure 21 – Proposed load shedding strategy flowchart.



Source: Made by the author.

is out of range, but it is not necessarily caused by microgrid power imbalance. In this case, the algorithm starts Timer_0 , no load-shedding is performed, and it returns to a new measurement. If the $V_{dc,mavg}$ is within safe limits, no load is shed and Timer_0 is reset. Otherwise, if $V_{dc,mavg}$ is still lower than $V_{dc}^* - \Delta V$, but Timer_0 has not reached 100 ms yet, no load shedding is performed. Still, if $V_{dc,mavg} < V_{dc}^* - \Delta V$ and Timer_0 has reached 100 ms, it means that the V_{dc} is below the limit for a long time, so the microgrid power unbalance is confirmed. In this case, some load must be shed.

As previously mentioned, the non-critical loads are ranked hierarchically. Once the power unbalance is confirmed, Timer_0 is reset, and the strategy checks if the less ranked

non-critical load (L_{NC1}) is connected. If the answer is yes, L_{NC1} is shed, and another timer ($Timer_1$) is started to inform how much time has passed since that load was shed. The next time an imbalance is detected, the algorithm will check if the next non-critical load is connected. To avoid abrupt load-shedding, the next non-critical load will only be shed if it's been at least $500ms$ since the last non-critical load was shed (KEIVANIMEHR *et al.*, 2021). If the next non-critical load is shed, a new timer is started ($Timer_2, Timer_3, \dots, Timer_N$).

This strategy may be applied for N hierarchically ranked non-critical load, with an adjustable delay for imbalance detection and between sheddings. As it is based on V_{dc} , this technique may be called Under-DC-Link Load Shedding ($UV_{dc}LS$).

5 Control Systems

This chapter presents DC-DC converters control designs and the VSI grid-forming control. First, it details closed-loop boost converter control, including Perturb and Observe MPPT method. Then, it addresses closed-loop bidirectional buck-boost control. Finally, it describes the grid-forming strategy based on droop control for the VSI, including secondary frequency and voltage regulation.

5.1 PV BOOST CONTROL

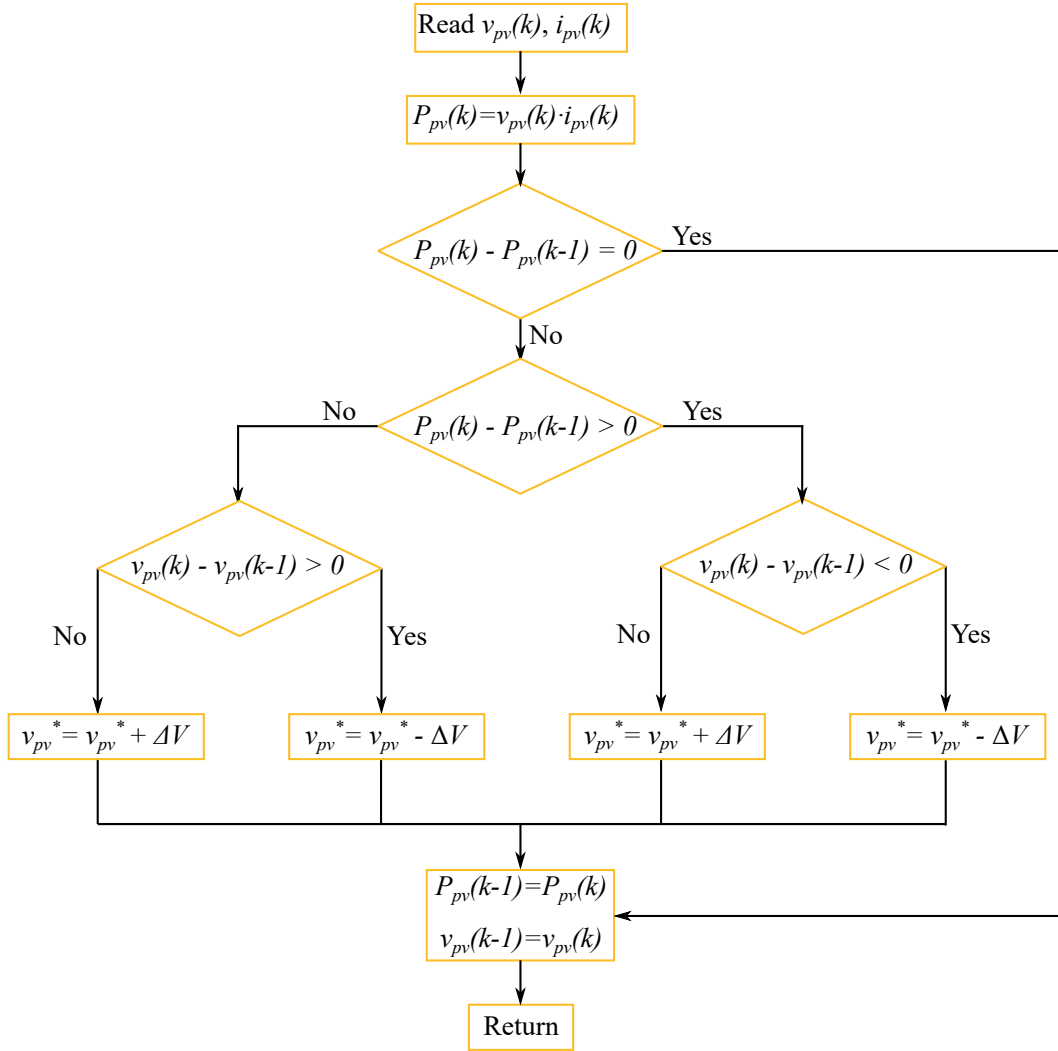
As presented in Figure 16, the boost control comprises an MPPT technique attached to a cascade closed-loop strategy to track the maximum power available to the PV unit. Power loops controllers adapt the PV power when it is required to operate in states 2 or 3. The following subsections detail the MPPT method and the close-loop controllers' designs.

5.1.1 Perturb and Observe MPPT

This work uses a traditional Perturb and Observe (P&O) MPPT method. It is widely used in literature due to its implementation simplicity and efficiency. It consists in a perturbation of PV array voltage (v_{pv}) to observe the output PV array power (P_{pv}). The perturbation is performed by incrementing, maintaining, or decrementing PV array reference voltage (v_{pv}^*). If the perturbation makes P_{pv} rise, the algorithm keeps perturbing in the same direction (ABID *et al.*, 2019). The algorithm flowchart of P&O is presented in Figure 22.

The algorithm starts reading v_{pv} and PV array current i_{pv} to compute the current value of P_{pv} . This value is compared to the previous power value, indicated by the discrete-time variable k . If they are equal, the method saves the latest value and returns to the beginning. Otherwise, it checks if P_{pv} is larger or lower than its previous value. Case it is larger, it means that output power is rising, so the algorithm keeps perturbing in the same direction by comparing v_{pv} with the previous value. Then, it keeps increasing ($v_{pv}(k) > v_{pv}(k-1)$) or decreasing ($v_{pv}(k) < v_{pv}(k-1)$) v_{pv}^* value. However, if P_{pv} is lower than its previous value, the algorithm changes the perturbing direction. The increment step for V_{pv}^* is represented by ΔV . Once v_{pv}^* is updated, algorithm also updates P_{pv} and v_{pv} previous values, then returns to the beginning.

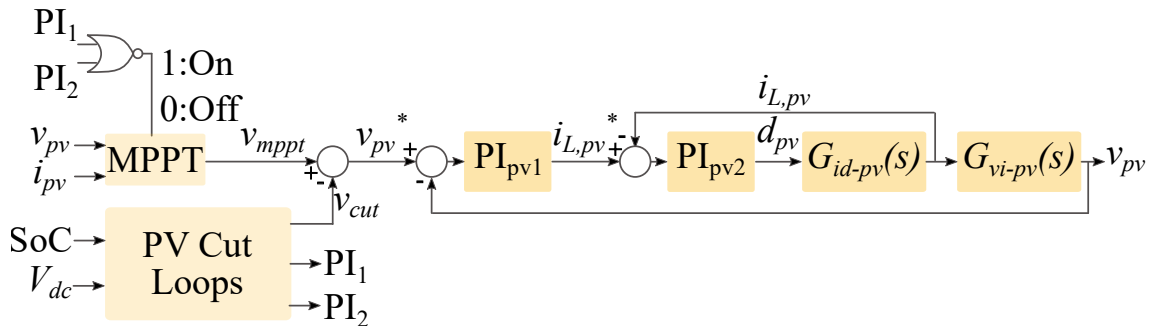
Figure 22 – P&O algorithm flowchart.

Source: Adapted from Abid *et al.* (2019).

5.1.2 Control Design

Attached to the P&O algorithm, the closed-loop strategy tracks v_{pv}^* . This strategy counts with outer voltage and inner current PI loops as presented in Figure 23.

Figure 23 – Boost converter control.



Source: Adapted from Mahmood, Michaelson and Jiang (2012).

Boost converter model average dynamic equations were detailed by Middlebrook e

Cuk (1976), and are given by equations (5.1) and (5.2) for boost IGBT switch S_1 closed:

$$L_{pv} \frac{di_{L,pv}}{dt} = -R_{L,pv} i_{L,pv} + v_{pv} \quad (5.1)$$

$$C_{pv} \frac{dv_{pv}}{dt} = -i_{L,pv} + \frac{V_{eq} - v_{pv}}{R_{eq}} \quad (5.2)$$

For S_1 open, Equations (5.3) and (5.4) are obtained:

$$L_{pv} \frac{di_{L,pv}}{dt} = -R_{L,pv} i_{L,pv} + v_{pv} - V_{dc} \quad (5.3)$$

$$C_{pv} \frac{dv_{pv}}{dt} = -i_{L,pv} + \frac{V_{eq} - v_{pv}}{R_{eq}} \quad (5.4)$$

Note that L_{pv} is the boost inductance; C_{pv} is the boost input capacitance; $R_{L,pv}$ is the series resistance of L_{pv} ; $i_{L,pv}$ is the L_{pv} current; v_{pv} is the PV terminal voltage; V_{eq} and R_{eq} are PV array voltage and resistance, respectively, seen from the PV terminal bus (SLONIM; SHAVIT, 1997).

First, PI_{pv1} represents voltage-loop and has as input the voltage difference between reference PV voltage v_{pv}^* and v_{pv} , generating inductor reference current i_{pv}^* as an output. Secondly, PI_{pv2} represents current-loop and has the difference between i_{pv}^* and i_{pv} as an input, and the d as an output. From equations (5.1) and (5.2), transfer functions are demonstrated and simplified (MIDDLEBROOK; CUK, 1976). Transfer function (TF) to control d in order to output i_{pv} is presented in Equation (5.5), while TF to control i_{pv} in order to output v_{pv} is described in Equation (5.6).

$$G_{id,pv} = \frac{V_{dc}(R_{eq}C_{pv}s + 1)}{R_{eq}L_{pv}C_{pv}s^2 + (R_{L,pv}R_{eq}C_{pv} + L_{pv})s + R_{L,pv} + R_{eq}} \quad (5.5)$$

$$G_{vi,pv} = \frac{-V_{dc}R_{eq}}{R_{eq}L_{pv}C_{pv}s^2 + (R_{L,pv}R_{eq}C_{pv} + L_{pv})s + R_{L,pv} + R_{eq}} \quad (5.6)$$

Equations (5.5) and (5.6) may be simplified to Equations (5.7) and (5.8), respectively:

$$G_{id-pv} = \frac{V_{dc}}{L_{pv}s + R_L} \quad (5.7)$$

$$G_{vi-pv} = -\frac{1}{C_{pv}s + \frac{1}{R_{eq}}} \quad (5.8)$$

Using (5.8) and (5.7) to apply the well-known pole placement technique presented by Ogata (2003) is possible to tune PI controllers and obtain its gains. Equations (5.9), (5.10) describe voltage controller proportional and integral gains, respectively, while Equations (5.11) and (5.12) describe current controller proportional and integral gains. All Equations consider boost switching frequency f_c , voltage controller and current controller cut-off frequencies: f_{cv} and f_{ci} , respectively.

$$K_{pv} = -2\pi f_{cv} C_{pv} \quad (5.9)$$

$$K_{iv} = -\frac{2\pi f_{cv}}{R_{eq-pv}} \quad (5.10)$$

$$K_{pi} = \frac{2\pi f_{ci} L}{V_{dc}} \quad (5.11)$$

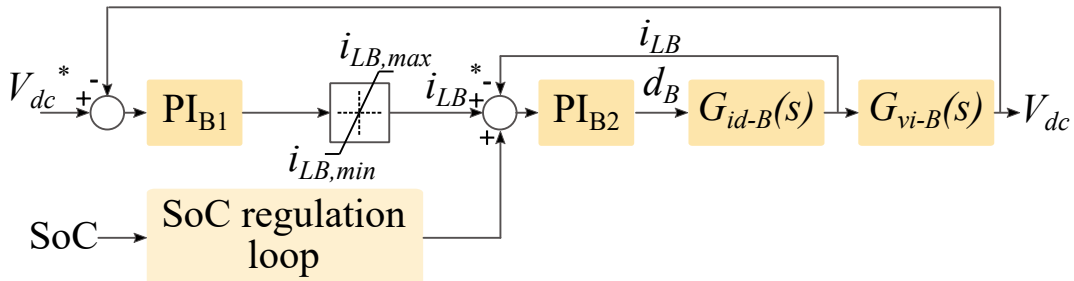
$$K_{ii} = \frac{2\pi R_L f_{ci}}{V_{dc}} \quad (5.12)$$

In order to tune PI controllers correctly, f_{ci} was considered ten times lower than f_c , while f_{cv} was considered a hundred times lower than f_c .

5.2 BESS BIDIRECTIONAL BUCK-BOOST CONTROL

According to the need, the BESS supports the microgrid unit by charging or discharging. When load power is larger than power delivered by PV units, the tendency is V_{dc} decrease. On the other hand, if load power is less than the power provides by PV units, V_{dc} tends to increase. In both cases, the BESS control system detects V_{dc} variation and acts in order to keep V_{dc} level constant. As the boost control, the bidirectional buck-boost control is composed of two main control loops: an outer voltage loop (PI_{B1}) and an inner current loop (PI_{B2}). Additionally, it comprises a minimum SoC regulation loop to change i_{LB} whenever it is required. The bidirectional converter control strategy is depicted in Figure 24.

Figure 24 – BESS bidirectional converter control strategy.



Source: Adapted from Mahmood, Michaelson and Jiang (2012).

When BESS needs to operate with a larger current larger than the discharging limit or lower than the charging limit, the saturation blocks limits i_{LB}^* to i_{LB-max} or i_{LB-min} , respectively.

5.2.1 Control Design

The bidirectional buck-boost dynamic equations are given by equations (5.13) and (5.14) for S_2 closed and S_3 open:

$$L_B \frac{di_{LB}}{dt} = v_B - R_{LB} i_{LB} \quad (5.13)$$

$$C_{dc,eq} \frac{dV_{dc}}{dt} = \frac{-V_{dc}}{R_o} \quad (5.14)$$

For S_2 open and S_3 closed, Equations (5.15) and (5.16) are obtained:

$$L_B \frac{di_{LB}}{dt} = -R_{LB} i_{LB} - V_{dc} + v_B \quad (5.15)$$

$$C_{dc,eq} \frac{dV_{dc}}{dt} = i_{LB} - \frac{V_{dc}}{R_o} \quad (5.16)$$

where L_B is BDC inductance and R_{LB} is L_B series resistance; v_B , i_{LB} are BESS terminal voltage and BDC inductor current, respectively, $C_{dc,eq}$ is the DC-link equivalent capacitance, and R_o is the virtual load resistance experimentally obtained. Here, R_c is considered around 53 Ω .

First, PI_{B1} regulates V_{dc} at V_{dc}^* to generate i_{LB}^* . Then, PI_{B2} regulates i_{LB} at i_{LB}^* . Thereby, Equations (5.13), (5.14), (5.15) and (5.16) are used to obtain TFs presented in Equations (5.17) and (5.18):

$$G_{id-B} = \frac{V_{dc} C_{dc,eq} R_o s + V_{dc} + R_o I_{LB} (1 - d_B)}{R_o L_B C_{dc,eq} s^2 + (L_B + R_o C_{dc,eq} R_B) s + R_{LB} + R_o (1 - d_B)^2} \quad (5.17)$$

$$G_{vi-B} = \frac{-R_o L_B I_{LB} s - R_o R_{LB} I_{LB} + R_o (1 - d_B) V_{dc}}{V_{dc} C_{dc,eq} R_o s + V_{dc} + R_o I_{LB} (1 - d_B)} \quad (5.18)$$

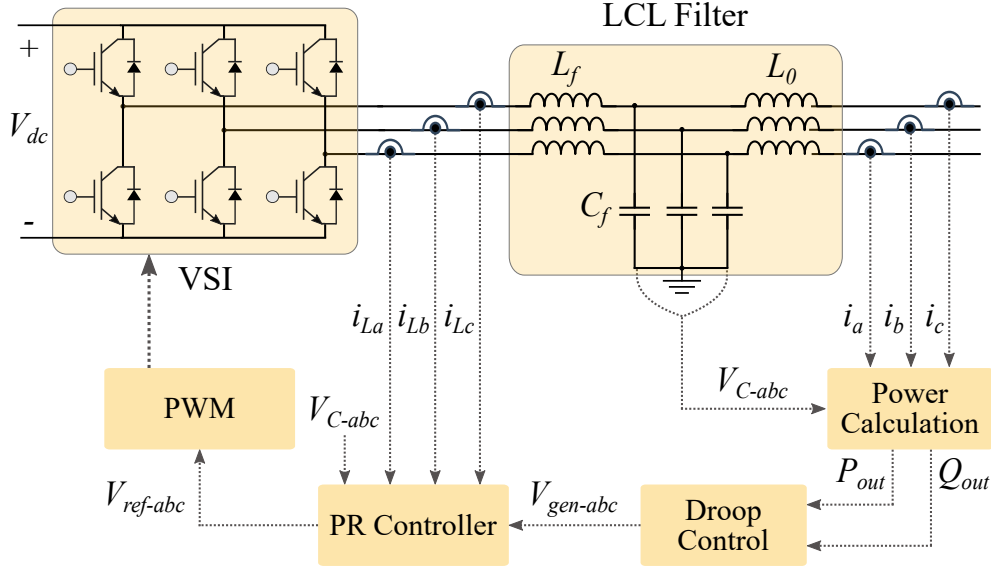
5.3 VSI GRID-FORMING DROOP CONTROL

This way, this subsection is dedicated to detailing the VSI grid-forming control based on droop control.

It is important to notice that in islanded mode, the microgrid studied in this work does not have frequency reference since there is no synchronous generator machine

connected. Thereby, a grid-forming control strategy based on droop control provides voltage and frequency reference to the microgrid unit. Due to the lack of inertia, this technique mimics the behavior of a synchronous machine by frequency and voltage according to active and reactive power, respectively. The block diagram of this strategy is presented in Figure 27.

Figure 25 – VSI Grid-forming control diagram.



Source: Adapted from Karimi, Oraee and Guerrero (2017).

5.3.1 Power Calculation Theory

Firstly, three-phase load output power calculation is performed according to instantaneous power theory using Equations 5.19 and 5.20 to compute instantaneous active and reactive power, respectively (AKAGI; KANAZAWA; NABAE, 1984):

$$P_{out}(t) = V_{c-a}I_{fa} + V_{c-b}I_{fb} + V_{c-c}I_{fc} \quad (5.19)$$

$$Q_{out}(t) = -\frac{1}{\sqrt{3}}(V_{bc}I_{fa} + V_{ca}I_{fb} + V_{ab}I_{fc}) \quad (5.20)$$

where V_{c-a} , V_{c-b} and V_{c-c} are phase voltages, while V_{bc} , V_{ca} and V_{ab} are line voltages.

After power calculation, droop control is performed to generate voltage amplitude and frequency references. Together they compose the reference voltage waveform. Further, secondary droop control is employed to avoid high frequency and voltage deviations. PR controllers track this reference waveform through inner current and voltage loops (KARIMI; ORAEE; GUERRERO, 2017). Droop control and PR controllers are detailed in the following subsections.

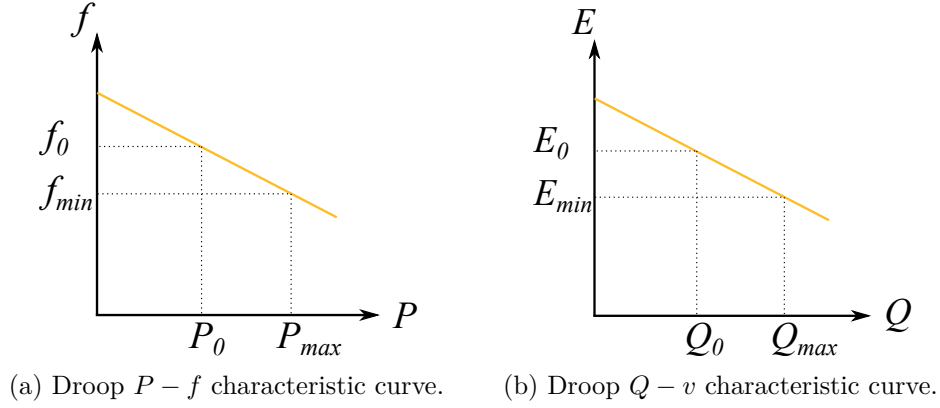


Figure 26 – Droop control characteristic curves.

5.3.2 Droop Control

Literature addresses many droop controllers based on conventional grid control. The presence of rotating generators provides grid frequency reference due to their rotating inertia. The difference between mechanical input power and electrical output power change generator rotational speed (VANDOORN *et al.*, 2012). However, PV generators do not have rotational inertia, so they need a technique to simulate this behavior.

Traditional droop control is based on the power flow characteristics of inductive lines, so this strategy does not require rotating inertia. Once microgrid output impedance is mainly inductive, this technique links microgrid active power with the phase angle used to obtain grid frequency, and reactive power with voltage. Then, the fundamental equations of traditional droop control are:

$$f_{droop} = f_0 + m \cdot (P_0 - P) \quad (5.21)$$

$$E_{droop} = E_0 + n \cdot (Q_0 - Q) \quad (5.22)$$

where, m and n are frequency and voltage droop coefficients, respectively; f_{droop} and f_0 are output and nominal frequency, respectively; E_{droop} and E_0 are output and nominal voltage amplitude, respectively; P_0 and Q_0 are reference active and reactive powers, respectively; P and Q are load active and reactive powers, respectively.

From Equations (5.21) and (5.22), droop characteristic curves are presented in Figures 26a and 26b, respectively. P_0 is here represented by the PV power while P is represented by the load power. Since this work considers resistive load, Q_0 is considered zero, whereas Q is represented by load reactive power.

5.3.3 Secondary Droop Control

It is crucial to consider droop control drawbacks to limit the reference AC voltage to safe regions of amplitude and frequency. The main limitation of droop control is that

little power variations may represent large frequency and voltage deviations. For this reason, this work employs a secondary droop control to regulate frequency and voltage at safe values according to the work of Nutkani *et al.* (2015). The frequency and voltage generated by droop control are dynamically recovered through the restoration off-sets calculated as shown in Equations (5.23) and (5.24):

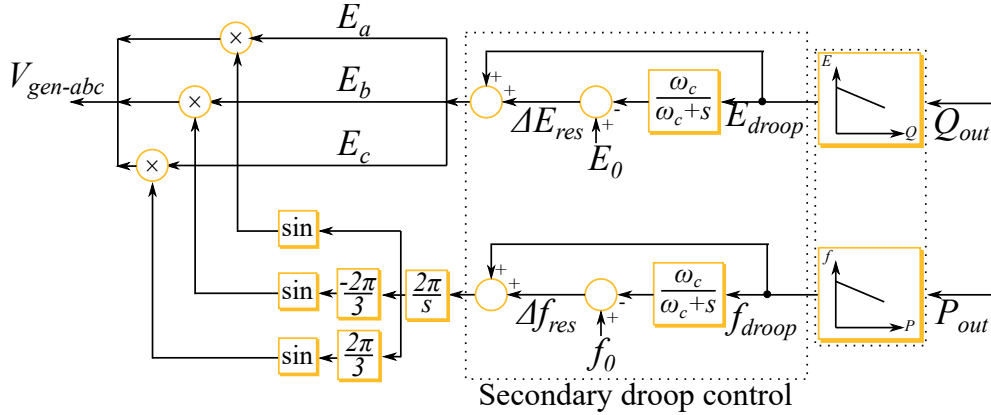
$$\Delta f_{res} = f_0 - f_{droop} \frac{\omega_c}{s + \omega_c} \quad (5.23)$$

$$\Delta E_{res} = E_0 - E_{droop} \frac{\omega_c}{s + \omega_c} \quad (5.24)$$

where Δf and ΔV are the frequency and voltage restoration off-sets, respectively and ω_c is the cut-off frequency to filter transients. Note that in equations (5.23) and (5.24), f and V are the droop output frequency and voltage amplitude, respectively.

To facilitate the understanding, the complete droop control diagram is presented in Figure 27, including traditional and secondary droop control and the wave generator.

Figure 27 – Droop control diagram.



Source: Adapted from Karimi, Oraee and Guerrero (2017).

5.3.4 PR Control

Following Figure 27, inner control loops are performed to track the reference voltage waveform generated by droop control. The outstanding performance of PR controllers in tracking AC variables has made this strategy widely used (BIRICIK; KOMURCUGIL, 2018). Basically, to eliminate steady-state error at a given frequency, the PR strategy introduces an infinite gain at that resonant frequency (TEODORESCU *et al.*, 2006). The basic transfer function of the PR controller used in this work is given by Equation (5.25):

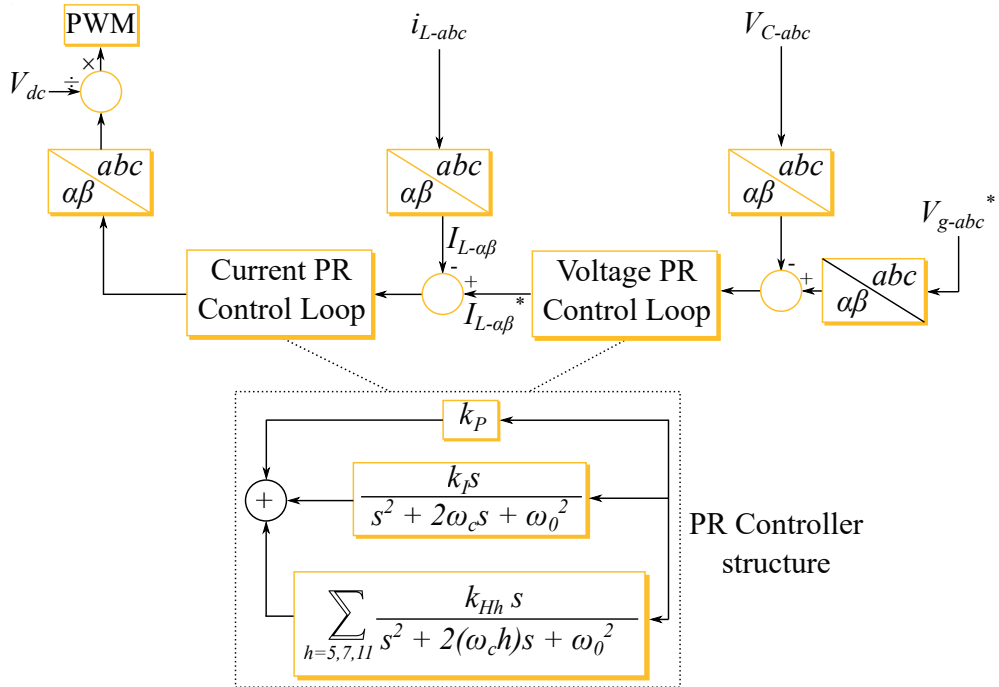
$$G_{PR}(s) = k_P + \frac{k_R s}{s^2 + 2\omega_c s + \omega_0^2} \quad (5.25)$$

where k_P is the proportional gain, k_R is the resonant gain, ω_c is the cut-off frequency, and ω_0 is the resonant frequency.

The PR controller used in this work considers not only single-frequency compensation, but uses cascade connected resonant controllers tuned at 5th, 7th and 11th harmonics to be compensated (VASQUEZ *et al.*, 2013)(TEODORESCU *et al.*, 2006). Then, Equation (5.26) is added to (5.25) to complete a loop control:

$$G_h = \sum_{h=5,7,11} \frac{k_{Hh}s}{s^2 + 2(\omega_ch)s + \omega_0^2} \quad (5.26)$$

Figure 28 – PR control loops strategy blocks.



Source: Adapted from Vasquez *et al.* (2013).

The complete control strategy is composed of current and voltage loops as depicted in Figure 28. It is based on stationary reference frame obtained by well-known Clarke transformation, as described in Equation (5.27), to convert abc voltages and currents into $\alpha\beta$.

$$\begin{bmatrix} V_{g\alpha} \\ V_{g\beta} \\ V_{g0} \end{bmatrix} = \begin{bmatrix} \frac{2}{3} & -\frac{1}{3} & -\frac{1}{3} \\ 0 & \frac{1}{\sqrt{3}} & -\frac{1}{\sqrt{3}} \\ \frac{1}{3} & \frac{1}{3} & \frac{1}{3} \end{bmatrix} \begin{bmatrix} V_{ga} \\ V_{gb} \\ V_{gc} \end{bmatrix} \quad (5.27)$$

5.3.5 Frequency Estimation: Phase Locked Loop

Phase Locked Loop (PLL) is a technique used to obtain phase information of grid voltage. It is here used to track the frequency behavior by using the diagram block

Table 3 – Control Parameters.

Parameter	Symbol	Value
p - f Droop Coefficient	m	0.005
q - v Droop Coefficient	n	0.1
PR Controller	Voltage Loop(K_{pv}, K_{rv}) Current Loop(K_{pi}, K_{ri})	0.764, 159 120, 1000
Bidirectional Controllers	PI _{B1} (K_{pB1}, K_{iB1}) PI _{B2} (K_{pB2}, K_{iB2}) PI _{B3} (K_{pB3}, K_{iB3})	21.13, 2822.63 0.042, 70 21.13 · 10 ⁴ , 5.65 · 10 ⁶
Boost Controllers	PI ₁ (K_{p1}, K_{i1}) PI ₂ (K_{p2}, K_{i2}) PI _{pv1} (K_{ppv1}, K_{ipv1}) PI _{pv2} (K_{ppv2}, K_{ipv2})	12.57 · 10 ⁵ , 106.82 · 10 ⁵ 0.1257, 53.41 -0.1257, -53.41 0.185, 3.14
BCAW Gains	PI ₁ (K_{b1}) PI ₂ (K_{b2}) PI _{B1} (K_{bB1}) PI _{B3} (K_{bB3})	106.82 · 10 ⁵ 53.41 2822.63 5.65 · 10 ⁶

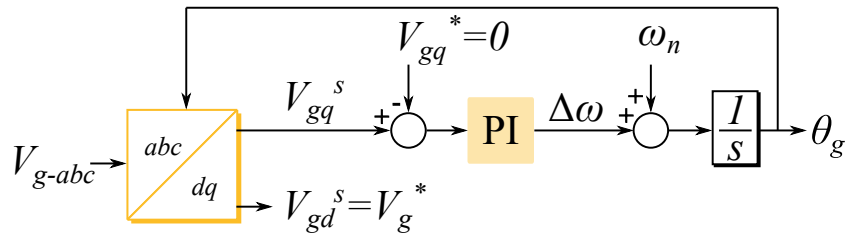
presented in Figure 29 (DU *et al.*, 2019).

The PLL method used in this work consists of a dq synchronous reference frame (SRF) through Park transformation described by Equation (5.28) to translate grid voltage abc into dq frame (HADJIDEMETRIOU; KYRIAKIDES; BLAABJERG, 2012):

$$\begin{bmatrix} V_{gd} \\ V_{gq} \end{bmatrix}^s = \frac{2}{3} \begin{bmatrix} \cos(\theta_g) & \cos(\theta_g - 120^\circ) & \cos(\theta_g + 120^\circ) \\ -\sin(\theta_g) & -\sin(\theta_g - 120^\circ) & -\sin(\theta_g + 120^\circ) \end{bmatrix} \begin{bmatrix} V_{ga} \\ V_{gb} \\ V_{gc} \end{bmatrix} \quad (5.28)$$

where V_{ga} , V_{gb} and V_{gc} are grid voltage amplitude absolute value for phases a , b and c , respectively, θ_g is grid voltage phase angle, V_{gd} and V_{gq} are dq grid voltage in the synchronous referential.

Figure 29 – PLL strategy block diagram.



Source: Adapted from Silva Júnior (2021).

From Equation (5.28), Equation (5.29) is obtained considering the same amplitude absolute value (V_g) for all three phases:

$$\begin{bmatrix} V_{gd} \\ V_{gq} \end{bmatrix}^s = \begin{bmatrix} V_g \cos(\theta_g - \bar{\theta}_g) \\ V_g \sin(\theta_g - \bar{\theta}_g) \end{bmatrix} \quad (5.29)$$

Thereby, the strategy presented in Figure 29 makes synchronous q-axis reference be in phase with voltage grid vector (V_g), so $\theta_g = \bar{\theta}_g$ (SILVA JÚNIOR, 2021). A PI controller tracks q-axis grid voltage V_{gq} to a zero value, so angular speed ω and θ_g are obtained (HADJIDEMETRIOU; KYRIAKIDES; BLAABJERG, 2012). The first is obtained through the sum of nominal angular frequency (ω_n) and angular frequency variation generated by the PI controller. The last one is computed by the integration of ω .

The control parameters are listed in Table 3.

6 Simulation Results

This chapter is dedicated to describing the simulation results. The microgrid and the control systems presented in the previous chapter were implemented and simulated in Matlab/Simulink environment.

6.1 Simulation Results

The simulations were conducted through five scenarios to show the unit transit among all operation states. These scenarios are:

1. Scenario 1: comprehends a transition from state 1 to state 3;
2. Scenario 2: comprehends a transition from state 1 to state 2;
3. Scenario 3: comprehends a transition from state 2 to state 3;
4. Scenario 4: comprehends a transition from state 1 to state 4;
5. Scenario 5: comprehends a transition from state 1 to state 5;

Each scenario was simulated with and without the employment of AWD techniques in the specific PI controller responsible for the state transition. The same simulation was performed using CAW and BCAW techniques to compare their performance. Further, in scenario 4 the proposed $UV_{dc}LS$ was compared to the traditional under-frequency load-shedding ($UFLS$). The following subsections describe the simulation details for each scenario.

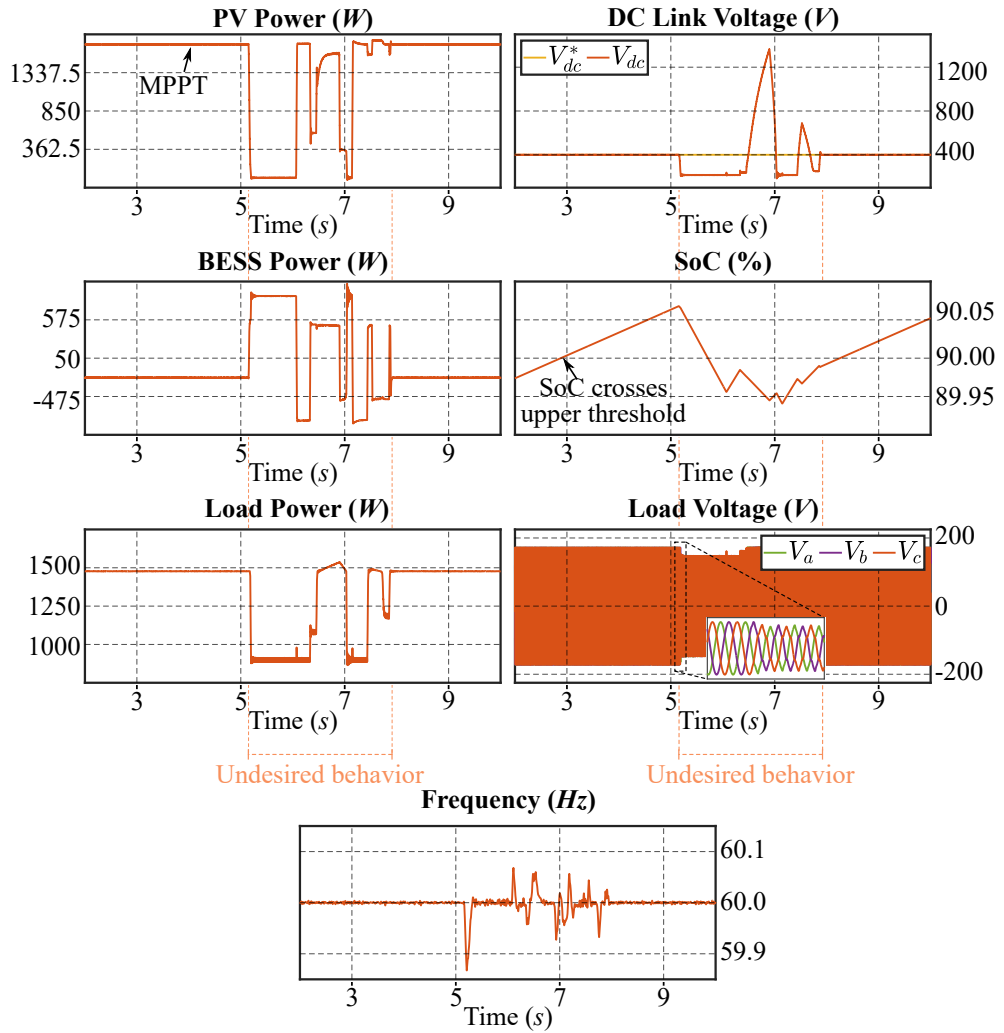
6.1.1 Scenario 1: Transition from State 1 to State 3

A situation where the BESS absorbs the PV extra power until it is totally charged was simulated, and it is presented here. It means that the SoC reaches SoC_{max} . To protect the BESS, the PI_1 action makes the PV unit reduce the power until the load is met and the BESS power is settled at zero. The simulation considers nominal operating conditions for the PV unit ($1000W/m^2$ and $25^\circ C$). The expected behavior is described as follows.

In the beginning, the PV injects a maximum of 1700 W considering the boost power losses and the load demand is over 1477 W. As the PV power is larger than the total output power, the BESS absorbs about 223W to maintain the stability. At approximately 2.9 s the SoC crosses the upper threshold (SoC_{max}). The input error of PI_1 turns negative,

dragging the PV unit away from MPP. The PV unit then cuts power until the BESS power is settled in zero, and consequently, the SoC is regulated to SoC_{\max} . In this situation the BESS may not absorb the power, then the PV power is reduced to over 1477 W to match the load power. The unit then works in state 3. The unit switches to state 3 due to the action of the PI_1 controller. However, the action of the saturation block limits the output signal to negative values to ensure it changes the PV unit set-point only when the SoC has reached SoC_{\max} . If no anti-windup is employed, the integration will take the controller output far away from safe operation values whereas $\text{SoC} < \text{SoC}_{\max}$. It will not just delay the controller action when it is required, but provoke undesired behaviors. The next paragraphs detail the comparison.

Figure 30 – Scenario 1 results without AWD in PI_1 .

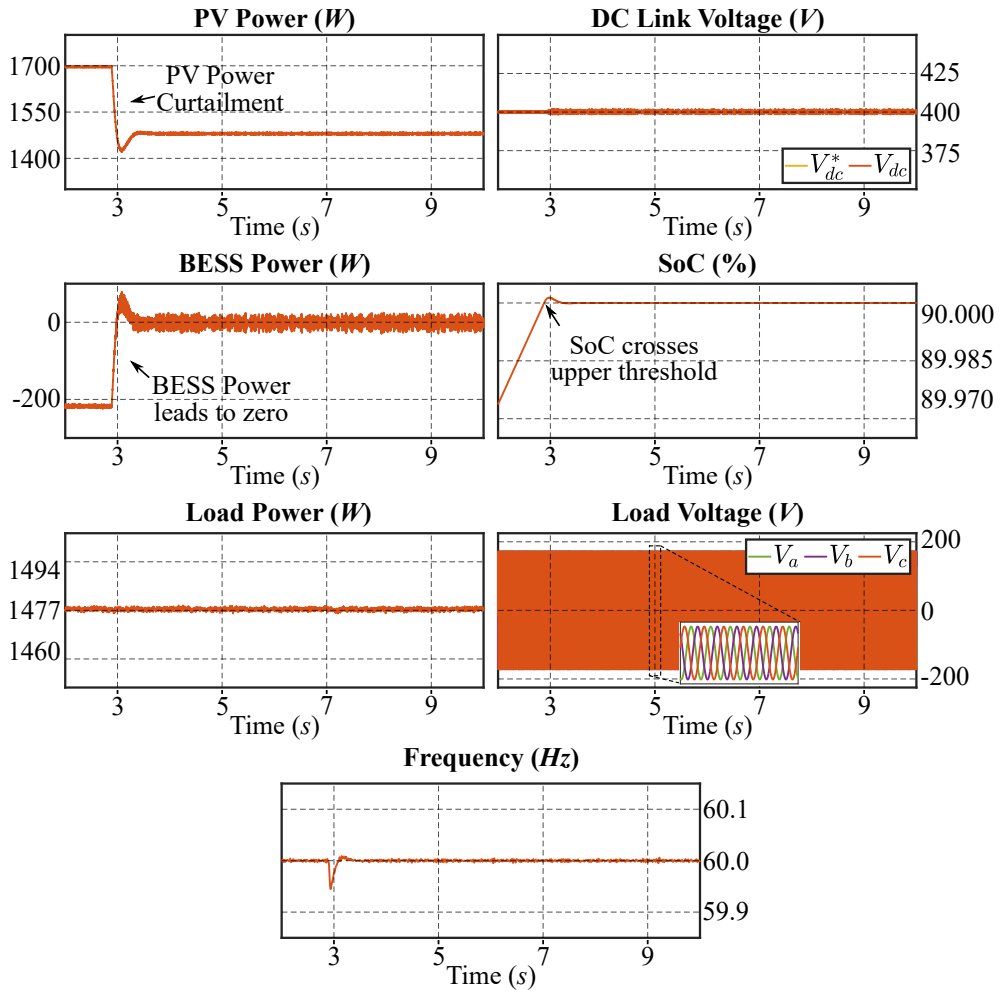


Source: Made by the author.

First, the simulation was performed with no anti-windup technique in any controller (PI_1 , PI_2 nor PI_{B1}). The results are presented in Figure 30. When the SoC reaches SoC_{\max} , no action is taken at first and the SoC keeps increasing. It may be explained by observing the PI_1 output signal in Figure 32 without anti-windup. Note that no limitation in the integrator has led the output signal to huge values. The strategy then waits for the output

signal to return from a high positive to a negative value to change the PV power set-point. At approximately 6 s, the signal crosses zero value, and the negative value affects the PV power. However, the non-limited signal drives the PV unit to a deep power drop until it reaches 0W, leading to a series of undesired and harmful behaviors. As there is no more PV power, the BDC control leads the BESS to a huge discharge value out of its safe control margin. Even with the current controller limiter, the BESS operates with approximately from 6 s to 7 s power above its limits. It is also observed a drop in V_{dc} , causing an AC voltage drop, and consequently a drop in the power delivered to the load. A huge undesired transient is noticed until PI_1 output is stable.

Figure 31 – Scenario 1 results with CAW in PI_1 .

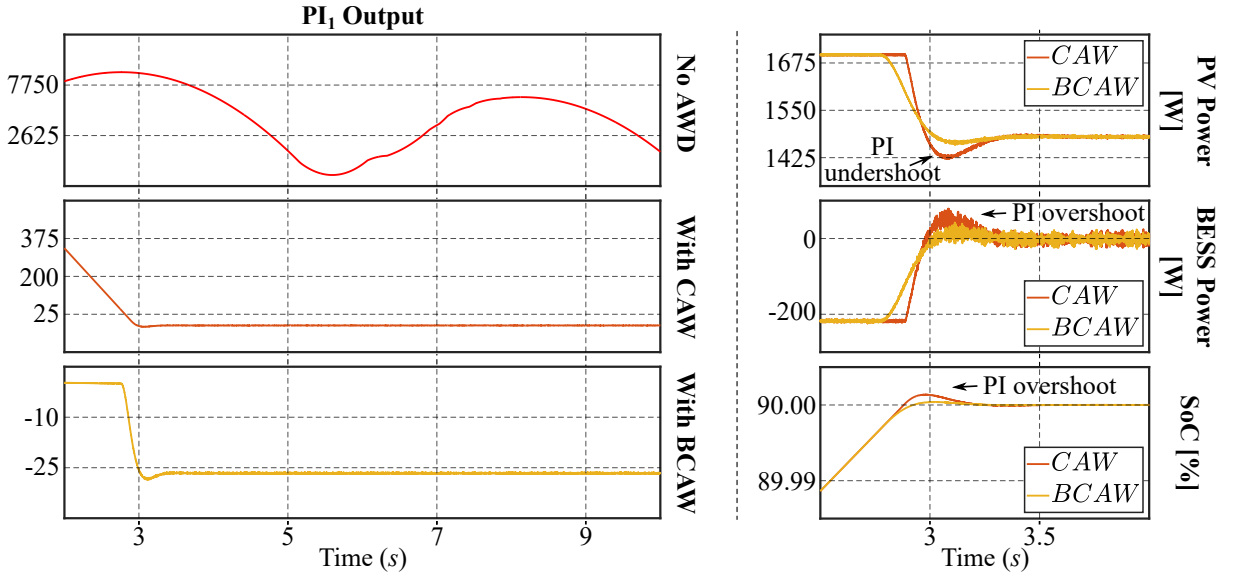


Source: Made by the author.

This undesired behavior during the transition from state 1 to state 3 may be avoided by simply employing an integration anti-windup method. The same simulation was performed using the previously detailed CAW technique in PI_1 , and the results are depicted in Figure 31. The unit behaves exactly as expected, following the behavior described in the second paragraph of this subsection. In this case, the unit operation states are well-defined. It operates in state 1 until 2.9 s, and in state 3 after it.

The same simulation was performed using the BCAW technique in PI_1 . Both strategies showed good performance in terms of avoiding undesired transients and ensuring smooth state transition. However, BCAW showed an even smoother transition by providing a faster response and reducing integration overshoots and undershoots. As the BCAW technique relies on dynamic gain to reset the integrator input, it works in this situation as a predictive factor. To illustrate it, the PI_1 output signal is plotted in Figure 32 for both strategies during the complete simulation. In addition, this comparison may be attested in the same figure where zoom in P_{BESS} , in the PV power, and in the SoC are depicted in the moment of the transition. It is clear to see the presence of the undershoot and overshoot with the CAW technique, and this phenomenon is explained as follows.

Figure 32 – Comparison between AWD strategies in PV power, BESS power, SoC, and PI_1 .



Source: Made by the author.

The CAW strategy resets the integrator input to zero instantaneously when the integration is no longer needed. The PI_1 output is then only driven by the proportional action as the SoC gets closer to SoC_{max} . It waits until SoC crosses the limit, the negative error turns the saturation block input equal to the output to switch instantaneously the integrator input to the controller input error. It takes some milliseconds until the SoC is settled at SoC_{max} , P_{BESS} at 0W, and the PV power at 1477 W, causing the characteristic PI controller overshoot or undershoot.

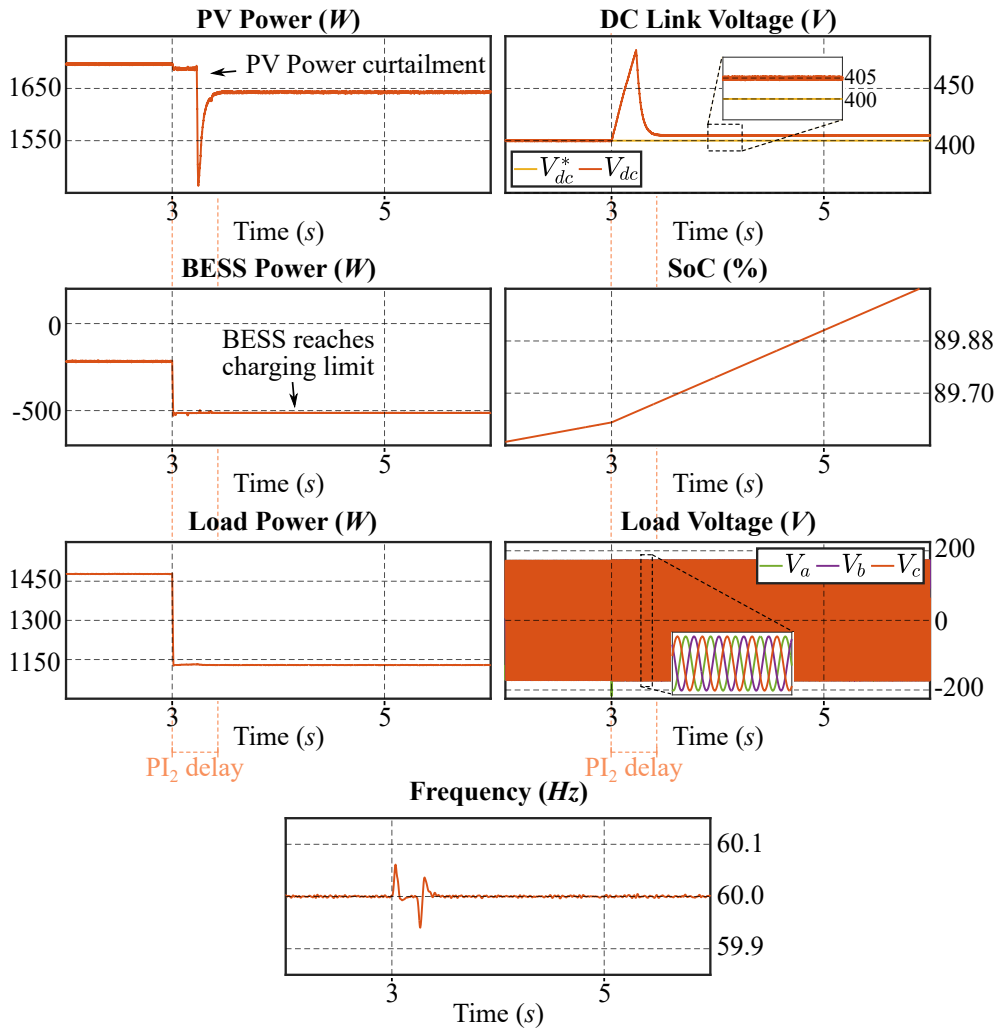
On the other hand, as the BCAW method uses a dynamic methodology based on a gain rate, it presents a smoother transition. While SoC has not reached SoC_{max} , the positive error produces a positive input signal in the saturation block. As the saturation block output is zero for positive inputs, the difference between the output and the input produces a dynamic negative value to be decreased from the integrator input at the BCAW gain rate K_{b1} . As the SoC gets closer to SoC_{max} , this difference is reduced, and the reset signal decreases until zero. This dynamic process does not reset the integration

action instantaneously, offering a faster and smoother response, and consequently reducing overshoots (ÅSTRÖM; HÄGGLUND, 2006).

6.1.2 Scenario 2: Transition from State 1 to State 2

In this scenario, the simulations were performed to present a transition from state 1 to state 2. It means that the unbalance between PV power and load demand is enough to make BESS reach the maximum charging power limit. The control system then limits i_{LB} to $i_{LB,min}$, so the PV must reduce the power to control V_{dc} . The unit is expected to behave as described in the next paragraph.

Figure 33 – Scenario 2 results without AWD in PI₂.

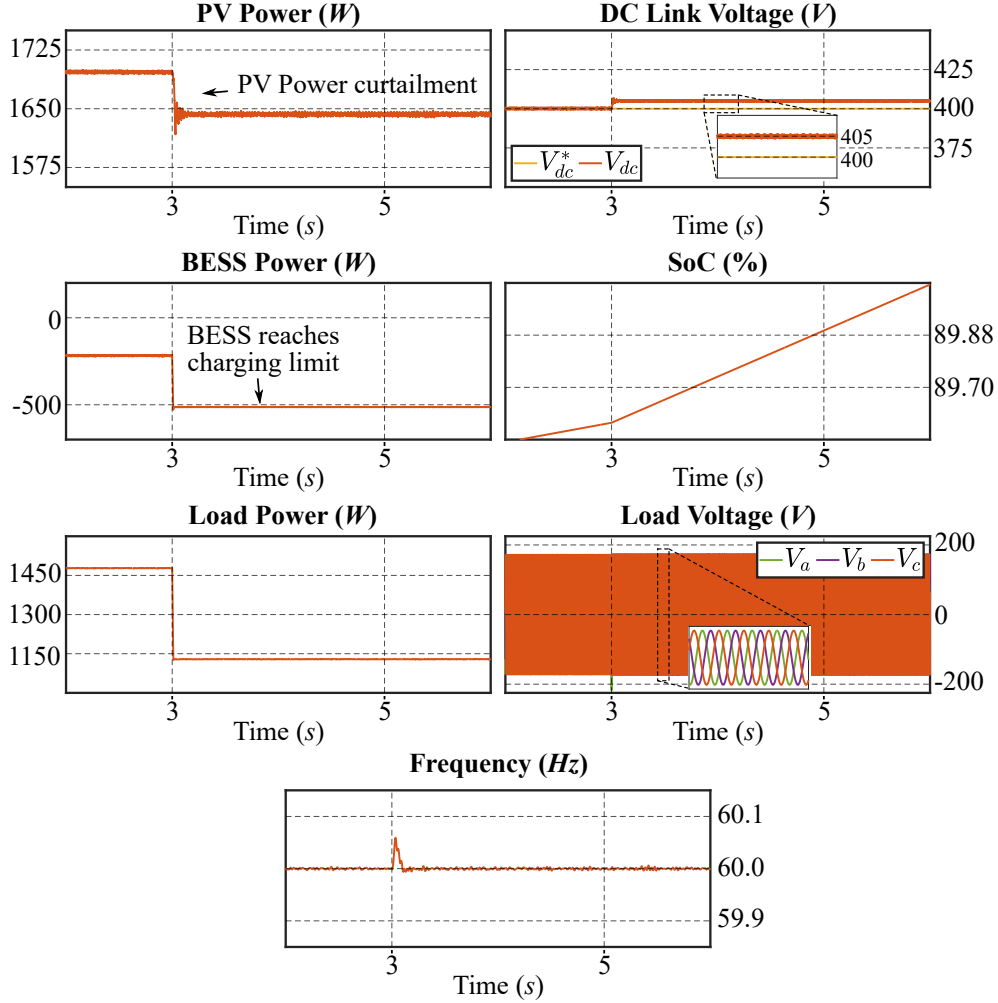


Source: Made by the author.

The simulation starts with a load power of over 1480 W. The PV unit injects 1700 W MPP power, so the BESS absorbs 220 W, making the unit work in state 1. At the instant 3 s, the load power abruptly decreases to about 1130 W. The BESS then reaches its maximum charging power limit of 500 W. However, it would be required to absorb 570 W of power from the PV. The surplus 70 W may not be absorbed, making V_{dc} increase. This

increase is detected by PI_2 , and v_{pv}^* is pushed away from MPP to control V_{dc} at $V_{dc} + \Delta V$. The PV unit then reduces the power to over 1630 W to keep the balance, making the unit switch to state 2. Here ΔV is considered 5 V, so V_{dc} is regulated to 405 V.

Figure 34 – Scenario 2 results with CAW in PI_2 .



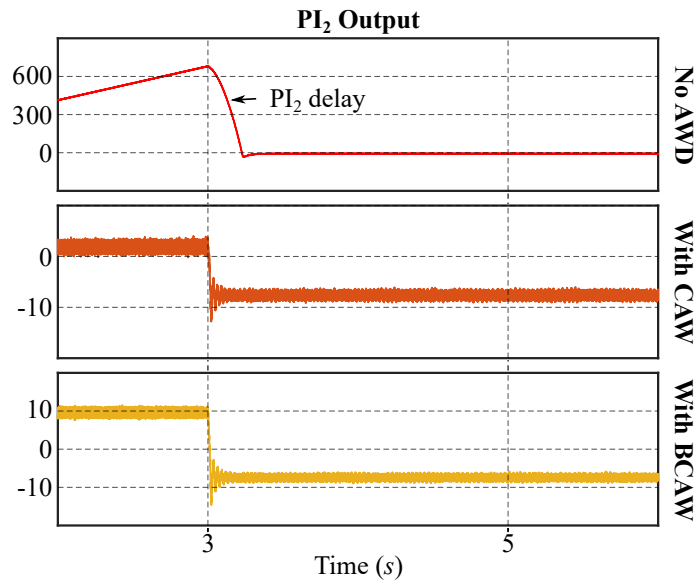
Source: Made by the author.

The action of PI_2 makes the unit change from state 1 to state 2 whenever V_{dc} increases above $V_{dc}^* + \Delta V$. During state 1, the BDC controls V_{dc} to V_{dc}^* , so the input error in PI_2 is not null, causing an integration windup in this controller. As a consequence, it causes a delay in the transition from state 1 to 2, and an undesired increase in V_{dc} . To illustrate this, a simulation was performed without the employment of any AWD strategy in PI_2 , and the results are presented in Figure 33. This controller should decrease the PV right after the load drop. However, the non-limited integrator has increased the controller output signal away from a safe range into high positive values. When V_{dc} crosses $V_{dc}^* + \Delta V$, the system has to wait for the control signal to become negative to perform PV power curtailment. In this simulation, the controller took approximately a 730 ms delay (PI_2 delay) to perform. This time might be even longer depending on how long the integrator has integrated a non-null error. The PI_2 output signal with no AWD method in Figure 35

confirms the misbehavior.

The same simulation was performed employing twice, employing CAW and BCAW strategy in PI_2 , one at a time. The results for CAW are depicted in Figure 34. The performance matches exactly the expected behavior described at the beginning of this subsection. In the transition from state 1 to state 2, the anti-windup strategy reduced the PI_2 delay from 730 ms to almost none. Both AWD strategies performed accordingly and showed the same results. Further, Figure 35 also depicts PI_2 output signals to confirm the similarity.

Figure 35 – Comparison between AWD strategies in PI_2 .



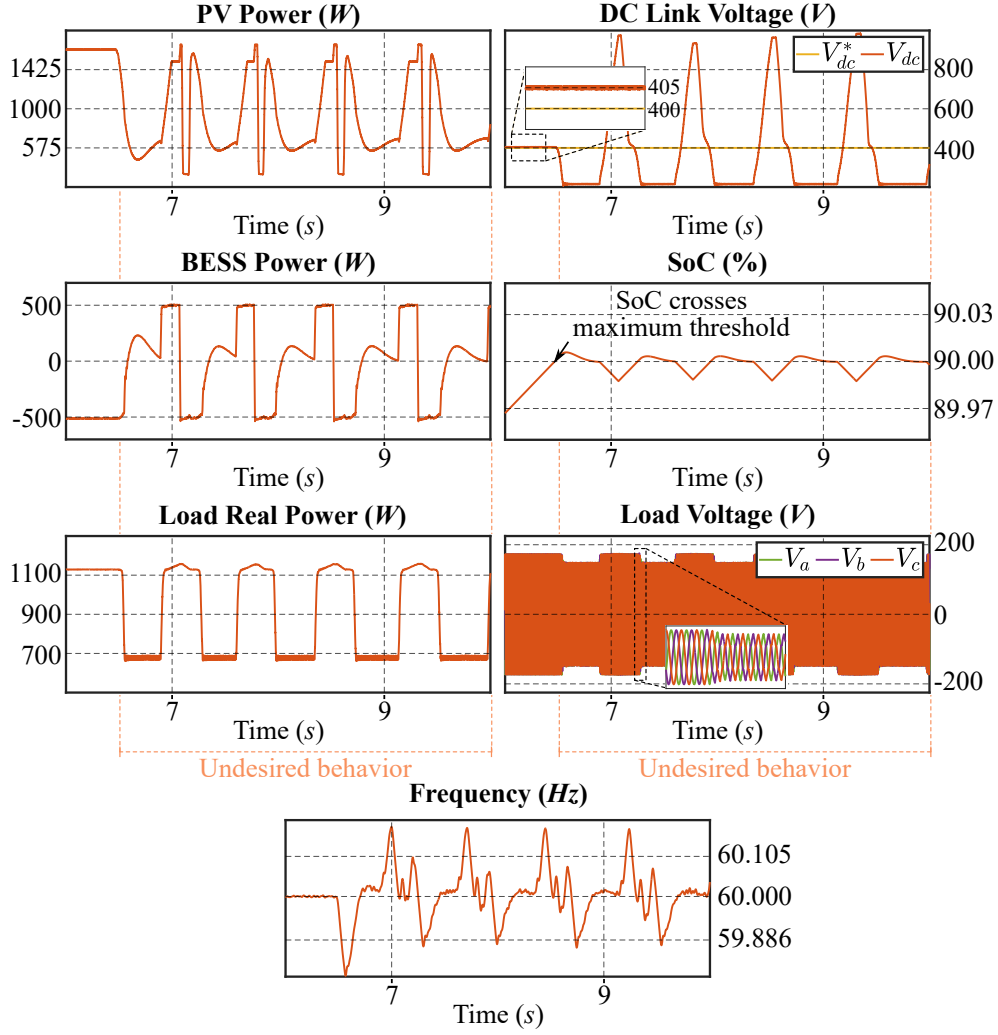
Source: Made by the author.

6.1.3 Scenario 3: Transition from State 2 to State 3

This subsection describes the transition from state 2 to state 3 continuing the same simulation performed in scenario 2. The simulation lasted enough time to make the SoC cross SoC_{max} . The transition to state 3 is expected to happen as described in the next paragraph.

At the moment the unit switched to state 2, the load power was reduced to 1130 W, the PV power was reduced to 1630 W while the BESS absorbs 500 W. When the SoC crosses SoC_{max} at approximately 6.5 s, the action of PI_1 pushes the PV unit even more away from MPP until BESS power is settled in 0 W, the SoC is regulated to SoC_{max} , and the PV unit reaches 1130 W to match the system load demand. Finally, the unit switches to state 3.

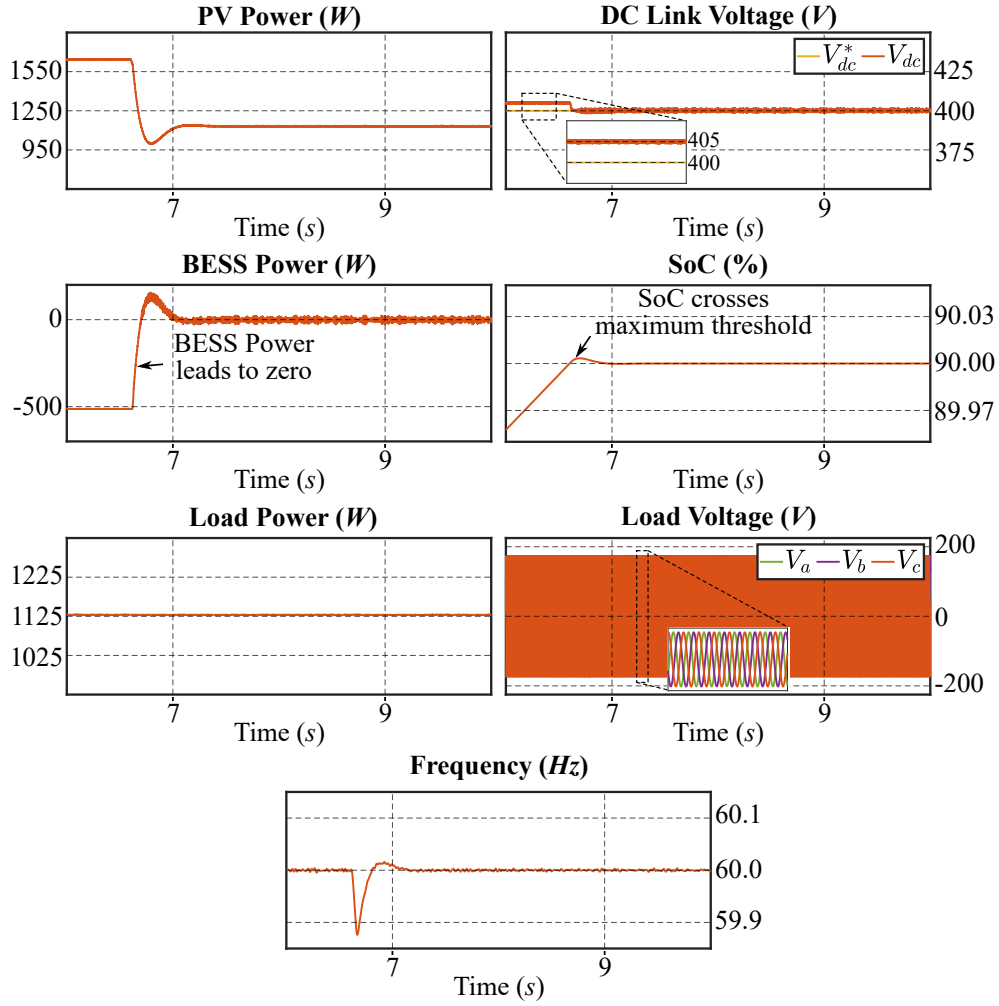
As presented in scenario 1, an AWD technique is required to avoid undesired transients when the SoC needs to be regulated at SoC_{max} . However, in the transition from state 2 to state 3, the employment of AWD in PI_1 is not enough to avoid misbehavior.

Figure 36 – Scenario 3 results without AWD in PI_{B1} , and with CAW in PI_1 .

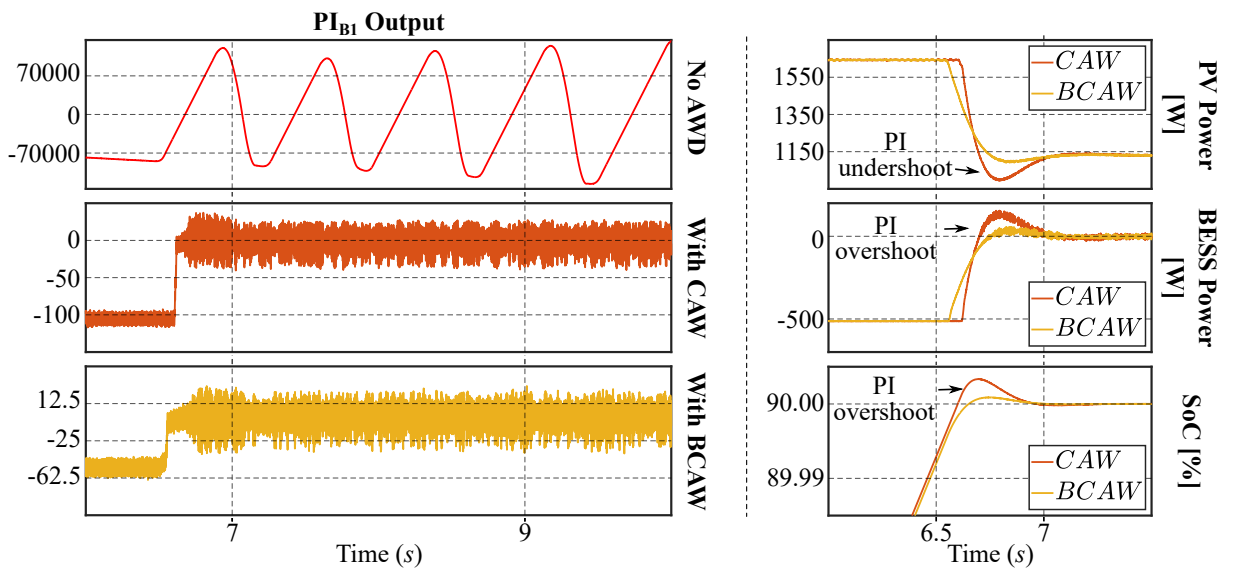
Source: Made by the author.

During state 2, V_{dc} is regulated to $V_{dc}^* + \Delta V$, but the input reference of PI_{B1} is V_{dc}^* . Then, the undesired behaviors are now provoked by the windup effect in PI_{B1} . Therefore, a simulation was performed with the employment of CAW technique in PI_1 , but with no AWD in PI_{B1} . When the PV power is reduced again, the BESS power must lead to zero. However, the output signal of PI_{B1} has decreased too much, so the system must wait until the control signal returns. But the unlimited integration action caused high variations in the control signal resulting in the undesired behavior presented in Figure 36, and confirmed by the PI_{B1} output signal plotted in Figure 38 with no AWD in PI_{B1} . The undesired behavior causes not just harmful variations in V_{dc} , but as a consequence, AC voltage distortions and load power noise are observed.

Again, the solution lies simply in employing an AWD technique in PI_{B1} . Now, the same simulation was performed, but this time employing AWD technique in both PI_{B1} and PI_1 . Both are necessary to avoid misbehavior in this scenario. The unit behaved exactly as described in the second paragraph of this subsection. The results using CAW in both

Figure 37 – Scenario 3 results with CAW in PI_{B1} and PI_1 .

Source: Made by the author.

Figure 38 – Comparison between AWD strategies in PV power, BESS power, SoC, and PI_{B1} .

Source: Made by the author.

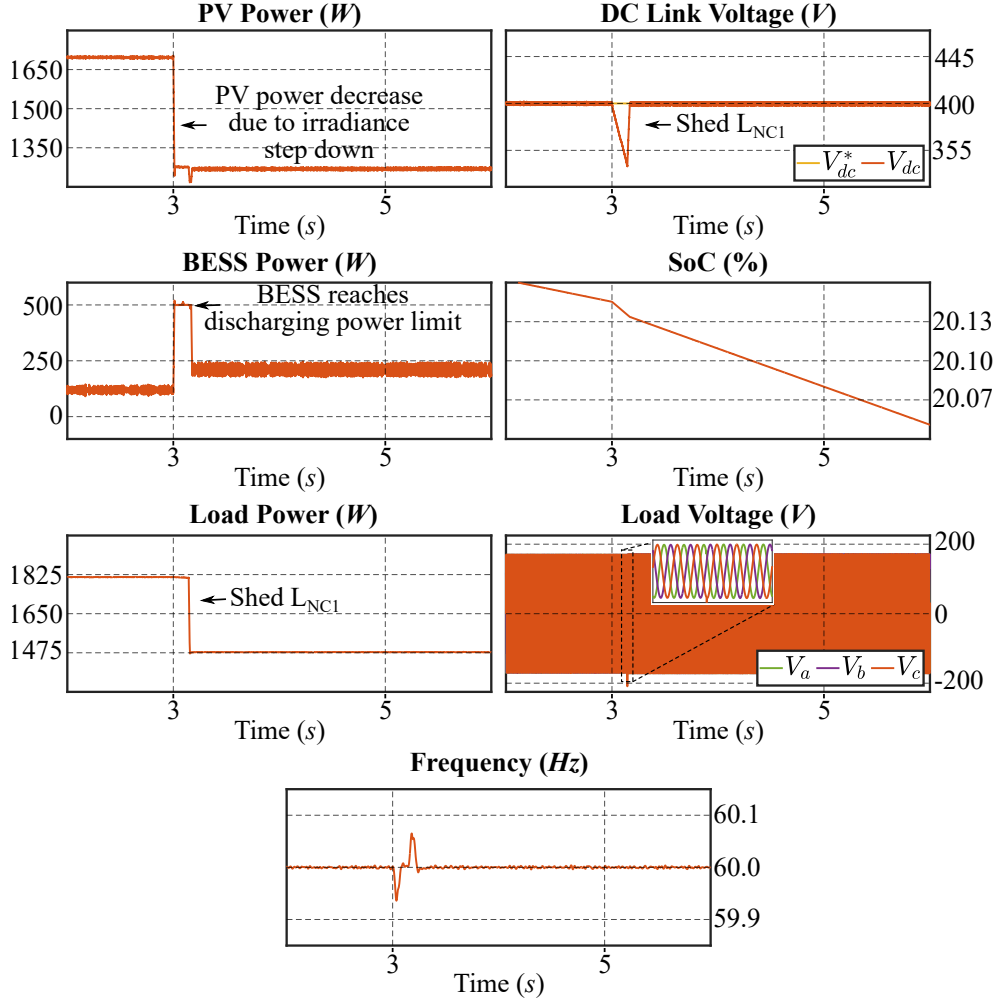
controllers are presented in Figure 37. Extremely similar results were witnessed using both BCAW and CAW. However, BCAW again showed a faster response by avoiding undershoots and overshoots. To illustrate this, Figure 38 depicts a zoom in the PV power, the BESS power, and SoC at the moment of the transition. In the same Figure, note that the PI_{B1} output signal is limited when an AWD method is employed.

6.1.4 Scenario 4: Transition from State 1 to State 4

State 4 comprehends situations when the BESS works within a safe SoC range but reaches the maximum discharging power. As the load power is still greater than the PV generation, the power lack causes a decrease in V_{dc} . Then, the system must shed loads to keep the balance. Here, the proposed $UV_{dc}LS$ method performance is presented. First, a simulation of the best situation is performed. The best situation is to keep the frequency secondary droop control turned on to regulate the frequency at the nominal value f_0 , while the signal for unbalance detection and load shedding is obtained from variations in V_{dc} . First, this scenario considers a non-critical load L_{NC1} , here considered to be over 350 W. Figure 39 illustrates the results of this first simulation, and it is described in the next paragraph.

In the beginning, a critical load of 1475 W is connected with L_{NC1} , resulting in a total load power of 1825 W. Again, the PV power operates by injecting over 1700 W in MPPT mode, considering the normal irradiance condition of 1000 W/m². As the PV power is lower than the total system demand, the BESS injects approximately 125 W. At the instant 3 s, a step down is applied in the irradiance, decreasing it from 1000 W/m² to 750 W/m² to simulate partial shading in the PV array. It changes the MPP, so the PV unit MPPT value decreases to 1250 W. At this moment, the BESS delivers the maximum discharging power limit $P_{BESS,max}$ of 500 W. The total available power is 1750 W, but the total load requires 1825 W. Then, the unit works in state 4. As the BESS power plus the available PV array power are not enough to meet the total load, the BESS can't control the link voltage, causing a drop in V_{dc} . The system has no other option but to shed a non-critical load attempting to restore the power balance. The $UV_{dc}LS$ algorithm detects the power unbalance when V_{dc} drops below $V_{dc}^* - \Delta V$, and after 100 ms L_{NC1} is shed. Here, ΔV is also considered 5 V. Now, only the critical load of 1475 W is connected, and the BESS regulates V_{dc} by injecting 225 W. Once the system power balance is restored, the microgrid's DG unit returns to state 1 working in normal operation.

To conclude, in this simulation, the proposed $UV_{dc}LS$ method showed to work properly in maintaining the power balance. The frequency presented no considerable variation due to the action of the droop secondary control, and the AC voltage waveform is preserved.

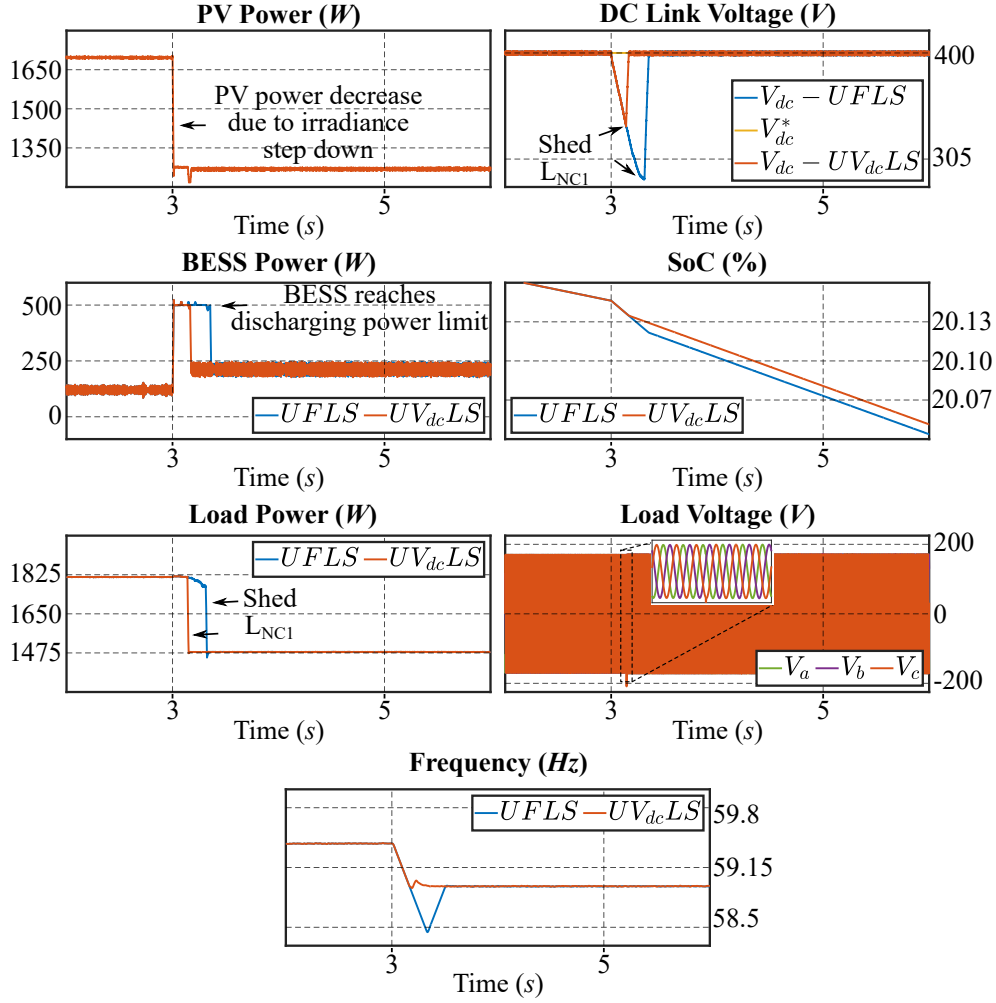
Figure 39 – Scenario 4 results with $UV_{dc}LS$ and secondary frequency droop turned on.

Source: Made by the author.

6.1.4.1 $UV_{dc}LS \times UFLS$ Comparison

Here, a comparison between the traditional $UFLS$ and the proposed $UV_{dc}LS$ is established through the same simulation described in this scenario. It is crucial to understand that such a comparison is only possible if the secondary frequency control is turned off. When this controller is working, it pushes the frequency to a safe range even for a high imbalance between active power generation and load demand (NUTKANI *et al.*, 2015). Note that the results previously presented have shown no considerable frequency variation. Then, a frequency deviation is necessary to simulate the traditional $UFLS$, otherwise, no load would be shed in critical situations. The next paragraphs detail the performance of each method. The results are depicted in Figure 40.

Similarly, the simulation begins with a 1475 W critical load and the same values of L_{NC1} resulting in a total of 1825 W of load power. The PV operates always in MPPT mode, and the BESS absorbs 125 W. As there is no strategy regulating the frequency at f_0 , the frequency varies according to the traditional droop equation (5.21). Then, at the first moment, the operating frequency is calculated as follows:

Figure 40 – Comparison between $UFLS$ and $UV_{dc}LS$ with frequency secondary control turned off.

Source: Made by the author.

$$f = 60 + 0.005(1700 - 1825) = 59.375 \text{ Hz} \quad (6.1)$$

Then, the initial frequency is 59.375 Hz. At 3s, the irradiance step down suddenly decreases the PV power to 1250W, making the BESS reaches the maximum discharging limit trying to keep the power balance. In this case, the new calculated frequency is:

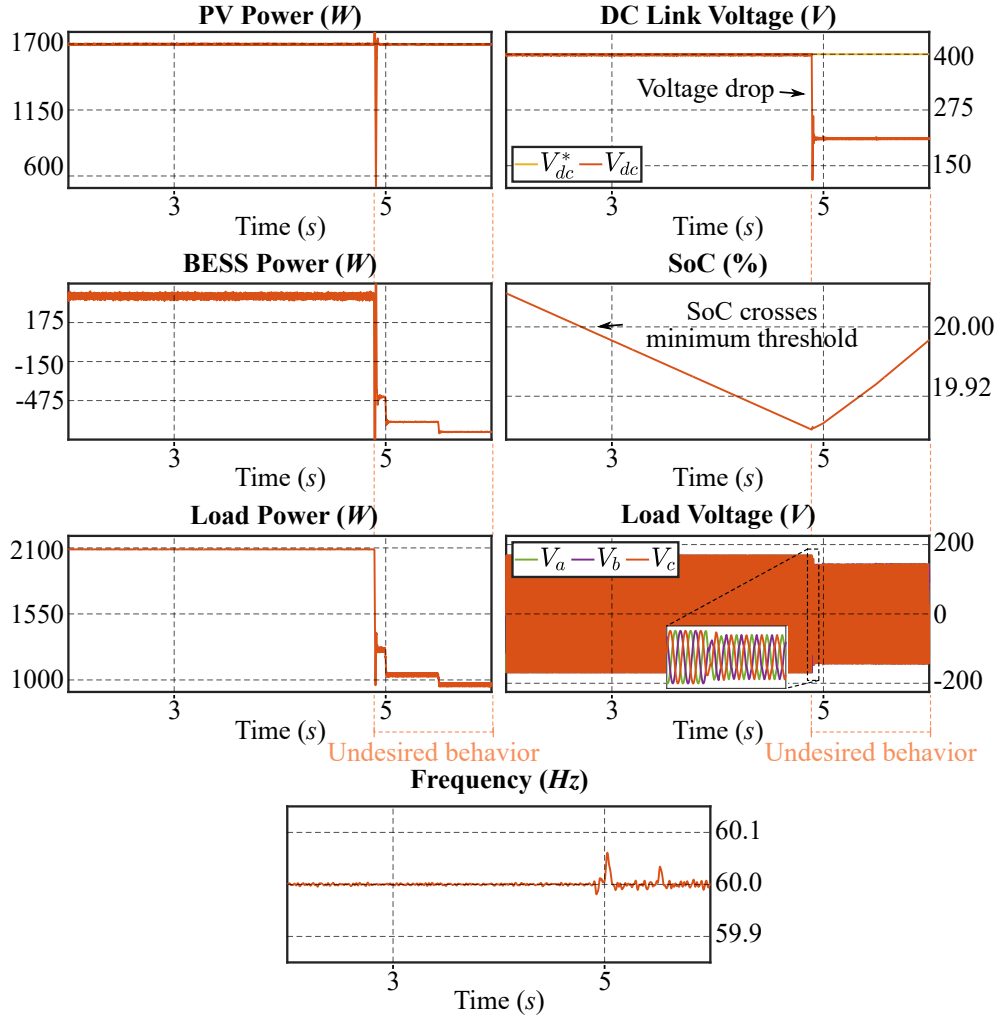
$$f = 60 + 0.005(1250 - 1825) = 57.125 \text{ Hz} \quad (6.2)$$

The frequency starts to decrease leading to 57.125 Hz. However, after 100 ms, the proposed $UV_{dc}LS$ strategy detects the power imbalance and shed L_{NC1} to decrease the load to 1475 W.

The same simulation was performed implementing traditional $UFLS$ (BAKAR *et al.*, 2017). This method shed load whenever the frequency drops below a pre-defined limit. When the PV power suddenly decreases, the traditional $UFLS$ waits until the

frequency drops below the minimum under-frequency value of 58.5 Hz for Distributed Energy Resources (DER) regulated by IEEE Standard 1547- (IEEE..., 2018) to make a decision (BAKAR *et al.*, 2017). In this simulation, the frequency took about 300 ms to cross the lower threshold.

Figure 41 – Scenario 5 results without AWD in PI_{B3} .



Source: Made by the author.

Both strategies showed to properly shed non-critical load to keep the power balance. The larger delay observed using the traditional $UFLS$ may be mitigated by adjusting the minimum frequency threshold. However, the proposed $UV_{dc}LS$ is still more attractive for the reasons listed below:

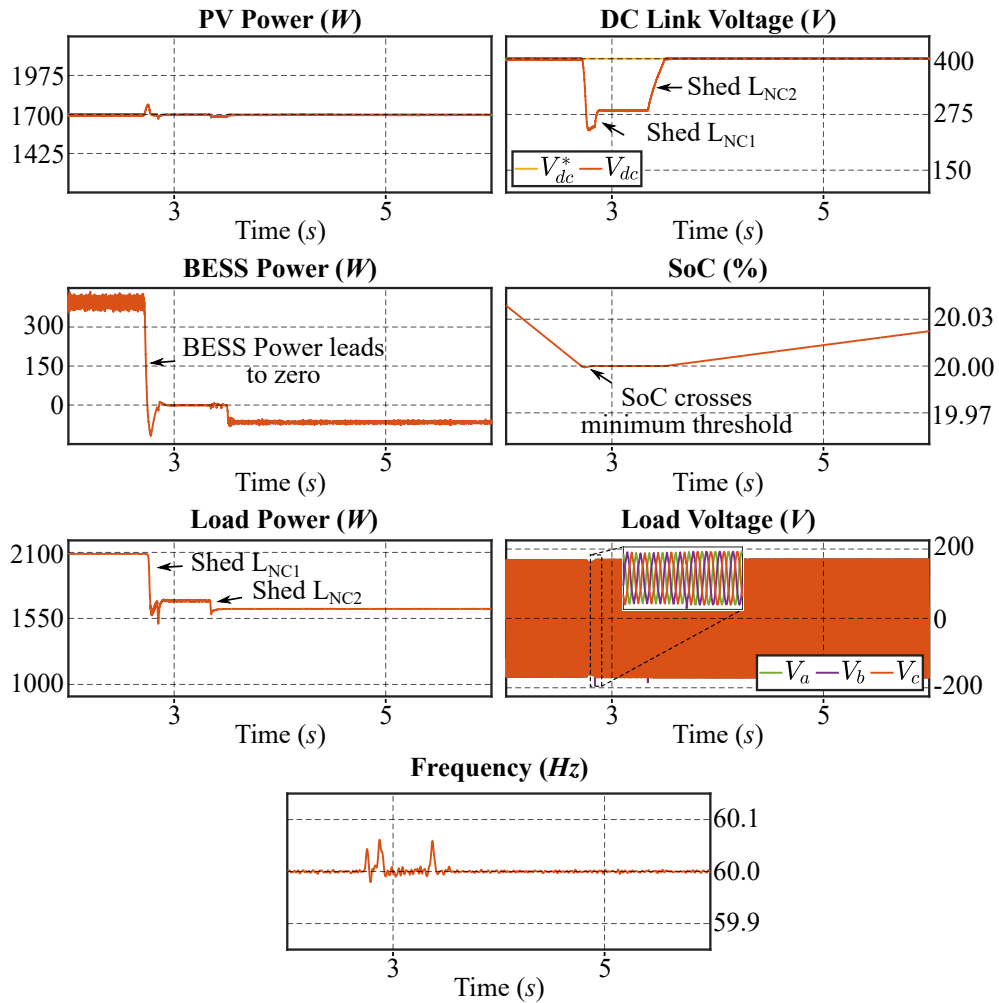
1. Faster response once it does not rely on frequency estimation, but only on local DC-voltage measurement;
2. When attached to the secondary frequency regulator droop control it provides a good alternative to detecting power unbalances without the need for large frequency variations.

Finally, it is important to highlight again that the best scenario is always to keep the frequency in a safe range. Then, turning on the secondary droop control is fundamental.

6.1.5 Scenario 5: Transition from State 1 to State 5

The results of this scenario were obtained from a situation where the SoC has reached SoC_{\min} . In order to protect the BESS from deep discharge, the action of PI_{B3} drags the reference current i_{LB}^* to zero. This control loop was proposed in Soares (2022), but the drawbacks were not mentioned. Like PI_1 loop, this may suffer from a windup effect whenever the unit work with a different SoC value than SoC_{\min} . Again, this work proposes the use of AWD methods in this controller and shows the consequences of not using it. First, the next paragraph describes how the unit is expected to work in the current scenario.

Figure 42 – Scenario 5 results with CAW in PI_{B3} .

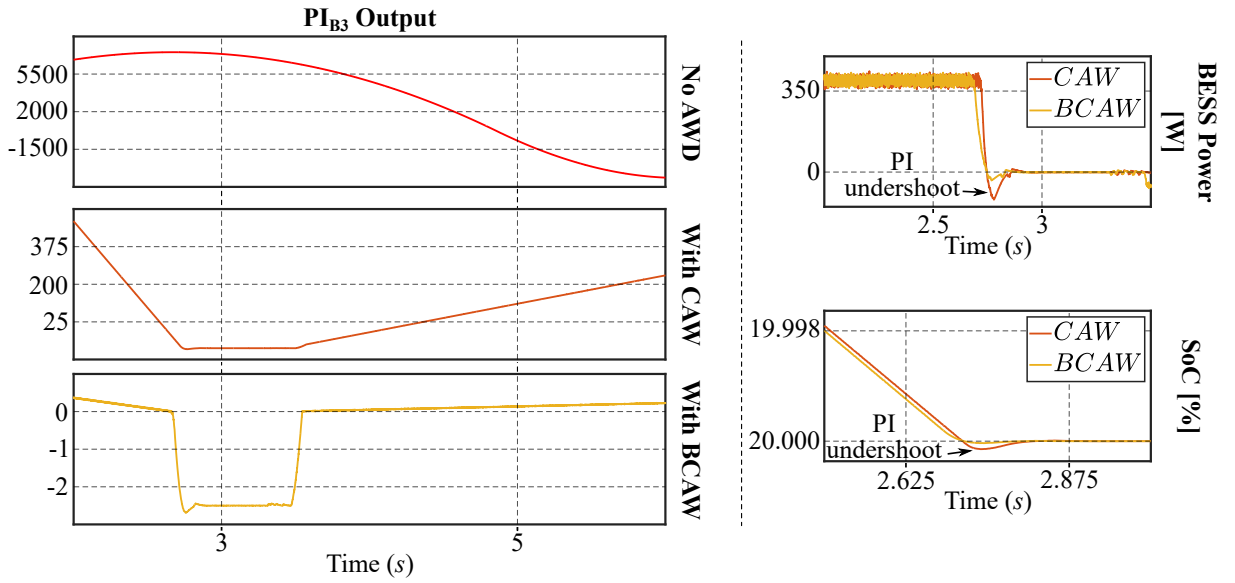


Source: Made by the author.

At the starting point, the PV unit operates at nominal irradiance and temperature conditions (1000 W/m^2 , 25°C) injecting 1700 W . The load is composed of one critical load of 1630 W , and two hierarchically disposed non-critical loads (L_{NC1} and L_{NC2}) of

350 W and 120 W, respectively. As mentioned previously, L_{NC1} is a less priority than L_{NC2} . Then, the total load power connected is 2100 W. As the load is greater than the PV generation, the BESS injects 400 W to maintain stability. When the SoC crosses SoC_{min} at approximately 2.7 s, the BESS power leads to zero due to the action of PI_{B3} , switching the unit to state 5. As the BESS can't compensate for the lack, V_{dc} drops. The $UV_{dc}LS$ algorithm detects unbalance and after 100 ms L_{NC1} is disconnected from the system. However, the disconnection of L_{NC1} is not enough to keep the balance since the total load power is greater than the PV power. The critical load and L_{NC2} together sum 1750 W, but the PV unit only injects 1700 and the BESS can't discharge. In this case, the system must shed L_{NC2} . To avoid abrupt load-sheddings, the method waits 500ms since L_{NC1} was shed to disconnect L_{NC2} . The PV unit feeds the critical load of 1630 W, and the BESS absorbs the surplus of 70 W, making the SoC increase. When it happens, the unit returns to state 1.

Figure 43 – Comparison between AWD strategies in PV power, BESS power, SoC, and PI_{B3} .



Source: Made by the author.

However, the simulation was first performed without any AWD technique in PI_{B3} and the results are depicted in Figure 41. First, note that when the SoC crosses SoC_{min} nothing is done and the BESS keeps discharging. Again, it happens because PI_{B3} output signal is too far away from the safe operating point. The system waits until the signal is back to take action. However, the huge integration of non-null errors for a long period made it assume large values. After approximately 2s, the BESS suddenly drops deeply, causing a sudden drop in V_{dc} . The non-critical loads were shed, but the bidirectional controller lost the operating point, making the system unable to restore stability. This may be confirmed in Figure 43 where PI_{B3} output signal with no AWD employment is plotted.

Furthermore, the same simulation was performed with CAW, and then with BCAW in PI_{B3} . In these simulations, the proposed minimum SoC regulation loop showed to

correctly decrease the BESS power in order to prevent deep discharge. Once again, $UV_{dc}LS$ algorithm worked properly to maintain power balance, the frequency is regulated at f_0 , and AC voltage is preserved at the appropriate waveform. The behavior is exactly the same as described in the second paragraph of the subsection, and the graphics are plotted in Figure 42 using. Both AWD techniques showed satisfactory performance by avoiding undesired transients, but, again, BCAW showed little smooth improvement by reducing the controller undershoot. To illustrate this, Figure 43 depicts a comparison in the BESS power and in the SoC during the state transition. It also shows the PI_{B3} output signal through each AWD technique.

To sum up, once again the employment of AWD techniques has shown to be crucial to ensure smooth state transitions by circumventing undesired transients. Both CAW and BCAW present good performance, but when it takes to SoC regulation, BCAW provides faster response and PI undershoot and overshoot mitigation.

7 Conclusion

This work investigated an improvement for a multi-loop power management strategy in an islanded microgrid under a critical situation where the system is composed of only one generation source. The single-sourced microgrid environment employs a hybrid generation unit formed by a PV unit attached to a BESS. In normal operation, the BESS absorbs the surplus power when there is more generation available than load demand. On the other hand, when the load demand is higher than the power provides by the PV unit, the BESS injects power to keep the power balance. However, the BESS's physical limitations must be respected. In critical situations where the BESS has reached safe constraints, the system must adapt to keep stability. Therefore, the multi-loop strategy adapts to the PV power or load situation. In high-PV power availability, power curtailment must be performed to prevent BESS overcharging. However, when the PV power is not enough to meet the load and the BESS may not compensate for the lack, some loads must be shed. In order to better understand the unit behavior, the operation was divided into five operation states. The analysis and improvement were proposed to ensure a smooth transition among these operation states.

The control system is composed of several PI controllers. These controllers only act when they are required. More precisely, when the BESS reaches its limits. Then, the normal operation makes those non-used controllers keep integrating non-null errors, causing interaction windup. This effect provoke action delays and undesired behaviors such as large voltage and current deviation, BESS deep discharge, or BESS overcharge. This work proposed the use of anti-windup techniques to avoid transients. The results showed that anti-windup is fundamental to keeping the operation in safe regions, ensuring smooth transitions. Further, two anti-windup techniques were analyzed: clamping and back-calculation anti-windup. Both showed to be sufficient to provide the system with a good performance by avoiding undesired behaviors. Still, BCAW technique showed a slightly better performance in those states that require SoC regulation. As this strategy uses a feedback path to dynamically reset the integration action, it reduces the action of PI under and overshoots and consequently provides a faster response.

Furthermore, a novel load-shedding method for the single-source PV/BESS-based islanded microgrid was developed and simulated in this work. The simulations have shown that the proposed load-shedding strategy based on the capacitive DC-link voltage of the unit has correctly detected high system imbalances when the load demand is larger than the generation power. It can work in phase with robust secondary frequency droop control to circumvent considerable frequency variation and still detect harmful power imbalances. The method was compared to the traditional under-frequency load-shedding strategy.

This comparison is only possible if the secondary frequency control is turned off to allow frequency variation. Still, the proposed strategy showed faster imbalance detection in sudden decreases in PV power availability once it does not rely on frequency estimation, but only on local DC voltage measurement.

Bibliography

ABGD, A. B. d. G. D. *Geração própria de energia elétrica atinge 19 GW e alcança 70% da capacidade de energia solar do País*. 2023. <https://www.abgd.com.br/portal/geracao-propria-de-energia-eletrica-atinge-19-gw-e-alcanca-70-da-capacidade-de-energia-solar-do-pais/>. Accessed in: 03/06/2023. 15

ABID, R. *et al.* Mppt control strategies for photovoltaic applications: Algorithms and comparative analysis. In: *2019 16th International Multi-Conference on Systems, Signals Devices (SSD)*. [S.l.: s.n.], 2019. p. 566–572. 58, 59

AHMED, A. *Power Electronics for Technology*. [S.l.]: Pearson Education, 1999. 41

AKAGI, H.; KANAZAWA, Y.; NABAE, A. Instantaneous reactive power compensators comprising switching devices without energy storage components. *IEEE Transactions on Industry Applications*, IA-20, n. 3, p. 625–630, 1984. 63

ÅSTRÖM, K. J.; HÄGGLUND, T. *Advanced PID control*. [S.l.]: ISA-The Instrumentation, Systems, and Automation Society Research Triangle Park, 2006. v. 461. 18, 51, 54, 73

ASTROM, K. J.; RUNDQWIST, L. Integrator windup and how to avoid it. In: *1989 American Control Conference*. [S.l.: s.n.], 1989. p. 1693–1698. 54

BAKAR, N. N. A. *et al.* Microgrid and load shedding scheme during islanded mode: A review. *Renewable and Sustainable Energy Reviews*, Elsevier, v. 71, p. 161–169, 2017. 17, 80, 81

BARONTI, F. *et al.* Comparing open-circuit voltage hysteresis models for lithium-iron-phosphate batteries. *IECON 2014 - 40th Annual Conference of the IEEE Industrial Electronics Society*, IEEE, p. 5635–5640, 2014. 21, 44

BARONTI, F. *et al.* Hysteresis modeling in li-ion batteries. *IEEE Transactions on Magnetism*, IEEE, v. 50, n. 11, p. 1–4, 2014. 21, 33

BARONTI, F. *et al.* Experimental analysis of open-circuit voltage hysteresis in lithium-iron-phosphate batteries. *IECON 2013 - 39th Annual Conference of the IEEE Industrial Electronics Society*, IEEE, p. 6728–6733, 2013. 21, 33, 44

BARROS, L. S.; BARROS, C. M. V. Modificação no controle do lado da rede de geradores eólicos baseados em pmsg para ampliar a suportabilidade a afundamentos de tensão. *Eletrônica de Potência*, v. 22, n. 2, p. 167–178, 2017. 21

BEHERA, M. K.; SAIKIA, L. C. Anti-windup filtered second-order generalized integrator-based spontaneous control for single-phase grid-tied solar pv-h₂/br₂ redox flow battery storage microgrid system. *Journal of Energy Storage*, v. 55, p. 105551, 2022. ISSN 2352-152X. 26

BIRICIK, S.; KOMURCUGIL, H. Proportional-integral and proportional-resonant based control strategy for puc inverters. In: *IECON 2018 - 44th Annual Conference of the IEEE Industrial Electronics Society*. [S.l.: s.n.], 2018. p. 3369–3373. 65

- CHE, L. *et al.* Hierarchical coordination of a community microgrid with ac and dc microgrids. *IEEE Transactions on Smart Grid*, v. 6, n. 6, p. 3042–3051, 2015. 16
- CHTITA, S. *et al.* An improved control strategy for charging solar batteries in off-grid photovoltaic systems. *Solar Energy*, v. 220, p. 927–941, 2021. ISSN 0038-092X. 23, 25
- CRISPIM, J.; CARREIRA, M.; CASTRO, R. Validation of photovoltaic electrical models against manufacturers data and experimental results. In: *2007 International Conference on Power Engineering, Energy and Electrical Drives*. [S.l.: s.n.], 2007. p. 556–561. 31
- DU, H. *et al.* An adaptive frequency phase-locked loop based on a third order generalized integrator. *Energies*, v. 12, n. 2, 2019. ISSN 1996-1073. Disponível em: <<https://www.mdpi.com/1996-1073/12/2/309>>. 67
- DURSUN, M.; DÖŞOĞLU, M. K. Lcl filter design for grid connected three-phase inverter. In: *2018 2nd International Symposium on Multidisciplinary Studies and Innovative Technologies (ISMSIT)*. [S.l.: s.n.], 2018. p. 1–4. 43
- GARG, A. *et al.* Comparative analysis of maximum power point algorithms for solar pv applications. In: *2020 21st National Power Systems Conference (NPSC)*. [S.l.: s.n.], 2020. p. 1–6. 15
- GOMES, C. C.; CUPERTINO, A. F.; PEREIRA, H. A. Damping techniques for grid-connected voltage source converters based on lcl filter: An overview. *Renewable and Sustainable Energy Reviews*, v. 81, p. 116–135, 2018. ISSN 1364-0321. 43
- HADJIDEMETRIOU, L.; KYRIAKIDES, E.; BLAABJERG, F. A new hybrid pll for interconnecting renewable energy systems to the grid. In: *2012 IEEE Energy Conversion Congress and Exposition (ECCE)*. [S.l.: s.n.], 2012. p. 2075–2082. 67, 68
- HANUS, R. A new technique for preventing control windup. *Journal A*, v. 21, n. 1, p. 15–20, 1980. 18
- HANUS, R. A new technique for preventing control windup. *Journal A*, v. 21, n. 1, p. 15–20, 1980. 53
- IEEE Standard for Interconnection and Interoperability of Distributed Energy Resources with Associated Electric Power Systems Interfaces. *IEEE Std 1547-2018 (Revision of IEEE Std 1547-2003)*, p. 1–138, 2018. 81
- IMPROVEMENT and validation of a model for photovoltaic array performance. *Solar Energy*, v. 80, n. 1, p. 78–88, 2006. ISSN 0038-092X. 31
- JALIL, M. H. A. *et al.* Pid with clamping anti-windup performance on temperature regulation of glycerin bleaching process. In: *2021 IEEE 12th Control and System Graduate Research Colloquium (ICSGRC)*. [S.l.: s.n.], 2021. p. 127–131. 53
- JUNIOR, G. P. da S.; BARROS, L. S.; BARROS, C. M. V. Synchronverter coupled to a lithium-ion bank for grid frequency and voltage supports and controlled charge-discharge. *Electric Power Systems Research*, Elsevier, v. 197, p. 107352, 2021. 21, 33
- KARIMI, Y. *et al.* Decentralized method for load sharing and power management in a pv/battery hybrid source islanded microgrid. *IEEE Transactions on Power Electronics*, v. 32, n. 5, p. 3525–3535, 2017. 16, 17

- KARIMI, Y.; ORAEE, H.; GUERRERO, J. M. Decentralized method for load sharing and power management in a hybrid single/three-phase-islanded microgrid consisting of hybrid source pv/battery units. *IEEE Transactions on Power Electronics*, v. 32, n. 8, p. 6135–6144, 2017. 16, 19, 24, 63
- KAZIMIERCZUK, M. K. *Pulse-width Modulated DC-DC Power Converters*. [S.l.]: Wiley, 2008. 34, 35, 38
- KEIVANIMEHR, M. *et al.* Load shedding frequency management of microgrids using hierarchical fuzzy control. In: *2021 World Automation Congress (WAC)*. [S.l.: s.n.], 2021. p. 216–221. 57
- KHAN, D. *et al.* A resonant damping control and analysis for lcl-type grid-connected inverter. *Energy Reports*, v. 8, p. 911–928, 2022. ISSN 2352-4847. 43
- LI, Z. *et al.* Adaptive droop control using adaptive virtual impedance for microgrids with variable pv outputs and load demands. *IEEE Transactions on Industrial Electronics*, v. 68, n. 10, p. 9630–9640, 2021. 18
- LIAO, C. *et al.* Clean energy transitions and human well-being outcomes in lower and middle income countries: A systematic review. *Renewable and Sustainable Energy Reviews*, v. 145, p. 111063, 2021. ISSN 1364-0321. 15
- MAESTRI, C. O. N. M.; ANDRADE, M. E. M. C. Priorities for tariff compensation of distributed electricity generation in brazil. *Utilities Policy*, v. 76, p. 101374, 2022. ISSN 0957-1787. 15
- MAHMOOD, H.; BLAABJERG, F. Autonomous power management of distributed energy storage systems in islanded microgrids. *IEEE Transactions on Sustainable Energy*, v. 13, n. 3, p. 1507–1522, 2022. 26
- MAHMOOD, H.; MICHAELSON, D.; JIANG, J. Control strategy for a standalone pv/battery hybrid system. In: *IECON 2012 - 38th Annual Conference on IEEE Industrial Electronics Society*. [S.l.: s.n.], 2012. p. 3412–3418. 18, 21, 24
- MAHMOOD, H.; MICHAELSON, D.; JIANG, J. Decentralized power management of a pv/battery hybrid unit in a droop-controlled islanded microgrid. *IEEE Transactions on Power Electronics*, v. 30, n. 12, p. 7215–7229, 2015. 25
- MENG, L. *et al.* Microgrid central controller development and hierarchical control implementation in the intelligent microgrid lab of aalborg university. In: *2015 IEEE Applied Power Electronics Conference and Exposition (APEC)*. [S.l.: s.n.], 2015. p. 2585–2592. 16
- MICHAELSON, D.; MAHMOOD, H.; JIANG, J. A predictive energy management system using pre-emptive load shedding for islanded photovoltaic microgrids. *IEEE Transactions on Industrial Electronics*, v. 64, n. 7, p. 5440–5448, 2017. 27
- MIDDLEBROOK, R. D.; CUK, S. A general unified approach to modelling switching-converter power stages. In: *1976 IEEE Power Electronics Specialists Conference*. [S.l.: s.n.], 1976. p. 18–34. 60

MOREIRA, A. V. S. *et al.* An adaptive perturb and observe method with clustering for photovoltaic module with smart bypass diode under partial shading. In: *2019 IEEE PES Innovative Smart Grid Technologies Conference - Latin America (ISGT Latin America)*. [S.l.: s.n.], 2019. p. 1–6. 30

NATIONS, U. *Ensure access to affordable, reliable, sustainable and modern energy*. 2022. <https://www.un.org/sustainabledevelopment/energy/>. Acesso em: 05/05/2022. 15

NUTKANI, I. U. *et al.* Secondary droop for frequency and voltage restoration in microgrids. In: *2015 17th European Conference on Power Electronics and Applications (EPE'15 ECCE-Europe)*. [S.l.: s.n.], 2015. p. 1–7. 19, 65, 79

OGATA, K. *Engenharia de Controle Moderno*. [S.l.]: Prentice Hall, 2003. 61

RASHID, M. H. *Power Electronics: Devices, Circuits and Applications*. [S.l.]: Pearson Education, 2014. 35, 36, 38, 39, 41, 42

RAUSCHENBACH, H. S. *Solar Cell Array Design Handbook*. [S.l.]: Van Nostrand Reinhold, 1980. 30

REZKALLAH, M. *et al.* Comprehensive controller implementation for wind-pv-diesel based standalone microgrid. *IEEE Transactions on Industry Applications*, v. 55, n. 5, p. 5416–5428, 2019. 23, 25

SADOUDI, S.; BOUDOUR, M.; KOUBA, N. E. Y. Multi-microgrid intelligent load shedding for optimal power management and coordinated control with energy storage systems. *International Journal of Energy Research*, Wiley Online Library, v. 45, n. 11, p. 15857–15878, 2021. 28

SAHIN, Y.; TING, N. S. Design of a new bidirectional dc-dc converter. In: *INCES 2019 - International Congress of Science, Culture and Education*. [S.l.: s.n.], 2019. p. 228–233. 37

SERBAN, I.; MARINESCU, C. Control strategy of three-phase battery energy storage systems for frequency support in microgrids and with uninterrupted supply of local loads. *IEEE Transactions on Power Electronics*, v. 29, n. 9, p. 5010–5020, 2014. 17

SHATAKSHI; SINGH, B.; MISHRA, S. Dual mode operational control of single stage pv-battery based microgrid. In: *2018 IEEMA Engineer Infinite Conference (eTechNxT)*. [S.l.: s.n.], 2018. p. 1–5. 16, 17

SHEIKHZADEHBABOLI, P. *et al.* Frequency control in standalone renewable based-microgrids using steady state load shedding considering droop characteristic. *International Journal of Electrical Power Energy Systems*, v. 142, p. 108351, 2022. ISSN 0142-0615. 17

SILVA JÚNIOR, G. P. d. *Implementação de Máquina Síncrona Virtual do Tipo Synchronverter para o Gerador de Indução Duplamente Alimentado Conectado a uma Microrrede*. Tese (presented to Computer and Electrical Engineering Graduate Program) — Universidade Federal do Rio Grande do Norte, Natal, 2021. 67, 68

SLONIM, M. A.; SHAVIT, D. S. Linearization of the output characteristics of a solar cell and its application for the design and analysis of solar cell arrays. In: IEEE. *IECEC-97 Proceedings of the Thirty-Second Intersociety Energy Conversion Engineering Conference (Cat. No. 97CH6203)*. [S.l.], 1997. v. 3, p. 1934–1938. 60

- SOARES, L. C. S. *Estratégia de gerenciamento de microrrede trifásica com PV e bateria incluindo o corte de carga baseado na tensão do barramento CC*. Dissertação (Mestrado) — Federal University of Paraíba, Brazil, 2022. 21, 46, 49, 52, 54, 82
- SUN, Q. *et al.* Hybrid three-phase/single-phase microgrid architecture with power management capabilities. *IEEE Transactions on Power Electronics*, v. 30, n. 10, p. 5964–5977, 2015. 16
- TEODORESCU, R. *et al.* Proportional-resonant controllers and filters for grid-connected voltage-source converters. *IEE Proceedings-Electric Power Applications*, IET, v. 153, n. 5, p. 750–762, 2006. 65, 66
- VANDOORN, T. L. *et al.* Analogy between conventional grid control and islanded microgrid control based on a global dc-link voltage droop. *IEEE Transactions on Power Delivery*, v. 27, n. 3, p. 1405–1414, 2012. 64
- VASQUEZ, J. C. *et al.* Modeling, analysis, and design of stationary-reference-frame droop-controlled parallel three-phase voltage source inverters. *IEEE Transactions on Industrial Electronics*, v. 60, n. 4, p. 1271–1280, 2013. 19, 66
- VILLALVA J.R. GAZOLI, E. R. F. M. Modeling and circuit-based simulation of photovoltaic arrays. *Brazilian Journal of Power Electronics*, v. 14(1), p. 35–45, 2009. 30, 31, 32
- VILLALVA, M. G.; GAZOLI, J. R.; FILHO, E. R. Comprehensive approach to modeling and simulation of photovoltaic arrays. *IEEE Transactions on Power Electronics*, v. 24, n. 5, p. 1198–1208, 2009. 21, 30
- VISCONTI, I. F. *Modelos de Cargas Baseados em Medições para Simulações Dinâmicas em Sistemas Elétricos de Potência*. Dissertação (Master Thesis) — Pontifícia Universidade Católica do Rio de Janeiro, 2010. 43
- WANG, F.; ZHANG, C. Protection and control for grid connected photovoltaic power generation system based on instantaneous power theory. In: *2009 Pacific-Asia Conference on Circuits, Communications and Systems*. [S.l.: s.n.], 2009. p. 356–359. 15
- ZHENG, H.; CHANG, X.; WANG, X. Study on the control strategy of grid connected and disconnected of microgrid with photovoltaic and storages. In: *2013 International Conference on Materials for Renewable Energy and Environment*. [S.l.: s.n.], 2013. v. 1, p. 115–118. 16